Flexural Behaviour of One-Way Concrete Slabs Reinforced by Glass-Fibre Reinforced Plastic Bars

by

Craig R. Michaluk

A Thesis

presented to the University of Manitoba

in partial fulfilment of the

Requirements for the Degree of

Master of Science

Structural Engineering Division
Department of Civil & Geological Engineering
University of Manitoba
Winnipeg, Manitoba

ISBN 0-612-13373-7

Canada

Name _____

Dissertation Abstracts International and *Masters Abstracts International* are arranged by broad, general subject categories. Please select the one subject which most nearly describes the content of your dissertation or thesis. Enter the corresponding four-digit code in the spaces provided.

Civil Engineering
SUBJECT TERM

0543 UMI
SUBJECT CODE

Subject Categories

THE HUMANITIES AND SOCIAL SCIENCES

COMMUNICATIONS AND THE ARTS
Architecture 0729
Art History 0377
Cinema 0900
Dance 0378
Fine Arts 0357
Information Science 0723
Journalism 0391
Library Science 0399
Mass Communications 0708
Music 0413
Speech Communication 0459
Theater 0465

EDUCATION
General 0515
Administration 0514
Adult and Continuing 0516
Agricultural 0517
Art 0273
Bilingual and Multicultural 0282
Business 0688
Community College 0275
Curriculum and Instruction 0727
Early Childhood 0518
Elementary 0524
Finance 0277
Guidance and Counseling 0519
Health 0680
Higher 0745
History of 0520
Home Economics 0278
Industrial 0521
Language and Literature 0279
Mathematics 0280
Music 0522
Philosophy of 0998
Physical 0523
Psychology 0525
Reading 0535
Religious 0527
Sciences 0714
Secondary 0533
Social Sciences 0534
Sociology of 0340
Special 0529
Teacher Training 0530
Technology 0710
Tests and Measurements 0288
Vocational 0747

LANGUAGE, LITERATURE AND LINGUISTICS
Language
- General 0679
- Ancient 0289
- Linguistics 0290
- Modern 0291

Literature
- General 0401
- Classical 0294
- Comparative 0295
- Medieval 0297
- Modern 0298
- African 0316
- American 0591
- Asian 0305
- Canadian (English) 0352
- Canadian (French) 0355
- English 0593
- Germanic 0311
- Latin American 0312
- Middle Eastern 0315
- Romance 0313
- Slavic and East European 0314

PHILOSOPHY, RELIGION AND THEOLOGY
Philosophy 0422
Religion
- General 0318
- Biblical Studies 0321
- Clergy 0319
- History of 0320
- Philosophy of 0322

Theology 0469

SOCIAL SCIENCES
American Studies 0323
Anthropology
- Archaeology 0324
- Cultural 0326
- Physical 0327

Business Administration
- General 0310
- Accounting 0272
- Banking 0770
- Management 0454
- Marketing 0338

Canadian Studies 0385
Economics
- General 0501
- Agricultural 0503
- Commerce-Business 0505
- Finance 0508
- History 0509
- Labor 0510
- Theory 0511

Folklore 0358
Geography 0366
Gerontology 0351
History
- General 0578
- Ancient 0579
- Medieval 0581
- Modern 0582
- Black 0328
- African 0331
- Asia, Australia and Oceania 0332
- Canadian 0334
- European 0335
- Latin American 0336
- Middle Eastern 0333
- United States 0337

History of Science 0585
Law 0398
Political Science
- General 0615
- International Law and Relations 0616
- Public Administration 0617

Recreation 0814
Social Work 0452
Sociology
- General 0626
- Criminology and Penology ... 0627
- Demography 0938
- Ethnic and Racial Studies 0631
- Individual and Family Studies 0628
- Industrial and Labor Relations 0629
- Public and Social Welfare 0630
- Social Structure and Development 0700
- Theory and Methods 0344

Transportation 0709
Urban and Regional Planning 0999
Women's Studies 0453

THE SCIENCES AND ENGINEERING

BIOLOGICAL SCIENCES
Agriculture
- General 0473
- Agronomy 0285
- Animal Culture and Nutrition 0475
- Animal Pathology 0476
- Food Science and Technology 0359
- Forestry and Wildlife 0478
- Plant Culture 0479
- Plant Pathology 0480
- Plant Physiology 0817
- Range Management 0777
- Wood Technology 0746

Biology
- General 0306
- Anatomy 0287
- Biostatistics 0308
- Botany 0309
- Cell 0379
- Ecology 0329
- Entomology 0353
- Genetics 0369
- Limnology 0793
- Microbiology 0410
- Molecular 0307
- Neuroscience 0317
- Oceanography 0416
- Physiology 0433
- Radiation 0821
- Veterinary Science 0778
- Zoology 0472

Biophysics
- General 0786
- Medical 0760

EARTH SCIENCES
Biogeochemistry 0425
Geochemistry 0996
Geodesy 0370
Geology 0372
Geophysics 0373
Hydrology 0388
Mineralogy 0411
Paleobotany 0345
Paleoecology 0426
Paleontology 0418
Paleozoology 0985
Palynology 0427
Physical Geography 0368
Physical Oceanography 0415

HEALTH AND ENVIRONMENTAL SCIENCES
Environmental Sciences 0768
Health Sciences
- General 0566
- Audiology 0300
- Chemotherapy 0992
- Dentistry 0567
- Education 0350
- Hospital Management 0769
- Human Development 0758
- Immunology 0982
- Medicine and Surgery 0564
- Mental Health 0347
- Nursing 0569
- Nutrition 0570
- Obstetrics and Gynecology .. 0380
- Occupational Health and Therapy 0354
- Ophthalmology 0381
- Pathology 0571
- Pharmacology 0419
- Pharmacy 0572
- Physical Therapy 0382
- Public Health 0573
- Radiology 0574
- Recreation 0575
- Speech Pathology 0460
- Toxicology 0383

Home Economics 0386

PHYSICAL SCIENCES
Pure Sciences
Chemistry
- General 0485
- Agricultural 0749
- Analytical 0486
- Biochemistry 0487
- Inorganic 0488
- Nuclear 0738
- Organic 0490
- Pharmaceutical 0491
- Physical 0494
- Polymer 0495
- Radiation 0754

Mathematics 0405
Physics
- General 0605
- Acoustics 0986
- Astronomy and Astrophysics 0606
- Atmospheric Science 0608
- Atomic 0748
- Electronics and Electricity 0607
- Elementary Particles and High Energy 0798
- Fluid and Plasma 0759
- Molecular 0609
- Nuclear 0610
- Optics 0752
- Radiation 0756
- Solid State 0611

Statistics 0463

Applied Sciences
Applied Mechanics 0346
Computer Science 0984
Engineering
- General 0537
- Aerospace 0538
- Agricultural 0539
- Automotive 0540
- Biomedical 0541
- Chemical 0542
- Civil 0543
- Electronics and Electrical 0544
- Heat and Thermodynamics ... 0348
- Hydraulic 0545
- Industrial 0546
- Marine 0547
- Materials Science 0794
- Mechanical 0548
- Metallurgy 0743
- Mining 0551
- Nuclear 0552
- Packaging 0549
- Petroleum 0765
- Sanitary and Municipal 0554
- System Science 0790

Geotechnology 0428
Operations Research 0796
Plastics Technology 0795
Textile Technology 0994

PSYCHOLOGY
General 0621
Behavioral 0384
Clinical 0622
Developmental 0620
Experimental 0623
Industrial 0624
Personality 0625
Physiological 0989
Psychobiology 0349
Psychometrics 0632
Social 0451

FLEXURAL BEHAVIOUR OF ONE-WAY CONCRETE SLABS REINFORCED BY GLASS-FIBRE REINFORCED PLASTIC BARS

BY

CRAIG R. MICHALUK

A Thesis submitted to the Faculty of Graduate Studies of the University of Manitoba in partial fulfillment of the requirements of the degree of

MASTER OF SCIENCE

ABSTRACT

Glass-Fibre Reinforced Plastic (GFRP) bars are currently used for special concrete structures in areas sensitive to magnetic fields and severe environmental conditions which accelerate corrosion of the steel reinforcements and, consequently, deterioration of the structure. An extensive testing program is currently being sponsored by the Canadian government to study the flexural behaviour of concrete slabs reinforced by ISOROD-GFRP reinforcements produced in Canada.

This thesis presents the experimental program undertaken at the Structural Engineering and Construction R&D Facility of the University of Manitoba to test a total of eight one-way concrete slabs reinforced with glass-fibre, carbon-fibre and conventional steel reinforcements. The slabs were tested under static loading conditions to determine their flexural limit states, including the behaviour prior to cracking, cracking, ultimate capacities and modes of failure. Based on this investigation, design recommendations and guidelines are proposed.

ACKNOWLEDGMENTS

The author would like to express his sincere thanks to Dr. Sami Rizkalla for providing his immeasurable guidance, assistance and advice during the research program.

The technical assistance given by Messrs. Ed Lemke, Scott Sparrow and Moray McVey during the experimental work is greatly appreciated. Special thanks go to Ms. Susan Grieef and all the graduate students for their assistance during the construction and testing of the specimens.

The financial assistance provided by the Natural Sciences and Engineering Research Council of Canada is greatly acknowledged. As well, Pultrall Inc., Thetford Mines, Québec, Canada for the donation of the material used in the research program.

Finally, the author wishes to express his deeply-felt gratitude to his parents who made all this possible. The tremendous support, patience and guidance of my father, Ronald W. Michaluk, and my mother, Barbara J. Michaluk, cannot be praised enough; to them this thesis is dedicated.

TABLE OF CONTENTS

CHAPTER 3: EXPERIMENTAL PROGRAM

CHAPTER 4: EXPERIMENTAL RESULTS

CHAPTER 6: SUMMARY AND CONCLUSIONS

LIST OF TABLES

TABLE

LIST OF FIGURES

FIGURE

NOTATION

a	=	shear span.
A_F	=	cross-sectional area of FRP reinforcements.
A_s	=	cross-sectional area of steel reinforcements.
b_w	=	width of slabs (b).
d	=	depth to center of reinforcements, measured from the extreme compression fibre of concrete ([mm] for Japanese equations, [mm] for the rest).
d_b	=	diameter of reinforcement.
E_F	=	elastic modulus of FRP in tension.
E_s	=	elastic modulus of steel in tension.
f'_c	=	compressive strength of concrete cylinders.
g	=	acceleration due to gravity (9.810 m/s^2).
M_u	=	factored ultimate moment.
P_{cr}	=	cracking load.
ΔP	=	step wise drop in load after initiation of first crack.
P_{ult}	=	ultimate load.
s_{cF}	=	average crack spacing for FRP reinforced specimens.
s_{cs}	=	average crack spacing for steel reinforced specimens.

w_{1F} = average first crack width for FRP reinforced specimens at load P_{cr}.

w_{1s} = average first crack width for steel reinforced specimens at load P_{cr}.

V_c = concrete contribution of the shear capacity of a reinforced concrete member.

V_u = factored ultimate shear load.

α_1 = factor to define rectangular stress block in compression zone.

= $0.85-.0015f'_c \geq 0.67$.

β = factor to define rectangular stress block in compression zone.

= $0.97-.0025f'_c \geq 0.67$.

β_1 = material factor for the diameter effect on FRP bars.

β_2 = material factor for the general behaviour of a specific FRP bar type in concrete.

β_d = shear factor for d in JSCE Design Code (JSCE 1984).

β_ρ = shear factor for ρ in JSCE Design Code (JSCE 1984).

β_n = shear factor for axial applied loads in JSCE Design Code (JSCE 1984).

Δ_{ult} = midspan deflection at ultimate load.

ε_{cu} = strain in concrete at ultimate compression stress (0.003).

ε_{Fu} = ultimate tensile strain in FRP reinforcements.

ϕ_c = concrete material factor (0.60).

κ = shear factor for d in CEB-FIP Design Code (CEB-FIP 1978).

λ = concrete type factor (1.0 for normal).

ρ = reinforcement ratio (A_F or A_s / bd).

ρ_b = balanced reinforcement ratio.

ρ_{Fmin} = minimum reinforcement ratio for GFRP reinforced concrete members.

σ_{Fu} = ultimate tensile strength of FRP.

σ_{Fexp} = tensile stress achieved in FRP at a given stage.

τ_{Rd} = shear factor for concrete strengths in CEB-FIP Design Code (CEB-FIP 1978).

CHAPTER 1

INTRODUCTION

1.0 GENERAL

Corrosion of steel reinforcements is drastically reducing the service life of reinforced concrete structures. One-way reinforced concrete slabs, which are mainly used in parking structures and bridge decks, are subjected to accelerated corrosion rates due to the addition of deicing salts. Glass-fibre reinforced plastics (GFRP) are suitable reinforcements for these concrete structures, due to their high strength-to-weight ratio, non-magnetic and non-corrosive characteristics (Chaallal and Benmokrane 1993). This study focused on the flexural behaviour of one-way concrete slabs reinforced by GFRP bars, produced by Pultrall Inc., Thetford Mines, Québec, Canada.

Lack of information on the GFRP bar as flexural reinforcement prompted the Canadian government to initiate a large scale study on ISOROD-GFRP reinforcements in

concrete structures. Various reinforcement ratios and slab thicknesses were studied to evaluate the performance of the ISOROD-GFRP bar as longitudinal reinforcement for concrete slabs.

1.1 OBJECTIVES

The main objective of this research test program was to investigate the flexural behaviour of one-way concrete slabs reinforced by GFRP bars in terms of flexural cracks, deflection, strains and mode of failure.

1.2 SCOPE

A total of eight slabs were fabricated and tested to failure in this experimental program. All the test slabs were reinforced one-way concrete slabs with rectangular cross-sections. All the slabs were tested to failure under the same static loading conditions. The different longitudinal reinforcements included ISOROD-GFRP, Leadline-Carbon Fibre Reinforced Plastic (CFRP) and steel reinforcements.

A brief review of the flexural behaviour of concrete slabs and beams reinforced by FRP reinforcements is given in Chapter 2. Civil engineering applications and the material characteristics used in this test program are also included in Chapter 2.

Chapter 3 gives a detailed description on the experimental program, including the design and fabrication of the test slabs, material property testing, test setup, instrumentation and test procedure.

A summary of the experimental results is given in Chapter 4. This includes the observed behaviour and measured data for all the tested slabs.

Discussion of the experimental results is give in Chapter 5, including the flexural behaviour and the analytical models.

The final chapter, Chapter 6, includes the summary, conclusions and recommendations based on the experimental program.

CHAPTER 2

LITERATURE REVIEW

2.0 GENERAL

Parking structures and bridge decks subjected to severe environmental conditions could experience deterioration of the main structural concrete components due to corrosion of steel, and consequently suffer reduced life time serviceability. Significant fluctuation of the temperature and use of salt for deicing also accelerates the corrosion process of the steel reinforcements. In Canada, it is estimated that the total cost to repair parking structures is in the range of four to six billion dollars (Bédard 1992). The estimated repair cost for existing highway bridges in U.S. is over 50 billion dollars, and one to three trillion dollars for all concrete structures (Fickelhorn 1990). Excessive corrosion problems also exist in Arabian Gulf countries (Maktouf et al 1991). The exterior of reinforced concrete structures in these countries are subjected to an extremely aggressive environment due to the high temperatures and humidities. Presence of

shrinkage and flexural cracks allows intrusion of salt-laden condensation, contaminated rain water, oxygen and carbon dioxide gases. This mixture of chemicals and moisture eventually penetrates to the level of steel reinforcement and accelerates its corrosion rate. Many techniques have been studied to delay the corrosion rates. These include cathodic protection systems (Howell 1990) and use of galvanized or epoxy coated rebars (Yeomans 1994). Long term efficiency of these systems is still uncertain (Clarke 1993). Engineers are currently exploring the use of fibre reinforced plastics (FRP) as a promising solution for the corrosion problem. FRP are non-corrosive, magnetically neutral and have a high strength-to-weight ratio. Although there is a tremendous diversity of the available Glass-Fibre Reinforced Plastic (GFRP) bars, no general information, or clear specifications specifically address their behaviour as reinforcements for concrete structures.

The remainder of this chapter will discuss definition, applications in Civil Engineering and material properties of FRP, and will review the flexural behavior of concrete members reinforced with GFRP and the design considerations needed for FRP reinforced concrete members.

2.1 DEFINITION OF FRP

FRP are composites where a matrix resin and fibrous materials are combined to form a certain product. The matrix resin is a type of polymer which binds the fibres together. The mechanical properties of the matrix are the same as that of a typical

polymer, hence the term "plastic" in FRP. The primary function of the matrix is to bind and protect the fibres, which bear the strength of the composite. Thermosetting resins are used to form the matrices, usually using epoxy resins or polyesters. Since the chemicals added to the resins define their mechanical properties and processability, the possible diversity of FRP is limitless. The notion of combining different materials to form superior materials comes from studying materials in nature (Hull 1981). Naturally occurring materials maximize their efficiency, with respect to strength, by aligning fibrous materials in the direction of the applied loads. Due to their processability, mechanical properties and cost, the most commonly used fibres in civil engineering applications are glass, carbon and aramid (poly-paraphenylene terephthalamide).

2.2 CIVIL ENGINEERING APPLICATIONS FOR FRP

The fibres being used today have strengths which range between 3600 MPa and 5600 MPa, allowing the development of composite reinforcements with strengths ranging between 700 MPa and 3000 MPa. Along with this very high strength though, comes the disadvantage of very small elongation prior to failure. Therefore, design codes and procedures must take into account the brittle failures associated with FRP materials. Due to the vast variety of FRP's available, applications in which FRPs are used are limited only by the creativity of the engineers and designers. The resins and fibres can be manipulated to suit certain designs in order to optimize their use. Of course, there are areas in which conventional materials may still be the most efficient material choice, but FRPs create a

new avenue for engineers to use to solve previously unsolved problems, or improve old solutions.

The remainder of this section discusses some of the current civil engineering applications using FRP reinforcements.

2.2.1 Rehabilitation of Bridges

One of the most imposing problems facing civil engineers today, is the rehabilitation of existing bridge structures. Many bridges currently in use in North America were built near the end of World War II with materials and techniques that were available at the time (CSCE 1991). Since then, the weights of trucks have increased by 40%, and the increase which was not anticipated in the original designs of most bridges (Jaeger 1989). Therefore, there are many aging structures which are carrying loads in excess of their design limits, and are in desperate need of repair. In cold-climate countries, like Canada, where the use of de-icing salts is necessary on roads, the life of current non-FRP bridges is being drastically reduced due to salt corrosion. Combined with the high volume of traffic and the high cost of reconstruction, bridges are unable to be shut down totally and therefore, must be repaired quickly and efficiently. Currently, the existing methods include the bonding of steel plates to the structure in order to increase their load carrying capacity (Meier 1988). Since the plates are made of corrosive material, within a short time the structure will weaken once more. The steel plates are also very heavy and

not easy to manipulate into the proper form and position for successful post-strengthening. With the use of highly durable, non-corrosive FRP, life spans of existing bridges can be extended. Thin FRP sheets (usually made of carbon fibre reinforced epoxy laminates 0.3 to 2 mm thick) can be bonded to the existing concrete or steel bridge with an epoxy resin adhesive to enhance the strength of the beam member and/or reduce cracking in areas of high stress (Meier 1991). Due to the light weight and high strength of FRP, handling and installation are easy and quick. Through the use of a hydraulic platform and pressure provided by a vacuum press during bonding, the manpower and the time needed to complete the repair is drastically reduced. Although the CFRP sheets are approximately 50 times more expensive per kg, the mass of CFRP needed for a repair is only about one twentieth of that for a steel repair. However, attention must be paid to the development of shear cracks in the concrete and any depressed concrete surfaces which can lead to premature peeling of the CFRP sheets. The light weight characteristic is also beneficial to repairing older bridges that are carrying much higher loads then they were designed for, and any increase in dead load should be minimized.

2.2.2 Pedestrian Bridges and Walkways

Because of their relatively high cost, currently the most widely used FRP bridge structures are narrow, single-span walkways between buildings or across small rivers or creeks (CSCE 1991). Since the FRP material is light weight (low dead weight) longer spans can be designed and constructed in a short amount of time, thus, lowering their cost

below that of a steel constructed walkway. The University of Pennsylvania, in association with E.T. Techtonics, a firm based in Philadelphia, created a pedestrian bridge at a very competitive cost (Johansen 1990). Low elastic modulus, creep and difficulty in post-construction modifications are some of the known disadvantages of FRP that were considered in this design. Bridges with spans of 7 to 10 m have been constructed with GFRP tube beam trusses, prestressed with Kevlar 49 (aramid) cables. The prestressing of the truss allowed for precambering, thus lower deflections, correction for creep effects and FRP cable changes in diameter and lengths. Therefore, some of these disadvantages were eliminated through engineering design.

2.2.3 Roadway Bridges

TECHNORA brand aramid fibre reinforced plastic (AFRP) rods were used by the Sumitomo Construction Company, in association with the Sumitomo Oyama Research facility, as prestressing tendons in two of their demonstration roadway bridges in the spring of 1990 (Noritake 1991). The first bridge spaned 12.5 m and consisted of three prestressed concrete box girders. Each girder consisted of 16 straight tendon bundles, four in the top flange and 12 in the bottom flange, which in turn consisted of three externally wound 6 mm diameter AFRP rods. Also, each of the beams had 8 mm diameter stirrups made of the same AFRP rods, and attached to the prestressing tendons with plastic ties. No steel was used in any of the three girders. A pretensioning force of

1716.75 kN was applied to the prestressing tendons, accounting for approximately 70% of their tensile strength.

The second bridge spaned 25 m and was 3.59 m wide. It had a single box girder, post-tensioned using ten AFRP internal tendons, five in each web, and six external tendons in the bottom invert. The internal tendons, which were parabolically draped, were made up of 19-6 mm diameter AFRP rods, and the external tendons were made up of 7-6 mm diameter straight AFRP rods. A prestressing force of 588.6 kN was applied to the internal tendons and a prestressing force of 245.25 kN was applied to the external tendons.

2.2.4 Long-Span Bridges

With regard to the advantage of high strength-to-weight ratio that has been noted for FRP materials, as bridge spans increase, so does the advantage of FRP. It is in the area of long-span cable supported bridges that Professor Urs Meier of the Swiss Federal Laboratories for Material Testing and Research (EMPA) in Zurich has proposed some ideas for the use of FRP (Meier 1987). Meier considered the feasibility of constructing a bridge across the Gibraltar Straight at its narrowest point with the use of steel, CFRP and GFRP materials.

As the span of a structural system increases, it approaches its limiting span, where the self weight of the structure alone is enough to fail the system. The limiting spans for

classical suspension bridges using the three materials in question were estimated to be 4490 m, 11560 m and 14580 m for steel, GFRP and CFRP respectively. At this juncture it seems, theoretically, that CFRP should be the choice of the material. Meier further compared the materials with respect to their economic break even points, where a span less then that calculated is considered uneconomical. The study found that any span length less than 4170 m would be most economically built with steel, while spans longer than that would be more economically built with the composite materials, the relative economy increasing with length. The properties of GFRP and CFRP were then compared, and it was shown that the disadvantage of the low elastic modulus of the GFRP was outweighed by the CFRP's high modulus-to-density ratio (highest of all structural materials), its low thermal coefficient, its excellent fatigue life, its high resistance to corrosion and ultra violet irradiation and its low level of creep. The required cable weights for bridges of CFRP and steel were also compared, showing that for longer span structures, CFRP should be the material of choice. There were a few disadvantages noted by Meier in the CFRP use in the structure. Due to the difficulty in CFRP girder fabrication, the aerodynamic stability of the cross section would be decreased. An increase of materials would then be necessary, creating a cross section that would be less than optimum with respect to aerodynamics, thus greatly increasing the lateral wind loads on the structure.

2.2.5 Highway Bridges

As previously mentioned, todays truck loadings are substantially greater than those for which the highway bridges of the 1950's and 1960's were designed. Because of these large loads, and in order to combat the problem of corrosion due to de-icing slats on the roads, the design of future highway bridges must include the use of FRP. Already highway bridges built of composite materials are in use in Germany, China, USA, Japan and Canada. The Trail Bridge in Calgary, Canada, for example, was the first SMART (stress-strain monitored by optical fibre sensors) bridge constructed in Canada using carbon fiber reinforced plastic (Abdelrahman 1995). The CFRP tendons were used to prestress six precast concrete girders. Incorporated in the CFRP tendons were optical fiber sensors, to allow for continuous monitoring of the stresses in the bridge. The span of the bridge girders was 20.8 m and the girders had a T cross-sectional shape.

2.2.6 Special Structures

Around the globe there are special circumstances, either due to environmental, climatic, electrical or load conditions, where the use of FRP can provide an advantage over the more conventional materials. Through education, the engineers of today can be introduced to this material earlier than past engineers and use the knowledge that they have already acquired. As more and more data are received on the FRP's performance, only the engineers lack of imagination and knowledge can stand in their way toward creating improved solutions to many of the future problems that they may face.

The following sections briefly discuss some of the special structures already using FRP around the world.

2.2.6.1 Protection Panels

Salt water areas where pier columns are subjected to sodium chloride deterioration can be protected by simply applying thin FRP sheets, "Protection Panels", around the concrete or steel to prolong their life span. This is beneficial for bridges over salt water and for oil refinerie platforms in the ocean. A U.S. based firm actually produces a steel pile which is encased in a highly compressed FRP (SPI CI 1995). The fibres in this case vary in length from three to six inches, and are randomly placed within the compressed matrix resin. The compressed FRP is strong enough in compression to allow the conventional methods of hammering to be used, and it provides a non-corrosive coating to protect the steel inner core from salt water corrosion.

2.2.6.2 Bridge Enclosures

Bridge enclosures are basically floor decks incorporating of FRP and constructed under the steel girders of a bridge which seals off the environmental effects and in turn decreases the corrosion of the steel, as well as, facilitates inspection and maintenance of the bridge. The initial concept was created by the winner of a 1981 Civil Engineering Competition in the UK (Head 1988). The first system ever installed was done on the A19 Tees Viaduct in Middlesbrough, England in 1989. GFRP panels were chosen for this

application due to their light weight, durability and cost compared to the other possible composites. This concept also helped ignite the idea of "aerodynamic fairings", which is an extension of the bridge enclosure above the deck in order to improve the aerodynamic shape of the bridge (Meier 1991).

2.2.6.3 Tall Chimney and Column Repair

Due to earthquake loading, many tall chimneys and bridge columns become tilted or damaged. To resolve this problem, the Japanese company Mitsubishi Kasei has produced two CFRP products: carbon fibre unidirectional tape and; carbon fibre winding strands (CSCE 1992). Together these products can retrofit chimney's as well as rectangular columns and improve their earthquake loading resistance. The carbon fibre unidirectional tape provides the flexural strength and the strands are used for support. A tall-chimney repair machine was developed by Ohbayashi Corporation which automatically impregnates the carbon fibre strands with resin as it winds the strands around the chimney or rectangular column.

2.2.6.4 Electro-Magnetically Neutral Structures

In certain situations, it is necessary not to have a magnetic field created within a structure. FRP composites are electro-magnetically neutral, and therefore, would be of great use in these situations to replace the metal-bearing conventional materials. Such situations arise in the design of microwave towers, transmission towers, hospitals and computer buildings. A U.S.-based company developed a fiberglass tripod constructed entirely of fiberglass structural shapes, including fiberglass studs and nuts. "The Arch", as it is called, stands 25.6 m high and has a clear span of 48.8 m. The purpose of "The Arch" is to develop antenna patterns for the U.S. Naval Command Control Ocean Systems Center at Point Loma, California, U.S.A.. The previous "Arch", constructed using wood and steel materials, had produced interference (SPI CI 1995).

2.3 MATERIAL PROPERTIES

FRP are composites where a matrix resin and fibres are combined to form a new material. As the high strength of the fibers are combined with the lower strengths of the matrix, the resulting FRP material realizes strengths somewhere between the two, as shown in Figure 2.1. The two components, fibres and matrix, are described below.

2.3.1 Fibres

Fibres are the constituent that carry the loads applied to the material. They provide the stiffness, strength, and as the name FRP implies, reinforcement to the matrix.

These fibres are commonly made from three different materials: Glass, Aramid (Kevlar 49) and/or Carbon/Graphite. Figure 2.2 displays the tensile stress versus strain curves for the three types of fibres. All three fibres show a linear relationship up until a brittle failure, suggesting elastic material behavior. Due to the probability of flaws throughout the lengths of the individual fibres, a wide range of strengths have been reported from tensile tests (Murphy 1994).

2.3.1.1 Glass Fibres

Glass fibres are described physically as a random network of amorphous glass whose surface is highly prestressed in the tensile direction. These fibres possess good mechanical behavior, high strength, high chemical resistance and good insulating qualities. Unfortunately glass fibres also possess poor scratch resistance and therefore, a low bonding strength with the matrix, as well as low elastic modulus and low fatigue resistance. Thanks to their handling during production phases, their mechanical properties and their high strength, stiffness, weathering and electrical resistance's, the type of glass fibres used in most FRP reinforcements for civil engineering applications are the E-glass (Electrical) type. S-glass type fibers have a different chemical composition, resulting in higher tensile strength and elastic modulus than E-glass type fibers. Due to their smaller filament diameters, they also have an improved interlaminar strength than the E-glass type fibers, but are more expensive to produce. Glass fibres are most commonly used in FRP since their cost is lower than the aramid (Kevlar 49) and carbon fibres (Murphy 1994).

2.3.1.2 Aramid Fibres

Aramid fibres are the latest fibres to be used in reinforcing plastics, and are described as semi-loose bundles of long polymer chains in a semiparallel array. The most common type of aramid fibre currently in use is Kevlar 49, developed by the Du Pont company (CSCE 1991). These organic fibres are called poly-paraphenylene terephthalamide, and are thought to be an aromatic polyamide. Aramid fibres possess a low density, high strength and the highest strength-to-weight ratio among the currently used fibres (Murphy 1991). The main disadvantages of these fibres are their low compressive strength and the difficulty of cutting or machining them.

2.3.1.3 Carbon Fibres

Carbon fibres are the most expensive fibres of the three, but they perform best. They possess very high static strengths, high elastic modulii and high fatigue strengths, hence they are used most commonly in prestressing applications (Murphy 1991). Carbon fibres are also the lightest of the three fibres and they maintain their strengths up to temperatures of 2000°C. They also possess low impact resistance and high electrical conductivity.

2.3.2 Matrix

The matrix of the FRP materials is manufactured using thermosetting resins and fillers (with curing agents, hardeners, inhibitors and plastisizers). Curing of the liquid-state thermosetting resins solidifies and hardens the resin around the fibers, and serves as a protector and molder to the fibers for the FRP material (Murphy 1991).

2.4 FLEXURAL BEHAVIOUR OF CONCRETE BEAMS AND SLABS REINFORCED BY FRP REINFORCEMENTS

This section includes studies on the use of FRP reinforcements for reinforced concrete slabs and beams. Since one-way reinforced concrete slabs have a behaviour similar to that of reinforced concrete beams, information on FRP-reinforced concrete beams is included.

Nawy et al (1971) investigated the behaviour of 20 concrete beams reinforced by GFRP and steel reinforcements. The dimensions for all the beams were 180 mm deep and 90 mm wide, with a clear span of 1.83 m. The beams were subjected to four-point loading at the third points of the span. The percentage of reinforcement was varied within the five series of four beams each. Pre-cracking behaviour was similar for both the GFRP and steel reinforced beams. At failure, crack patterns revealed more cracks in the GFRP reinforced beams than in the steel-reinforced ones. However, the observed failure loads for the GFRP reinforced beams were twice as large as those for the similar steel reinforced

beams. The failure cracks for all the GFRP reinforced beams were the outer most diagonal tension cracks observed in the beams. Once the cracks propagated toward the top of the beams, the beam split into two segments and slid apart from each other. Deflections at the ultimate loads of the GFRP-reinforced beams were approximately three times those observed in the steel reinforced beams.

Further testing on the behaviour of 14 simply supported concrete beams reinforced by GFRP bars and two steel-reinforced beams are reported by Nawy and Neuwerth (1977). The cross-sections of all the beams were 127 mm x 305 mm, with a clear span of 3.05 m. The beams were loaded by two concentrated loads at the third points of the span. The principle variable parameter was the percentage of reinforcement, which varied from 0.65% to 2.28%. Only one or two cracks developed in the beams with the smallest amount of reinforcement, while the beams reinforced with the largest percentage of reinforcement, 2.28%, developed a significantly larger number of cracks. The crack spacings for the beams reinforced by GFRP reinforcements averaged 2.75 times the cracks spacings observed in the steel-reinforced beams. Bilinear load-deflection behaviour was observed in all 16 concrete beams, with the post-cracking stiffness of the GFRP reinforced beams being drastically reduced, in comparison to the steel reinforced beams. Evaluation of the effective moment of inertia, based on Equation 2.1, was done using Branson's deflection equation (Branson 1966), based on Equation 2.2.

$$I_e = \left(\frac{M_{cr}}{M_a}\right)^3 I_g + \left(1 - \frac{M_{cr}}{M_a}\right)^3 I_{cr} \qquad \text{Eqn. 2.1}$$

$$\Delta_{max} = \frac{Pa}{24E_cI_e}\left(3L^2 - 4a^2\right) \qquad \text{Eqn. 2.2}$$

Smaller calculated deflection values, in comparison to observed deflections, resulted due to the over-estimated I_e values produced using Equation 2.1. For load levels up to 35% of the ultimate load, observed deflections were within the allowable serviceability limits. Due to the low elasticd modulus, the ultimate strengths of the GFRP bars were never developed.

Benmokrane et al (in print ACI S.J.) completed an experimental study of eight concrete beams reinforced by ISOROD-GFRP and steel reinforcements. Four of the beams were reinforced by ISOROD-GFRP bars, while the remaining four were reinforced with conventional steel rebars. To account for the effective moment of inertia, the ACI equation for the moment of inertia, based on Equation 2.1, was modified based on experimental results, resulting in Equation 2.3.

$$I_e = \alpha I_{cr} + \left[\frac{I_g}{\beta} - \alpha I_{cr}\right]\left(\frac{M_{cr}}{M_a}\right)^3 \quad . \qquad \text{Eqn. 2.3}$$

where:

$\alpha = 0.84$

$\beta = 0.70$

The ultimate moment capacities for the GFRP-reinforced beams were comparable to those for the steel reinforced beams, but within the elastic range the deflections were three times larger in the beams reinforced by GFRP bars.

Masmoudi et al (1996) continued the study of ISOROD-GFRP reinforced concrete members by investigating 12 concrete beams reinforced by ISOROD-GFRP and Kodiak-GFRP bars. The test specimens were simply supported on a simple span of 3000 mm and with cross-sections of 200 mm x 300 mm. Three series, which included two identical beams reinforced by ISOROD and two reinforced by Kodiak reinforcements, of reinforced concrete specimens with percentages of reinforcements of 0.5%, 0.75% and 1.07%, were tested in this program. Cracks which formed outside the constant moment zone in all of the beams, initiated as flexural cracks, then developed inclined cracks as the loads were increased. As the percentage of reinforcement was increased, so did the number of observed cracks, thus, the crack spacing and widths decreased. The cracking moment was not affected by the type or percentage of reinforcement. The crack widths could be predicted using the Gergely-Lutz equation, based on Equation 2.4.

$$w = K_g f_s \frac{h_2}{h_1} \sqrt[3]{d_c A} \times 10^{-6} \qquad \text{Eqn. 2.4}$$

Faza and GangaRao (1992) reported studies on the pre- and post-cracking behaviour of GFRP and steel reinforced concrete beams. The test program consisted of 25 rectangular concrete beams, 152.4 mm x 304.8 mm, reinforced by Kodiak-GFRP bars and tested under four-point loading conditions. Five variable parameters were investigated, including:

1) four bar sizes;
2) three types of bar surface conditions;
3) three types of stirrups;
4) two percentages of reinforcement; and
5) five compressive concrete strengths.

As in many of the previously reported studies, the cracking moment was unaffected by the reinforcement type or ratio. However, the sand-coated bars provided improved flexural behaviour compared to that for the remaining surface types. The deflections observed in the GFRP-reinforced concrete beams averaged four times those observed in the steel reinforced beams. The sand-coated bars also improved the control of the crack widths, in comparison to the two other surface conditions. After the initiation of the first crack, the

effective moment of inertia equation provided by the ACI, based on Equation 2.1, produces a large over-estimation, thus, lower predicted deflections, as compared to the observed behaviour. A modified moment of inertia was proposed, based on Equation 2.5, which assumes the GFRP-reinforced beams are fully cracked between the two concentrated point loads, and partially cracked outside the constant moment zone.

$$I_m = \frac{23 I_{cr} I_e}{8 I_{cr} + 15 I_e} \qquad \text{Eqn. 2.5}$$

Use of this modified moment of inertia results in a deflection equation, based on Equation 2.6, for a beam loaded at its third points of the span.

$$\Delta_{max} = \frac{23 P L^3}{648 E_c I_m} \qquad \text{Eqn. 2.6}$$

The modified deflection equation more accurately predicted the load-deflection behaviour of the tested beams.

2.5 DESIGN CONSIDERATIONS

Although many concrete structures already include GFRP reinforcements, they have been designed conservatively. Since most of the current codes require strains in the

steel reinforcements to achieve the yield strain prior to failure, design codes must be modified to consider the material characteristics of FRP. Since FRP reinforcements do not possess a yield point, new design approaches must be developed.

Many studies, based on GFRP reinforcements, have developed modified moments of inertia and/or crack width equations (Nawy et al 1971, Nawy and Neuwerth 1977, Benmokrane under press, Masmoudi 1996 and Faza and GangaRao 1992). However, each study developed a different empirical formula based on their individual test programs. Until many tests on the same specific GFRP bar types have been completed, with accurate formulae being derived, strain compatibility can be used to analyze the flexural behaviour of the GFRP reinforced concrete members.

2.5.1 Flexural Behaviour

Nanni (1993) reviewed the design procedure necessary to accommodate the use of FRP bars as the reinforcement of reinforced concrete members. He suggested that the working stress design approach should be considered when designing with FRP reinforcements. This is due to the linear stress-strain behaviour of the material up until failure. Using derived properties based on uniaxial tension tests, idealized material properties were developed to analyze the flexural behaviour of FRP-reinforced concrete members. Since FRP bars do not yield prior to failure, the failure criteria must be designed for crushing of the concrete prior to rupture of the FRP reinforcement. Due to

the low elastic modulus of FRP reinforcements, in comparison to steel rebars, deflection control is the controlling parameter. The crack widths must also be controlled. To ensure safe designs, confidence in the manufacturer's published properties must be established. Therefore, standardized testing must be established.

Using the stress-strain properties of GFRP reinforcements, the one-way concrete slabs can be analyzed based on the strain compatibility approach. This approach has been observed by many researchers (Mutsuyoshi et al 1990 and GangaRao and Faza 1983) to produce accurate results. Prediction of the cracking and ultimate moments and the failure modes can be made with good correlation to experimental results. The cracking and ultimate moments for GFRP reinforced concrete members can be calculated using Equations 2.7 and 2.8, based on Figure 2.3.

$$M_{cr} = \frac{f_R I_g}{y_b} \qquad \text{Eqn. 2.7}$$

$$M_u = Td - Cc \qquad \text{Eqn. 2.8}$$

where:

M_{cr} = cracking moment.

f_R = tensile strength of concrete.

T = equivalent tensile force at the level of FRP reinforcement.

C = equivalent compressive force in the compression zone.

c = distance from the extreme compression fibers to the centroid of the compressive force in the compression zone.

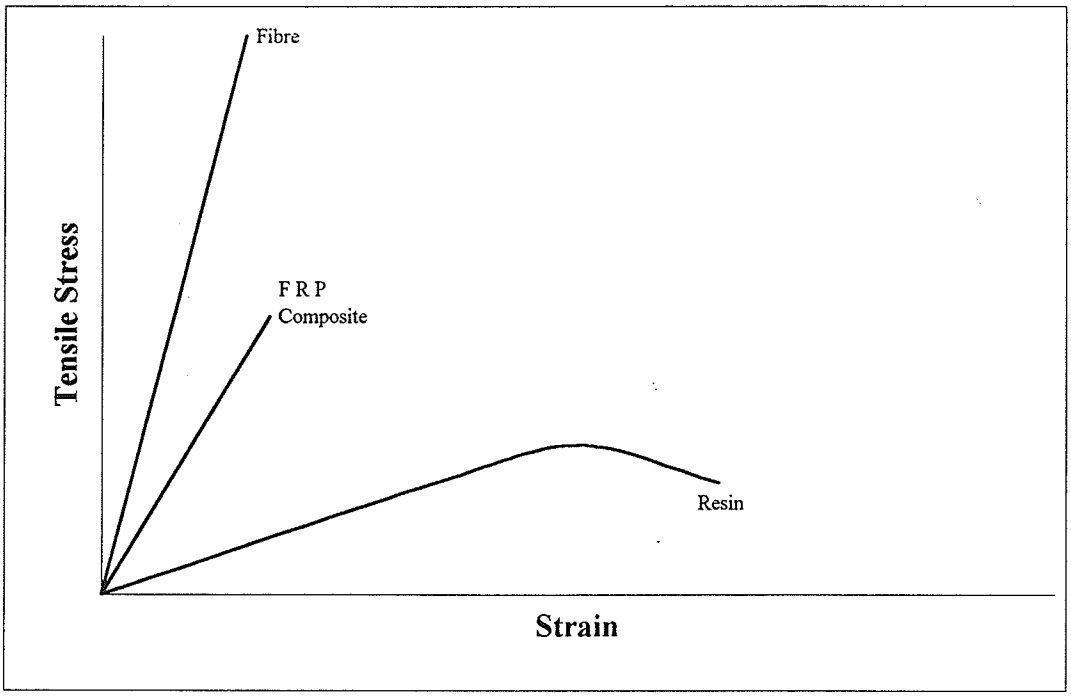

Figure 2.1: Stress-strain relationship of the FRP components.

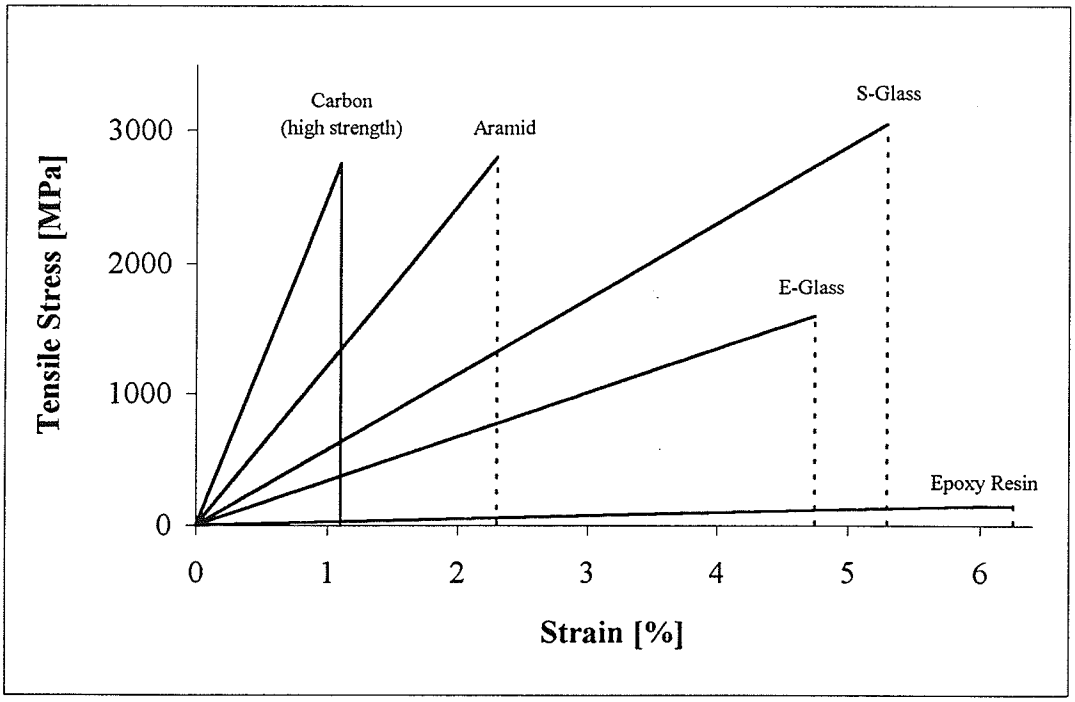

Figure 2.2: Stress-strain relationship of the fibres and epoxy resin.

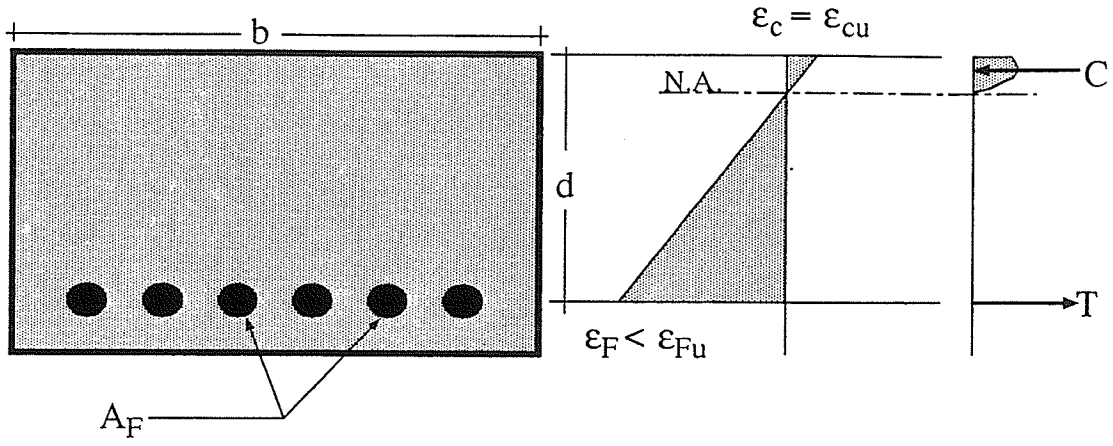

Strain and stress distribution at crushing of concrete

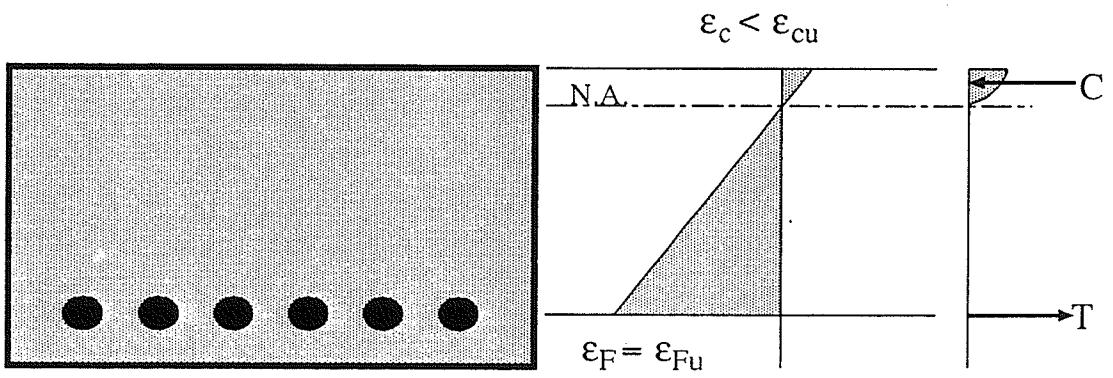

Strain and stress distribution at rupture of GFRP bars

Figure 2.3: Strain and stress distributions for different failure modes of one-way concrete slabs reinforced by GFRP bars.

CHAPTER 3

EXPERIMENTAL PROGRAM

3.0 GENERAL

The experimental program was designed to evaluate the flexural behavior of one-way concrete slabs reinforced by GFRP bars. In this investigation, ISOROD-GFRP reinforcements, produced by Pultrall Inc., Thetford Mines, Québec, Canada, were used. The three modes of failure considered in this investigation were: crushing of the concrete while the GFRP bars remain elastic; rupture of the GFRP bars prior to crushing of the concrete and; simultaneous rupture of the GFRP bars and crushing of the concrete. A total of eight slabs were tested in this program, and are described in Table 3.1. The slabs were tested under four-point static loading conditions, using two concentrated loads at the third span points. Five slabs were reinforced by ISOROD-GFRP bars, two slabs were reinforced by conventional steel rebars and one slab was reinforced by Leadline-CFRP

rods, produced by Mitsubishi Kasei, Japan. The three slabs reinforced by steel and CFRP reinforcements were used as control slabs for behavior comparisons.

The parameters considered in evaluating the flexural behavior include:

1. Failure mode of the slabs
2. Percentage of reinforcements
3. Thickness of the slabs
4. Crack widths

3.1 TEST SPECIMENS

3.1.1 Design of Specimens

The slab lengths and widths were kept constant throughout the study. The slabs' overall dimensions conform to Canadian Design Code (CSA 1984) in terms of span-to-thickness ratio. The length of the slabs was selected to match spans of beams tested in a parallel study at Sherbrooke University using ISOROD-GFRP bars (Benmokrane under press). Given the length and width of the slabs, the design of the slabs was completed by calculating the necessary percentage of reinforcement needed to produce the three desired failure modes.

The slabs were divided into three series, A, B and C, according to their designed failure mode, in order to examine the influence of ISOROD-GFRP bars on the flexural behavior of the slabs.

The notation used for the tested slabs was selected to describe the following parameters:

(a) Type of reinforcements: I = ISOROD-GFRP bars

S = Steel rebars

LL = Leadline-CFRP rods

(b) Thickness of the slab: 150 = 150 mm

200 = 200 mm

(c) Expected mode of failure: A = Rupture of reinforcements

B = Balanced

C = Crushing of concrete

The dimensions of the slabs and the reinforcement details are shown in Figures 3.1 and 3.2. The length and width of all the slabs were 3500 mm and 1000 mm respectively.

This allowed a clear span of 3000 mm for the static four point loading condition. The two thicknesses investigated in the study were 150 mm and 200 mm.

3.1.2 Longitudinal Reinforcement

The longitudinal reinforcements were placed in the slabs at spacings according to the Canadian Design Code (CSA 1984) and were extended 100 mm past the slab ends to facilitate monitoring of any possible slippage during testing.

A 102 x 102 MW25.8 x MW25.8 welded wire mesh was also placed in the upper portion of the slabs, following common practice when casting slabs.

3.1.3 Transverse Reinforcement

All the transverse reinforcements were the same material as the longitudinal reinforcements, and were spaced on top of the longitudinal reinforcements according to the Canadian Design Code (CSA 1984).

3.2 MATERIAL PROPERTIES

3.2.1 Concrete

The concrete used in all the slabs was designed for a nominal strength of 30 MPa after three days, and provided by local ready mix concrete company, Perimeter Concrete Ltd.. The mix design had the following proportions:

Coarse Aggregate (max. 14 mm diam.)	1149.6 kg/m^3
Fine Aggregate (passing #4 sieve)	679.8 kg/m^3
Portland Cement	400 kg/m^3
Water	148.5 kg/m^3
Superplastisizer (Reobuild 1000)	3* kg/m^3
(Water/Cement Ratio = 0.37)	

* approximate value

The specified slumps before and after the addition of the superplastisizer were 40 mm and 180 mm respectively. Three standard cylinders of dimensions 150 mm x 300 mm and three concrete beams of dimensions 150 mm x 150 mm x 650 mm, were cast according to ASTM C39-86 and ASTM C78-84, respectively, for each slab in order to monitor the concrete strengths. At the time of testing, the cylinders were tested for the compressive strength of the concrete and the beams were tested for the rupture strength of concrete in tension.

3.2.2 Longitudinal and Transverse Reinforcement

3.2.2.1 ISOROD-GFRP Bars

ISOROD brand name GFRP bars are fabricated through a pultrusion process of continuous E-glass fibres and a thermosetting polyester resin. To enhance the bond properties, an outer spiral wrapping of glass fibres and a sand coating are added to the core of the ISOROD-GFRP bars. All of the ISOROD-GFRP bars used in this study had a nominal ultimate tensile strength of 690 MPa determined by tests conducted at the University of Sherbrooke (Chaallal and Benmokrane 1993). Measured properties of the deformed ISOROD-GFRP bars were tested using three samples each of the 12.7 mm and 15.9 mm diameter bars. Tension tests were also conducted at the same time at the University of Manitoba by Grieef (1996) on smooth ISOROD-GFRP bars using diameters of 19.1 mm and 25.4 mm. A similar coupler grip system, shown in Figure 3.3, was used for both the deformed and smooth bar tests. Through the use of a mixture of an epoxy resin, West System Epoxy Resin 105, and a hardener, West System Hardener 205, a protective coating was formed on the ends of the FRP tension test specimens for the previously mentioned coupler grip system. This system allows for successful tension tests on FRP specimens, while using conventional machinery, as shown in Figure 3.4.

3.2.2.2 Leadline-CFRP Rods

The guaranteed nominal tensile stress is 1970 MPa and ultimate elongation is 1.3% (Mitsubishi Kasei 1992). The measured ultimate tensile strength and ultimate strain based

on tests conducted at the University of Manitoba were 2950 MPa and 1.3% respectively (Abdelrahman 1995). All of the test results are presented in Chapter 4.

3.2.2.3 Mild Steel Rebars

All of the steel rebars used in the study were Grade 400W. The nominal yield strength of the bars is 400 MPa. The measured yield and maximum strength of the rebars were obtained through tension tests following ASTM , and are presented in Chapter 4.

3.3 INSTRUMENTATION

3.3.1 Longitudinal Reinforcement Strain Measurements

To measure the strains in the longitudinal reinforcement during the testing, N11-FA-5-120-11 electrical 120 ohm resistance strain gauges, produced by Showa Measuring Instruments Co., Ltd., of Japan, were placed directly on the GFRP and CFRP reinforcements. The gauge length was 5 mm and the gauge factor was 2.12 ± 1%. The strain gauges were covered with an air-drying acrylic coating, a nitrile rubber coating and a butyl rubber caulking to protect the gauges from water intrusion during casting. The location of the strain gauges is shown in Figure 3.5(a).

3.3.2 Concrete Strain Measurements

Stainless steel DEMEC points were attached to both sides of the slab at the level of reinforcements using an epoxy resin to measure the strain in the concrete. There were three DEMEC point stations on each side of the slab within the flexural zone, as shown in Figure 3.5(b). Strain readings were taken manually using a DEMEC gauge of 200 mm gauge length.

To measure the strain in the concrete at the top of the slabs, stainless steel DEMEC points were attached to the top surface of each slab using an epoxy resin. Twelve DEMEC point stations were located within the flexural zone and manual strain readings were taken with the use of a DEMEC gauge of 200 mm gauge length. The locations of DEMEC point stations on the top the slab are illustrated in Figure 3.5(c).

3.3.3 Deflection Measurements

Deflections were measured at the midspan of all slabs with the use of a linear variable differential transducer (LVDT). An LVDT with a range of ±38mm was attached to a steel arm supported by a steel column. The LVDT was placed against an aluminum plate which was attached to the top surface of the slab using an epoxy resin. This configuration is shown in Figure 3.6.

3.3.4 Crack Width Measurements

Crack widths were measured on the bottom surface of the slab at two positions along the crack, and then averaged. The measurements were taken using either a Wild M5-63661 microscope, with an accuracy of ±0.01 mm, balanced on a swivel arm system or with a hand held Brinell microscope, with an accuracy of ±0.05 mm.

3.3.5 Slip in longitudinal reinforcement

Two dial gauges were placed on either side of two or three reinforcement bars on each slab to monitor the relative slippage of the longitudinal reinforcement with respect to the concrete. A 75 mm diameter steel washer was attached to the end surface of the slab with epoxy resin to support the magnetic base of the dial gauge. Manual readings were taken throughout the test. The dial gauge setup is shown in Figure 3.7.

3.3.6 Data Acquisition System

All of the strain gauge, LVDT and actuator load and stroke readings were monitored continuously throughout the tests using one data acquisition system. The system consisted of an IBM compatible 386 computer, a six volt amplifier and a Validyne Data Acquisition system. All the data was stored in a file during the test and were also displayed graphically on the computer screen during the test, allowing the monitoring of the load-deflection and strain gauge readings. The graphical displays were done using the

data acquisition software program "Labtech Notebook". All the data stored to the file were later transferred to floppy disks for later analysis.

3.4 FABRICATION OF THE SPECIMENS

All of the slabs were fabricated at the Structures Research and Development facility at the University of Manitoba. A wooden form, shown in Figure 3.8, was designed to allow the casting of one 150 mm and one 200 mm thick slabs simultaneously. The forms were cleaned and lubricated with Pre-Form oil prior to the placement of the reinforcements, to facilitate the release of the slabs from the forms after curing.

The longitudinal reinforcements were placed in the forms, held in position by plastic chairs and the end portions of the wooden forms. The transverse reinforcements were placed on top of the longitudinal reinforcements and attached with metal ties. Wooden braces were placed around the forms to suspend the steel wire mesh in position.

Standard slump tests were performed at the arrival of the ready-mix concrete. A range of ±15% of the specified slumps before and after the addition of the superplastisizer was allowed. The concrete was vibrated through the use of a hand held vibrator to help avoid any honeycombing, and to move the concrete around the numerous reinforcements in the forms. The top surface of the slabs was smoothened by spreading cement and water, followed by troweling using steel trowels. A plastic tarp covered the slabs for

approximately four days after casting for curing, during which, water was sprinkled daily on top of the surface. The wooden forms were removed and the slabs were allowed to cure in the laboratory atmosphere for at least another 24 days prior to testing.

The six standard cylinders and beams were cured in the same environments as the slabs. The minimum age of the slabs prior to testing was 28 days.

3.5 TEST SETUP

The slabs were tested in a structural steel loading frame constructed for this study at the Structures Research and Development Laboratory at the University of Manitoba. Six structural steel columns were prestressed, with the use of four Dywidag bars per column, to the structural floor. Four of the six columns were used for the supports and two were used to support the 1000 kN MTS actuator, as shown in Figure 3.9. Each support consisted of a 1010 mm long, 38 mm diameter solid steel bar placed on top of a square hollow structural steel section, which was bolted to the supporting structural steel columns. A flat 13 mm thick, 150 mm wide and 1010 mm long steel plate was placed on top of the steel bar to form a roller support system. Wooden wedges were used to hold the plates in position while the slabs were maneuvered into position on top of the supports with the use of an overhead crane. A spreader beam system consisting of three square hollow structural steel sections, as shown in Figure 3.9, was used to transmit the loads to the slabs. Quick-set plaster of paris mixed with water was used between the two sections

of the spreader beam system and the slabs to ensure a uniform load transmittal. Several 25 mm thick rubber plates were placed between the actuator contact and the spreader beam system to allow for minor rotational movement.

3.6 TESTING PROCEDURE

Once the slab was leveled and properly aligned through the use of an overhead crane, the LVDTs and strain gauges were connected to the data acquisition system. The remaining instrumentation was then placed into position, just prior to the commencement of the test, in order reduce any risk of damage. All instrumentation was checked and zeroed prior to the start of testing.

All the slabs were tested under static conditions and monotonically loaded under stroke control. The stroke rate was set at 0.6 mm/min. up until the initiation of cracking, and was doubled to 1.2 mm/min. for the remainder of the test. At certain load increments, the stroke was held constant while DEMEC point station and dial gauge readings were taken. As the development and propagation of the cracks occurred, they were marked and measured for width at the same load increments as the other manual readings were taken.

Table 3.1: Details of the test slabs.

Thickness mm	Reinforcement	Mark No.	ρ^* %	Trans. reinf.	Predicted Mode of Failure	Test Date	Observed Mode of Failure
150	Steel	S-150-T	.962	15 - No. 10M rebars	Yield	Nov 21/94	Yield
	ISOROD	I-150-A	.487	15 - 9.5 mm diam. ISOROD bars	Rupture of Reinf.	Apr 22/95	Rupture of Reinf.
		I-150-B	.764		Balanced	Jul. 10-95	Rupture of Reinf.
		I-150-C	.955		Crushing of Concrete	Jan 19/95	Shear
200	Steel	S-200-T	.390	22 - No. 15M rebars	Yield	Apr 6/95	Yield
	ISOROD	I-200-A	.230	22 - 9.5 mm diam. ISOROD bars	Rupture of Reinf.	Apr 21/95	Rupture of Reinf.
		I-200-C	.774		Crushing of Concrete	Feb 6/95	Shear
	Leadline	LL-200-C	.303	33 - 8 mm diam. Leadline rods	Crushing of Concrete	Jul. 12/95	Bond

Typical clear span length = 3000 mm Typical width = 1000 mm

$$*\rho = \frac{Area\ of\ reinforcements}{bd}$$

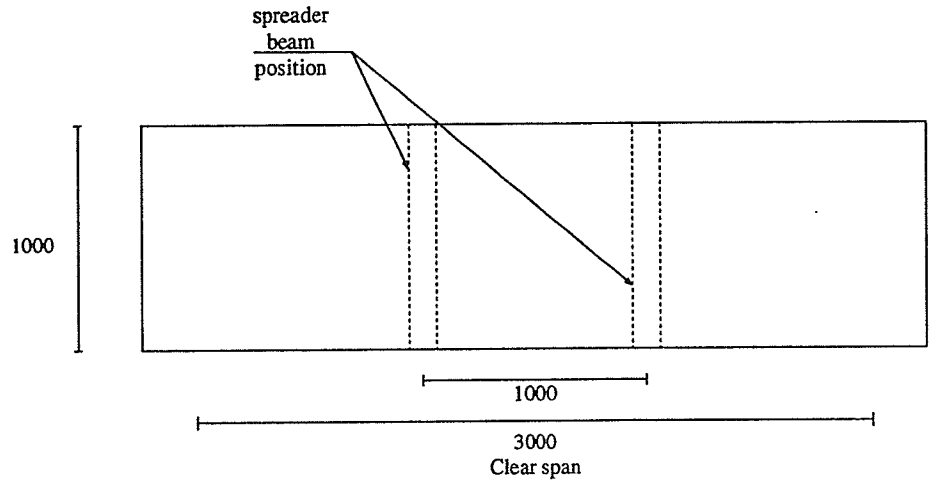

(a) Typical slab top view

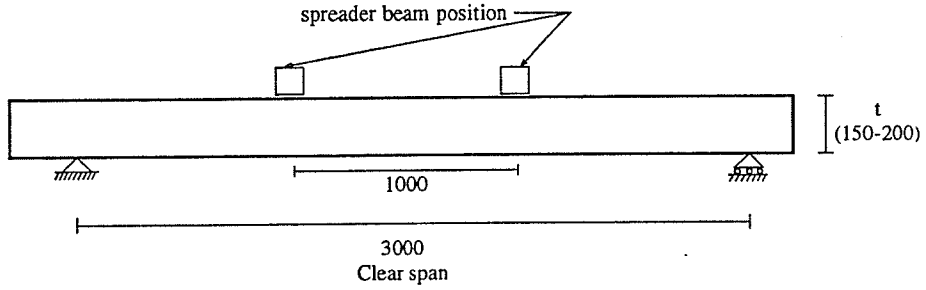

(b) Typical side view of slabs

Figure 3.1: Dimensions of the test slabs.

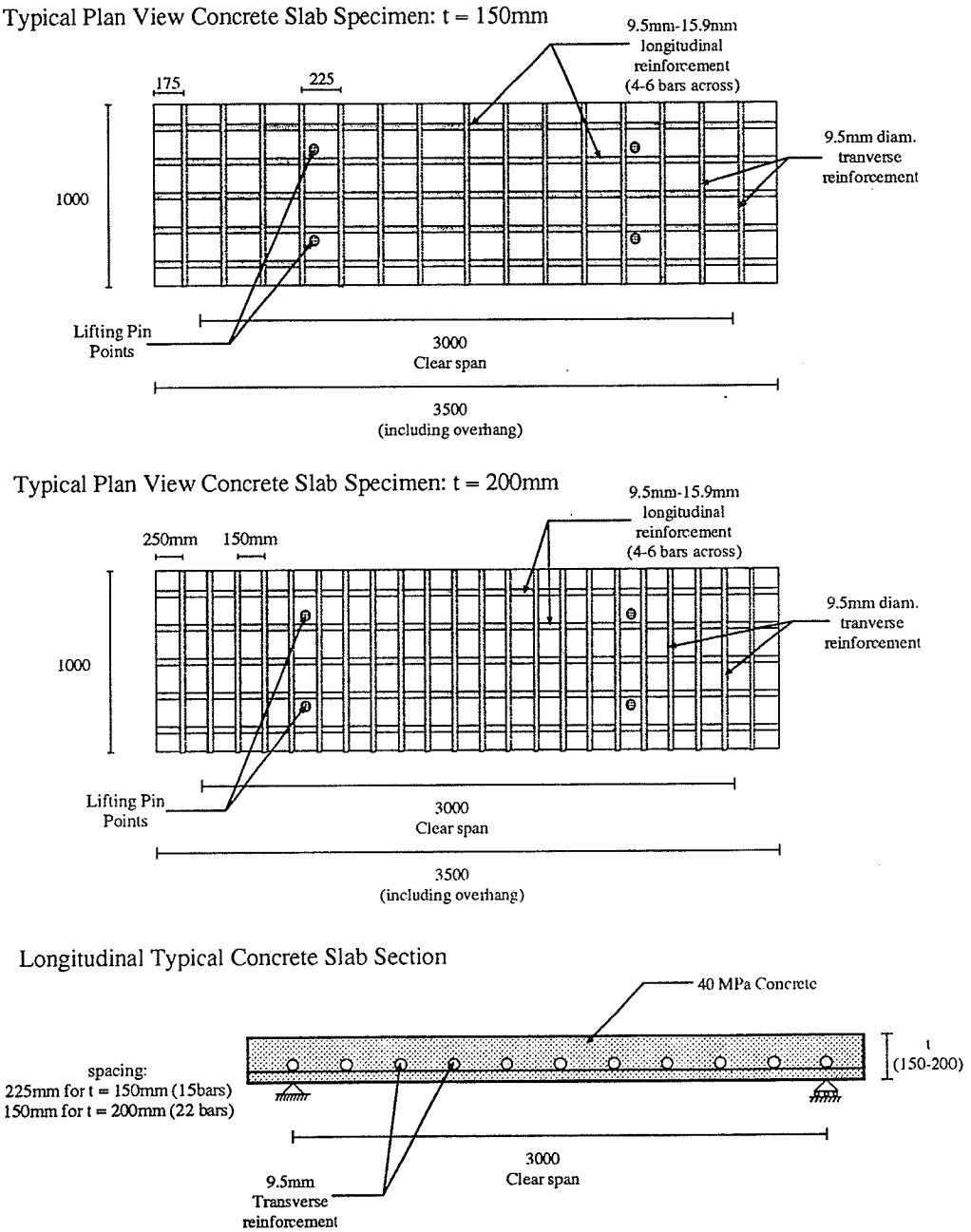

Figure 3.2: Reinforcement details of the slabs.

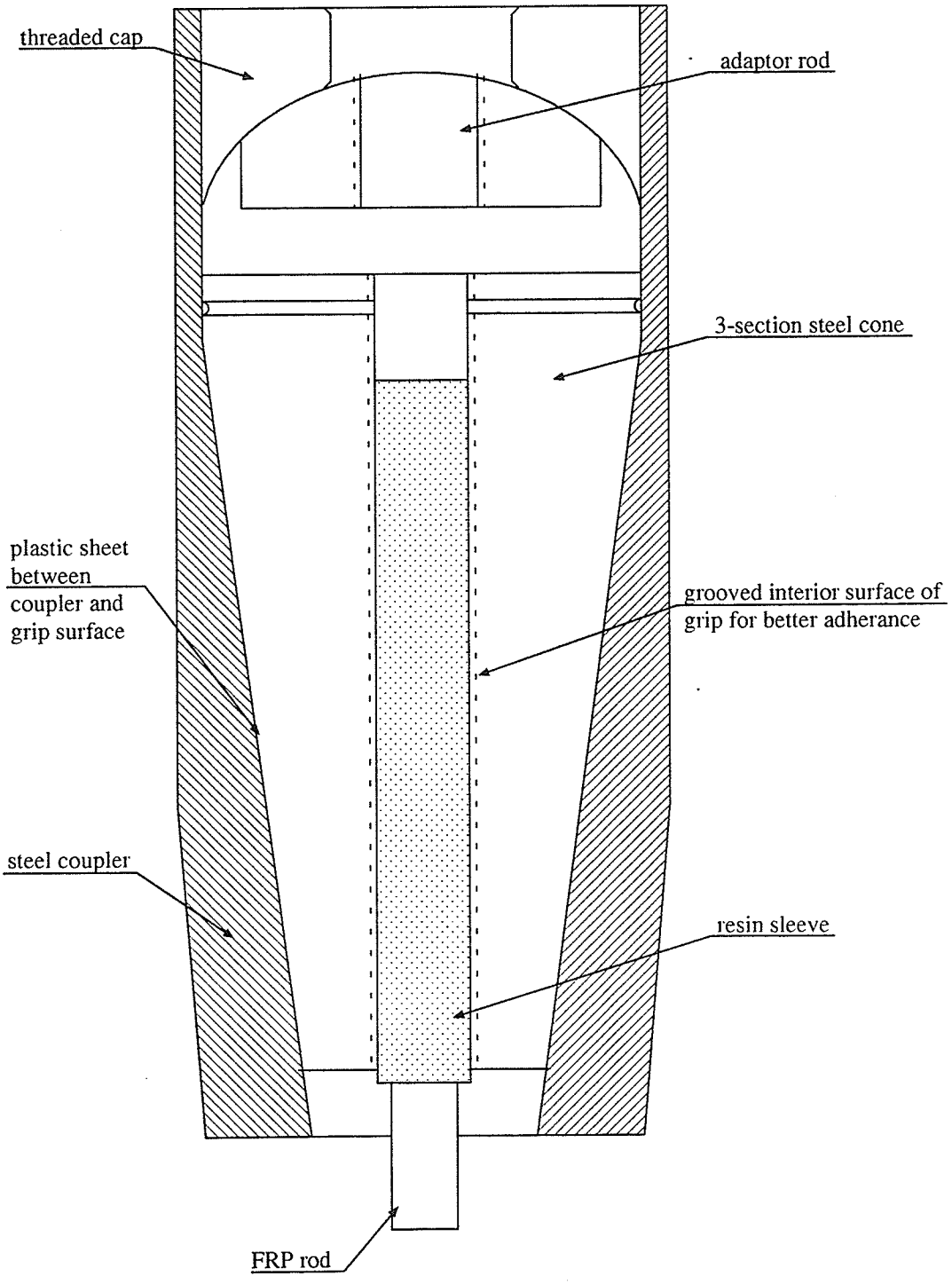

Figure 3.3: Schematic of the coupler grip system used for the FRP tension tests.

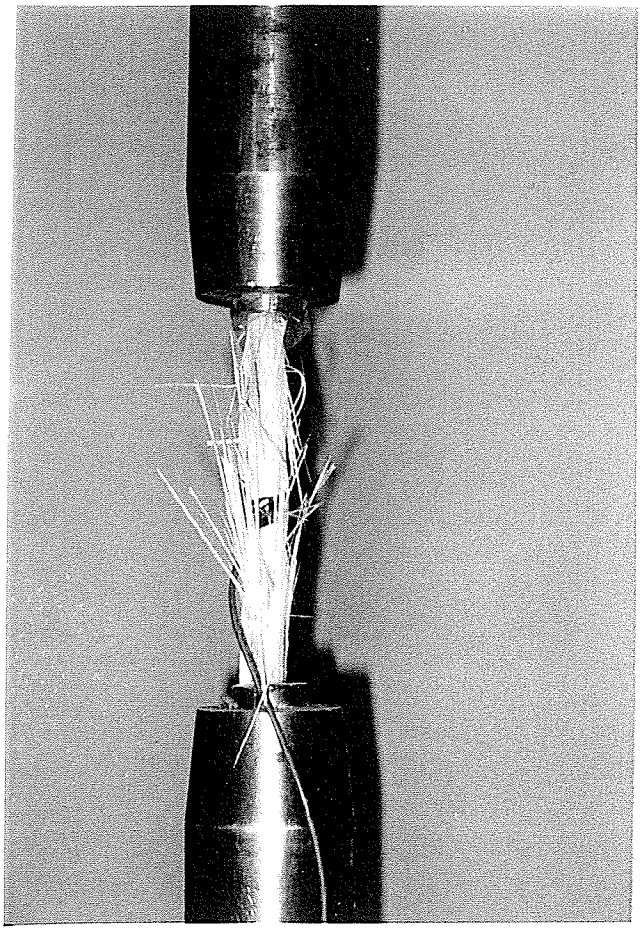

Figure 3.4: Photo of a successful tension test performed on ISOROD.

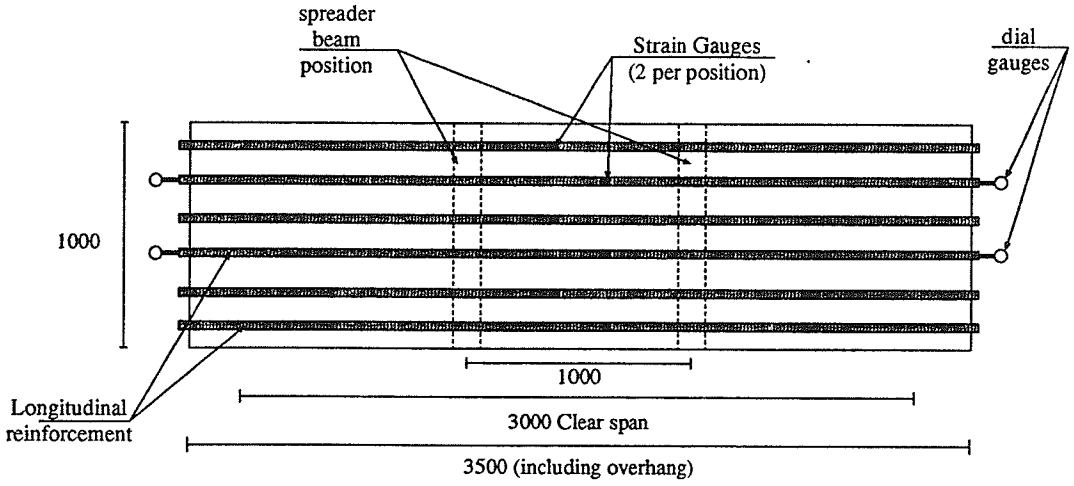

(a) Strain Gauges

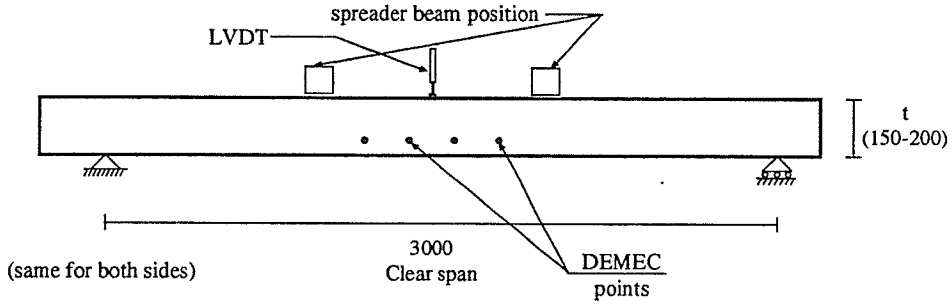

(b) DEMECS at Reinforcement Level

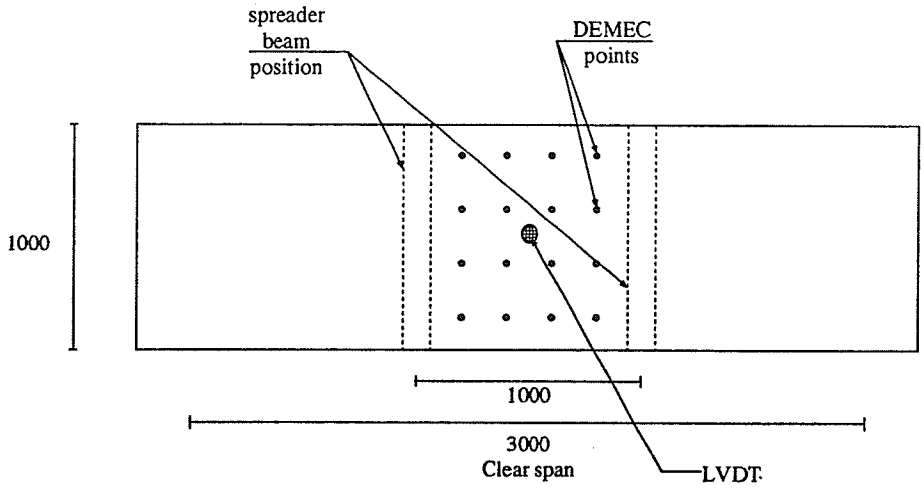

(c) DEMECS at Top of Slab

Figure 3.5: Location of the strain gauges and DEMEC point stations.

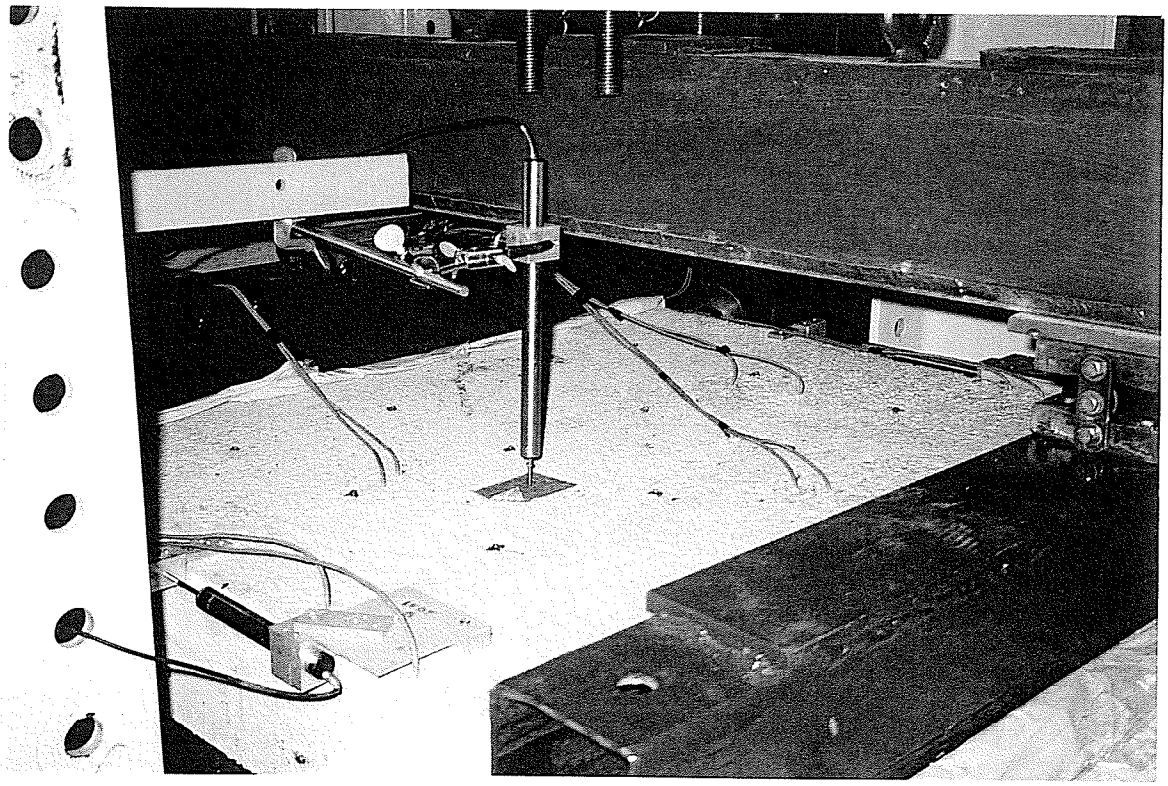

Figure 3.6: LVDT configuration for midspan deflection measurements.

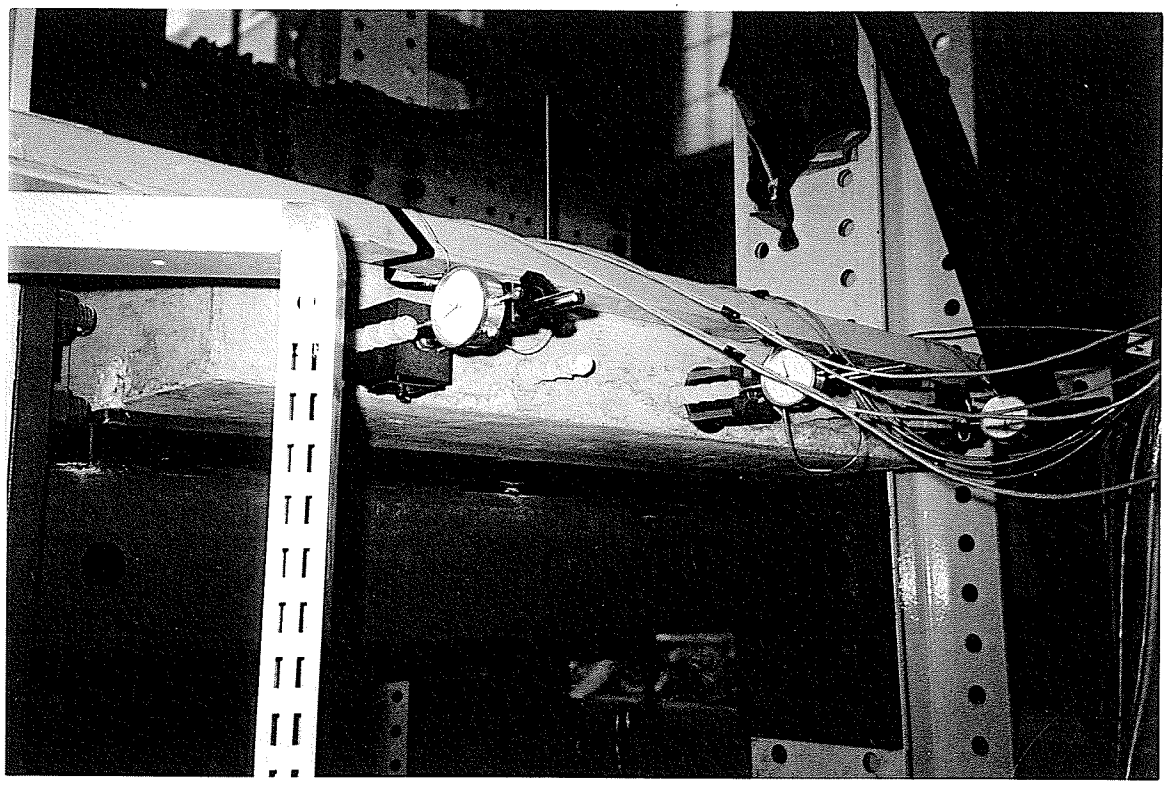

Figure 3.7: Dial gauge setup for end slippage of the reinforcements.

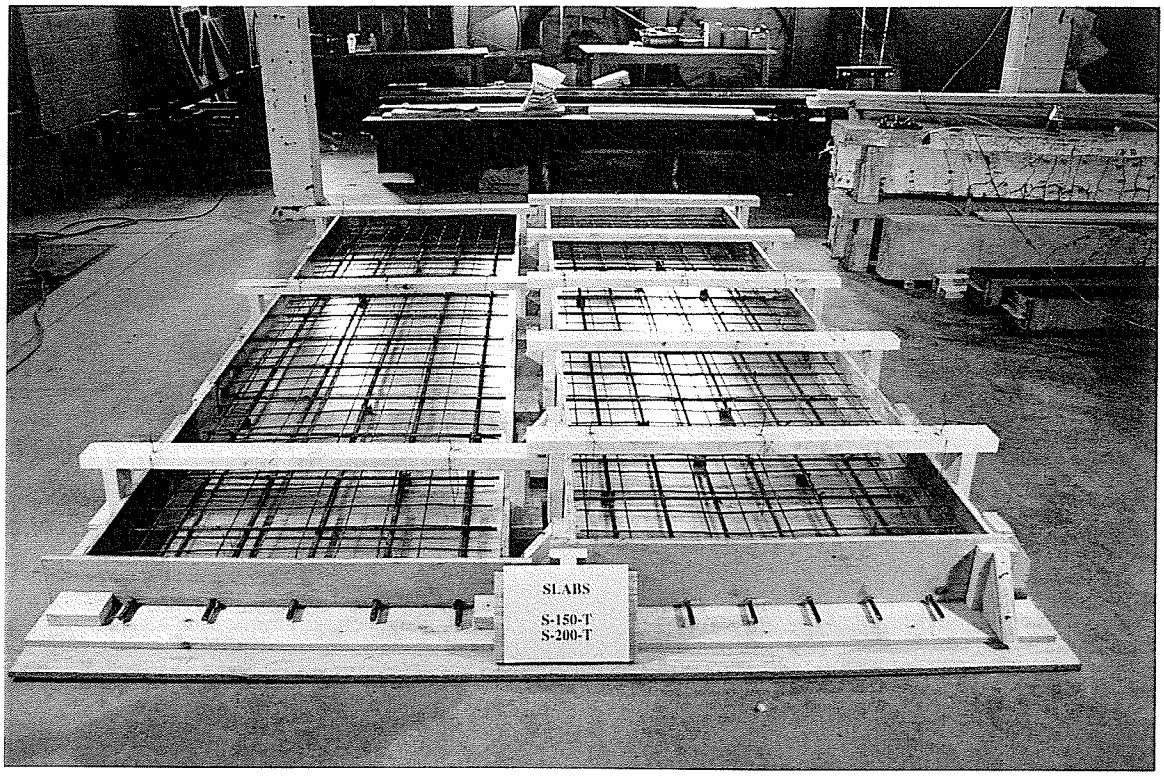

Figure 3.8: The wooden forms used for casting all the test slabs.

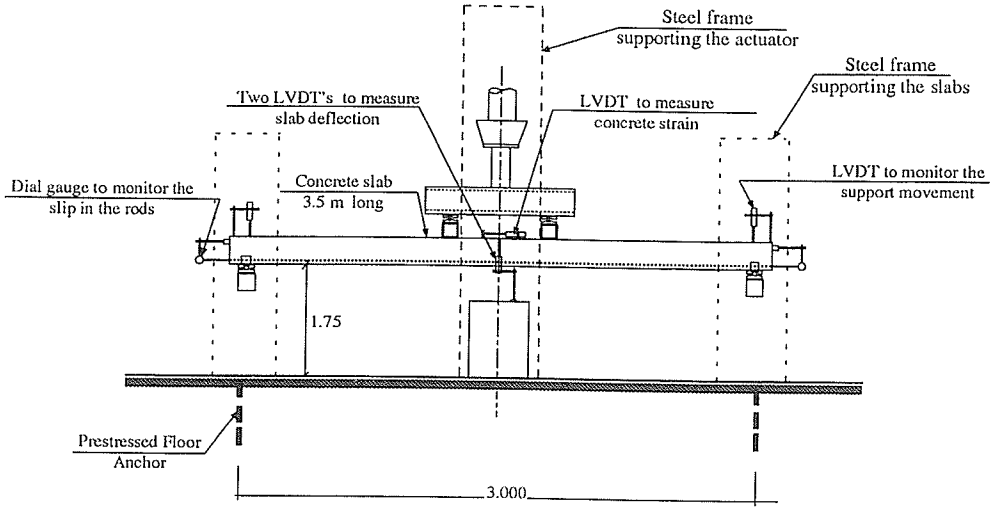

Figure 3.9(a): Schematic of the test setup.

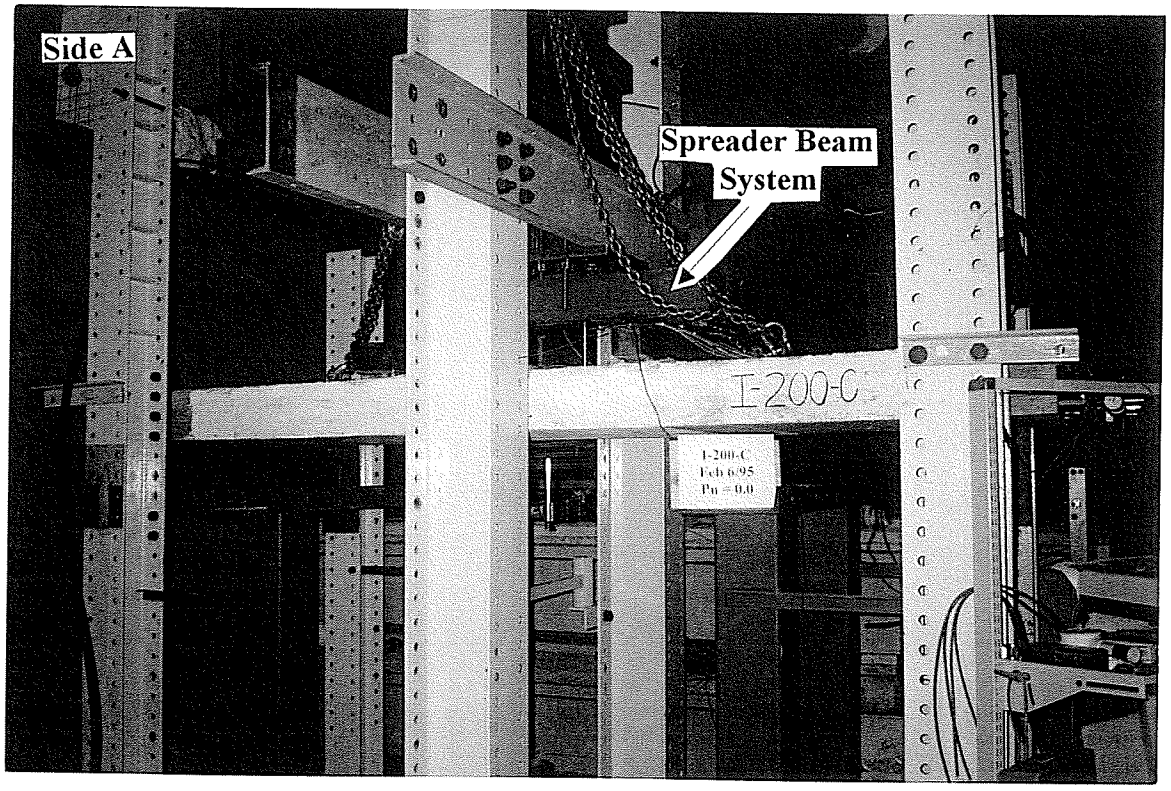

Figure 3.9(b): Test setup.

CHAPTER 4

EXPERIMENTAL RESULTS

4.0 GENERAL

Presentation of the measured material properties tested in this program and the experimental results of the eight slabs are included in this chapter. The material properties were measured for the concrete, steel rebars, ISOROD-GFRP reinforcements and the Leadline-CFRP rods used in this program. The experimental results include the load-deflection behaviour, strain in the reinforcements, strain in the concrete at the level of reinforcements, strain of the outer-most compression fibres of the slabs (top of slab), crack patterns and reinforcement slippage with respect to both ends of the slabs.

4.1 Material Properties

4.1.1 Concrete

The compressive and tensile strengths of the concrete achieved for each slab are presented in Table 4.1. All values reported are the strengths at the time of testing. Four sets of concrete were used for the eight slabs (i.e. two slabs per cast).

4.1.2 Steel Rebar

The tensile stress-strain behaviour and strengths of the 10M steel rebars is presented in Figure 4.1. The yield stress and strain, and the ultimate stress and strain values, obtained during tension tests at the University of Manitoba, were 435 MPa, 0.246 %, 700 MPa and 0.800 % respectively. The measured elastic modulus is 176.8 GPa. The yield stress and elastic modulus provided from the manufacturer were 400 MPa and 200 GPa respectively. Although 15M rebars were also used, not enough material was available for tension testing. The 10M and 15M rebars, used in this test program, were delivered in the same order and were fabricated by Cowin Steel Co.Ltd., Winnipeg, Manitoba, Canada.

4.1.3 ISOROD-GFRP bars

The tensile stress-strain behaviour and strengths of the ISOROD-GFRP reinforcements are illustrated in Figure 4.2. Table 4.2 presents the tensile strength values obtained from tension tests performed on 12.7 mm, 15.9 mm, 19.1 mm and 25.4 mm

diameter deformed ISOROD bars at the University of Manitoba and at Sherbrooke University (Chaallal and Benmokrane 1993), as well as, 19.1mm and 25.4 mm diameter smooth ISOROD bars at the University of Manitoba (Grieef 1996). The tension tests performed at the University of Manitoba on the 9.5 mm diameter ISOROD reinforcements were unsuccessful, due to excessive slippage in the grip system. Due to premature anchorage failures in the tests performed at the University of Manitoba, the averaged tensile strength value of 692 MPa, obtained by Chaallal and Benmokrane (1993), for the ISOROD bars is used for analysis purposes. All ISOROD reinforcements used in the longitudinal and transverse directions were fabricated at the same time by Pultrall Inc., Thetford Mines, Québec, Canada.

4.1.4 Leadline-CFRP rods

The tensile stress-strain behaviour of Leadline-CFRP rods is illustrated in Figure 4.3, and the tensile properties of the Leadline rods is given in Table 4.3. These properties are the values provided by the manufacturer, Mitsubishi Kasei, Japan (1992), and the results from testing done at the University of Manitoba (Abdelrahman 1995).

4.2 Overall Test Results

In general, all the ISOROD-GFRP reinforced slabs exhibited linear behaviour prior to cracking, followed by sudden, wide and deep cracks accompanied by large deformations. A detailed description of the load-deflection, crack pattern, strain and

failure mode behaviours of each slab is given in the following sections. All observations are given with respect to Side A of each slab, and the step-wise reduction in load resistance, ΔP, is given as a percentage of the respective cracking loads, P_{cr}, for each slab.

4.2.1 Load-Deflection Behaviour and Crack Development

The load-deflection behaviour of all eight slabs throughout the entire program, along with predicted values, are shown in Figures 4.4 to 4.11. Measured data presented in the figures also includes the midspan self-weight loads of 10.6 kN and 14.1 kN for the 150 mm and 200 mm thick slabs respectively. The following sections describe the load-deflection and crack development behaviour of each individual slab in detail.

4.2.1.1 Slab I-150-A

Slab I-150-A consisted of a 1000 mm wide one-way slab with a thickness of 150 mm, producing a cross-sectional area of 150 000 mm^2. A cross-section of slab I-150-A is illustrated in Figure 4.12(a), showing the placement of the reinforcements, which consisted of four 12.7 mm diameter ISOROD-GFRP bars in the longitudinal direction and 15 - 9.5 mm diameter ISOROD-GFRP bars in the transverse direction, fulfilling the requirements of the Canadian Design Code (CSA 1994). Slab I-150-A was originally designed to fail by rupturing of the GFRP bars prior to crushing of the concrete according to the Canadian Design Code (CSA 1984).

Prior to the initiation of cracking, the slab exhibited linear behaviour as shown in Figure 4.4. The initial loading rate was set at 0.6 mm/min. to allow for proper observations prior to the initiation of cracks. Initiation of cracking occurred at a load resistance of 24.1 kN and a midspan deflection of 1.25 mm. All the cracks that developed in slab I-150-A are shown in Figures 4.13 and 4.14. The initial crack, crack 1, was observed within the constant moment zone approximately 50 mm inside the left loading point. The immediate height of the crack was 135 mm straight vertical. Once the crack occurred, the load resistance immediately reduced to 12.2 kN (53.5% reduction with respect to the cracking load).

The application of load was continued until crack 2 developed within the constant moment zone, at a load resistance of 28.2 kN, approximately 50 mm inside the right loading point with a height of 130 mm. The load resistance instantly reduced to 20.5 kN (32.0% reduction) and a total midspan deflection of 10.00 mm developed. While crack 2 was developing, crack 1 increased in height by 10 mm and propagated 25 mm to the right, following the position of the embedded steel mesh in the top portion of the slab.

Loading was continued until crack 3 developed within the constant moment zone at a load of 31.1 kN. Crack 3 developed approximately 330 mm to the left of the right loading point, with an immediate height of 135 mm. A load resistance reduction of 6.2 kN (25.7% reduction) to 24.9 kN was observed instantaneously, generating a total deflection

of 18.40 mm. Although crack 2 showed negligible change, crack 1 continued to propagate horizontally as crack 3 developed.

Crack 4 developed, once the load resistance reached 32.6 kN, within the constant moment zone approximately 475 mm to the right of the left loading point with an immediate height of 125 mm. An instantaneous load resistance reduction to 25.1 kN (31.1% reduction) was observed, producing a total deflection of 25.40 mm. Negligible effects were observed in the previous three existing cracks while crack 4 developed.

At a load resistance of 33.1 kN, the development of a fifth crack, V1, was observed within the shear-flexural zone approximately 290 mm to the left of the left loading point with an immediate height of 130 mm. The load resistance reduced to 27.6 kN (22.8% reduction), bringing the total deflection to 32.05 mm. Crack 4 increased in height by 10 mm and propagated 30 mm to the left along the position of the embedded steel mesh while the fifth crack developed. The other previously existing cracks showed negligible change.

The load was applied again until a sixth crack, V2, developed in the shear-flexural zone, at a load resistance of 35.9 kN, approximately 100 mm to the right of the right loading point. An immediate crack height of 140 mm was observed along with a load resistance reduction to 31.5 kN (18.3% reduction), producing a total deflection of 39.98 mm. The previously existing cracks had negligible change as crack V2 developed.

Due to the excessive deflections, the load rate was increased to 1.2 mm/min. to speed up the testing, and loading was continued. At a load resistance of 42.1 kN, a seventh crack, crack 5, developed within the constant moment zone approximately 250 mm to the right of the left loading point with an immediate height of 125 mm. The load resistance reduced to 39.6 kN (9.5% reduction) instantly, giving a total deflection of 53.93 mm. Negligible effects were observed in the remaining existing cracks at this level of load.

Loading was continued until a load resistance of 44.6 kN was achieved, when the load rate was once again increased to 2.0 mm/min. to speed up the testing. The final two observed cracks, V3 and V4, both developed within the shear-flexural zones once the load reached 53.1 kN. The position of cracks V3 and V4 were 190 mm to the left of the left loading point and 330 mm to the right of the right loading point respectively, with immediate heights of 135 mm. The previously existing cracks all propagated along the position of the embedded steel mesh while the final two cracks were developing.

Once the loading was continued, excessive deflections occurred until the GFRP bars at the position of crack 1 ruptured at a load of 60.6 kN.

4.2.1.2 Slab I-150-B

Slab I-150-B consisted of a 1000 mm wide one-way slab with a thickness of 150 mm, producing a cross-sectional area of 150 000 mm^2. A cross-section of slab I-150-B is

illustrated in Figure 4.12(b), showing the placement of the reinforcements, which consisted of four 15.9 mm diameter ISOROD-GFRP bars in the longitudinal direction and 15 - 9.5 mm diameter ISOROD-GFRP bars in the transverse direction, fulfilling the requirements of the Canadian Design Code (CSA 1994). Slab I-150-B was originally designed to fail by rupturing of the GFRP bars and simultaneous crushing of the concrete according to the Canadian Design Code (CSA 1984). Due to limited sizes of ISOROD-GFRP bars and variable concrete strengths, it is impossible to accurately predict a balanced failure. The actual predicted failure mode is by rupturing of the GFRP bars just prior to crushing of the concrete.

Prior to the initiation of cracking, the slab exhibited linear behaviour as shown in Figure 4.5. The initial loading rate was set at 0.6 mm/min. Cracking was initiated at a load of 32.9 kN and a midspan deflection of 1.83 mm. All the cracks which developed during the testing of slab I-150-B are shown in Figures 4.13 and 4.15. The initial crack, crack 1, was observed within the constant moment zone approximately 60 mm inside the right loading point with an immediate height of 135 mm. Once the crack occurred, the load resistance immediately reduced to 16.6 kN (49.5% reduction).

The application of load was continued until crack 2 developed within the constant moment zone at a load of 34.7 kN. Development of the crack occurred approximately 225 mm inside the left loading point with an immediate height of 138 mm. The load resistance instantly reduced to 19.6 kN (45.9% reduction) and a total midspan deflection

of 10.66 mm developed. While crack 2 was developing, crack 1 propagated 5.00 mm vertically.

Once a load resistance of 40.6 kN was achieved, the loading rate was increased to 1.2 mm/min. to speed up testing. Loading was continued until a third crack developed within the constant moment zone at a load of 44.0 kN. Crack 3 developed approximately 495 mm to the right of left loading point with an immediate height of 132 mm. A load resistance reduction of 11.1 kN (33.7% reduction) to 32.9 kN was observed instantaneously, generating a total deflection of 30.33 mm. Crack 2 propagated 60 mm to the left and 25 mm to the right following the position of the embedded steel mesh, while crack 1 propagated 40 mm to the left during the development of crack 3.

Cracks V1 and V2 developed the second time the load reached 44.0 kN, outside the constant moment zone approximately 260 mm and 280 mm to the right of the right loading point respectively. The immediate height of cracks V1 and V2 were 110 mm and 138 respectively. Negligible effects were observed in the previous three existing cracks while cracks V1 and V2 developed.

At a load resistance of 49.7 kN, the development of a sixth crack, V3, was observed within the shear-flexural zone approximately 300 mm to the left of the left loading point with an immediate height of 140 mm. During the development of crack V3,

crack 3 and V2 increased in height by 15 mm and propagated 15 mm horizontally to the left, while cracks 1 and 2 displayed slight horizontal propagation.

Loading was continued until a seventh crack, crack 4, developed in the constant moment zone at a load resistance of 55.7 kN, approximately 435 mm to the right of the left loading point. The height of the crack immediately reached 130 mm, with the load resistance reducing to 50.0 kN (17.3% reduction), producing a total deflection of 64.27 mm. The sixth crack propagated approximately 25 mm to the left, while the previous five existing cracks had negligible change during the development of crack 4.

At this point during testing, due to the excessive deflections, the load rate was increased to 2.4 mm/min. At a load resistance of 65.2 kN, an eighth crack, V4, developed outside the constant moment zone approximately 85 mm to the left of the left loading point with an immediate height of 130 mm. Crack propagations along the position of the embedded steel mesh continued for all the previously existing cracks during the development of crack V4.

Loading was continued until a load resistance of 70.6 kN was achieved, when the load rate was once again increased to 6.0 mm/min. to speed up the testing. The final crack, V5, developed within the shear-flexural zone once the load reached 75.9 kN, approximately 370 mm to the left of the left loading point with an immediate height of 90

mm. The previously existing cracks all propagated along the position of the embedded steel mesh while the final crack was developing.

Once the loading was continued, excessive deflections occurred until the GFRP bars at the position of crack 2 ruptured in tension at a load resistance of 80.4 kN.

4.2.1.3 Slab I-150-C

Slab I-150-C consisted of a 1000 mm wide one-way slab with a thickness of 150 mm, producing a cross-sectional area of 150 000 mm^2. A cross-section of slab I-150-C is illustrated in Figure 4.12(c), showing the placement of the reinforcements, which consisted of five 15.9 mm diameter ISOROD-GFRP bars in the longitudinal direction and 15 - 9.5 mm diameter ISOROD-GFRP bars in the transverse direction, fulfilling the requirements of the Canadian Design Code (CSA 1994). Slab I-150-C was originally designed to fail by crushing of the concrete prior to rupturing of the GFRP bars according to the Canadian Design Code (CSA 1984).

The initial stiffness of slab I-150-C, referring to the load-deflection behaviour in Figure 4.6, was less than the previously tested 150 mm slabs reinforced with GFRP bars, due to a crack which developed during a load cell malfunction. Unfortunately, due to this malfunction the actual load resistance when the initiation of cracking occurred is unknown. Once the malfunction was corrected, testing resumed with an initial loading rate of 0.6 mm/min.. Initiation of further cracking occurred at a load of 27.0 kN and a

midspan deflection of 3.30 mm. For all analysis purposes, this was the load taken as the cracking load. All the cracks that developed in slab I-150-C are shown in Figures 4.13 and 4.16. The initial crack, crack 1, was observed within the constant moment zone approximately 240 mm inside the right loading point with a height of 135 mm. Crack 2 was observed 615 mm to the left of the right loading point developing a height of 110 mm. Once the second crack occurred, the load resistance immediately reduced to 17.1 kN (36.7% reduction).

The application of load was continued until crack 3 developed within the constant moment zone at a load resistance of 28.5 kN. The crack developed approximately 370 mm inside the right loading point with an immediate height of 130 mm. Load resistance instantly reduced to 21.4 kN (26.3% reduction) and a total midspan deflection of 11.60 mm developed. While crack 3 was developing, cracks 1 and 2 showed negligible change.

Loading was continued until crack 4 developed within the constant moment zone, at a load resistance of 35.4 kN, approximately 75 mm to the left of right loading point. As crack 4 propagated from side A to side B, referring to the bottom view of the slab in Figure 4.17, it connected with crack 1. The immediate height of the crack was 115 mm straight vertical. A reduction in load resistance of 1.7 kN (6.3% reduction) to 33.7 kN was observed instantaneously, generating a total deflection of 24.36 mm. Although crack 1 showed negligible change, cracks 2 and 3 increased in height by 30 mm and 10 mm as crack 4 developed.

Once the load resistance reached 38.4 kN, the development of a fifth crack, V1, was observed within the shear-flexural zone approximately 75 mm to the left of the left loading point with an immediate height of 140 mm. The load resistance reduced to 37.7 kN (2.6% reduction), bringing the total deflection to 27.77 mm. The previously existing cracks showed negligible change.

Once the load resistance of 40.6 kN was achieved, the load rate was increased to 1.2 mm/min.. A sixth crack, V2, developed in the shear-flexural zone at a load of 48.5 kN, approximately 300 mm to the right of the right loading point with a height of 140 mm. The load resistance instantly reduced to 44.9 kN (13.3% reduction), producing a total deflection of 51.74 mm. The previously existing cracks all branched into two cracks and propagated along the position of the embedded steel mesh.

At a load resistance of 67.7 kN, crack 6 developed within the constant moment zone approximately 85 mm to the right of the left loading point with an immediate height of 120 mm. Referring to Figure 4.17, crack 6 developed as a result of crack 2 branching into two cracks as it propagated from side B to side A. Only a slight reduction in load resistance of 0.1% to 66.6 kN was observed, producing a total deflection of 87.36 mm. During the development of crack 6, negligible effects were observed in crack 4, while cracks V2, 2 and 5 all propagated 10 mm to the left and crack 1 propagated 25 mm to the right.

Loading was continued until a load resistance of 70.6 kN was observed, when the load rate was once again increased to 2.0 mm/min. to speed up the testing. Once loading was continued, excessive deflections occurred until the GFRP bars at the position of crack V1 ruptured in shear at a load of 74.6 kN.

4.2.1.4 Slab S-150-T

Slab S-150-T consisted of a 1000 mm wide one-way slab with a thickness of 150 mm, producing a cross-sectional area of 150 000 mm^2. A cross-section of slab S-150-T is illustrated in Figure 4.12(d), showing the placement of the reinforcements, which consisted of five No. 15 steel rebars in the longitudinal direction and 15 - No. 10 steel rebars in the transverse direction, fulfilling the requirements of the Canadian Design Code (CSA 1994). Slab S-150-T was originally designed to fail by yielding of the steel rebars prior to crushing of the concrete according to the Canadian Design Code (CSA 1984).

Prior to the initiation of cracking, the slab exhibited linear behaviour as shown in Figure 4.7, with an initial loading rate of 0.6 mm/min.. Initiation of cracking occurred at a load resistance of 40.6 kN and a midspan deflection of 2.74 mm. All the cracks that developed in slab S-150-T are shown in Figures 4.13 and 4.18. The initial crack, crack 1, was observed within the constant moment zone approximately 210 mm inside the left

loading point with an immediate height of 75 mm. Once the crack occurred, the load resistance immediately reduced to 40.1 kN (1.2% reduction).

The application of load was continued until cracks 2 to 6 developed within the constant moment zone at a load resistance of 45.6 kN. The cracks developed 545 mm, 45 mm, 225 mm, 390 mm and 915 mm to the left of the right loading point, with heights of 50 mm, 80 mm, 90 mm, 90 mm and 85 mm for cracks 2 to 6 respectively. Crack V1 also developed outside the constant moment zone once the load resistance reached 45.6 kN. The position of crack V1 was approximately 60 mm to the left of the left loading point, and the immediate height of the crack was 100 mm. The load resistance reduced to 43.6 kN (4.9% reduction) and a total midspan deflection of 5.71 mm developed. While these cracks were developing, crack 1 increased in height by 20 mm.

Loading was continued until cracks 7 and 8 developed within the constant moment zone and crack V2 developed outside the constant moment zone at a load resistance of 50.6 kN. Crack 7 developed approximately 200 mm to the left of right loading point with respect to side A of the slab. Referring to Figure 4.19, the bottom view of slab S-150-T, crack 7 is actually an extension of crack 4 as it propagated from side A to side B. Crack 4 also split into two cracks and connected up with crack 5. Crack 8 developed as an extension of cracks 2 and 5 as they propagated from side A to side B near the center of the slab. Crack V2 developed approximately 160 mm to the right of the right loading point. The immediate crack heights were 90 mm, 85 mm and 105 mm for cracks 7, 8 and

V2 respectively. A load resistance reduction of 4.0 kN (9.9% reduced) to 46.6 kN was observed instantaneously, generating a total deflection of 8.47 mm. Although crack 3 showed negligible change, cracks 1 and 2 increased in height by 10 mm and 20 mm respectively while cracks 7, 8 and V2 developed.

Cracks V3 and V4 developed after the continuation of loading, and a load resistance of 55.6 kN was achieved, outside the constant moment zone approximately 280 mm to the left of the left loading point and 290 mm to the right of the right loading point respectively. The immediate height cracks V3 and V4 were 80 mm and 50 mm respectively. The load resistance instantly reduced to 52.6 kN (7.4% reduced), producing a total deflection of 10.51 mm. Increase in heights by 10 mm, 20 mm and 20 mm were observed in cracks 1, 2 and 6 respectively, while cracks V3 and V4 developed.

At a load resistance of 75.6 kN, the development of cracks V5 and V6 was observed within the shear-flexural zone approximately 495 mm to the right of the right loading point with immediate heights of 110 mm and 100 mm respectively. The load resistance reduced to 74.6 kN (2.5% reduction), bringing the total deflection to 17.39 mm. Cracks 5, 7, 8 and V1 all increased in height by 20 mm while the cracks developed. The other previously existing cracks showed negligible change.

The load was applied again until crack V7 developed in the shear-flexural zone at a load resistance of 90.6 kN, approximately 535 mm to the right of the right loading point.

The height of the crack immediately reached 60 mm straight vertical and the load resistance instantly reduced to 88.6 kN (4.9% reduction), producing a total deflection of 22.15 mm. The previously existing cracks all increased in height of varying degrees, ranging between 10 mm and 20 mm.

Due to the excessive deflections, the load rate was increased to 1.2 mm/min. to speed up the testing, and the loading was continued. At a load resistance of 95.6 kN, crack 2 split into two cracks and cracks V8 and V9 developed outside the constant moment zone approximately 160 mm to the left of the left loading point and 70 mm to the right of the right loading point respectively. The immediate height of cracks V8 and V9 were 165 mm and 190 mm respectively. The load resistance reduced to 94.6 kN (2.5% reduction), giving a total deflection of 23.98 mm. Negligible effects were observed in the remaining existing cracks during the development of cracks V8 and V9.

Loading was continued until a load resistance of 120.6 kN was observed, when the load rate was once again increased to 2.4 mm/min. to speed up the testing. Crack V10 developed within the shear-flexural zone once the load resistance reached 125.6 kN, approximately 575 mm to the left of the left loading point with an immediate height of 65 mm. The previously existing cracks all propagated along the position of the embedded steel mesh while crack V10 was developing.

The final two cracks, V11 and V12, both developed outside the constant moment zone at load resistances of 130.6 kN and 140.6 kN respectively. The positions of cracks V11 and V12 were 30 mm to the left of the left loading point and 450 mm to the right of the right loading point, with heights of 130 mm and 100 mm respectively.

Once the loading was continued, excessive deflections occurred until the concrete above the position of crack 1 crushed within the compression zone at a load resistance of 155.0 kN.

4.2.1.5 Slab I-200-A

Slab I-200-A consisted of a 1000 mm wide one-way slab with a thickness of 200 mm, producing a cross-sectional area of 200 000 mm^2. A cross-section of slab I-200-A is illustrated in Figure 4.12(e), showing the placement of the reinforcements, which consisted of five 9.5 mm diameter ISOROD-GFRP bars in the longitudinal direction and 22 - 9.5 mm diameter ISOROD-GFRP bars in the transverse direction, fulfilling the requirements of the Canadian Design Code (CSA 1994). Slab I-200-A was originally designed to fail by rupturing of the GFRP bars prior to crushing of the concrete according to the Canadian Design Code (CSA 1984).

Prior to the initiation of cracking, the slab exhibited linear behaviour as shown in Figure 4.8, with an initial loading rate of 0.6 mm/min.. Initiation of cracking occurred at a load resistance of 43.9 kN and a midspan deflection of 1.37 mm. All the cracks that

developed in slab I-200-A are shown in Figures 4.20 and 4.21. The initial crack, crack 1, was observed within the constant moment zone approximately 90 mm inside the left loading point with an immediate height of 125 mm. Once the crack occurred, the load resistance immediately reduced to 22.0 kN (49.9% reduction).

The application of load was continued until crack 2 developed within the constant moment zone once the load resistance reached 40.9 kN for the second time. The crack occurred approximately 380 mm inside the right loading point with an immediate height of 180 mm. The load resistance instantly reduced to 28.6 kN (28.0% reduction) and a total midspan deflection of 10.59 mm developed. While crack 2 was developing, crack 1 increased in height by 55 mm.

Loading was continued until crack 3 developed within the constant moment zone at a load resistance of 44.4 kN, approximately 120 mm to the left of right loading point with an immediate height of 170 mm. A reduction in load resistance of 13.8 kN (31.4% reduction) to 30.6 kN was observed instantaneously, generating a total deflection of 17.02 mm. Cracks 1 and 2 showed negligible changes while crack 3 developed.

Crack 4 developed once the load resistance reached 38.7 kN for the third time. The fourth crack developed within the constant moment zone approximately 250 mm to the right of the left loading point with an immediate height of 185 mm. The load resistance instantly reduced to 32.2 kN (14.8% reduction), producing a total deflection of

20.31 mm. Negligible effects were observed in the previous three existing cracks while crack 4 developed.

Once the loading was continued, excessive deflections occurred until the GFRP bars at the position of crack 2 ruptured in tension at a load of 47.1 kN.

4.2.1.6 Slab I-200-C

Slab I-200-C consisted of a 1000 mm wide one-way slab with a thickness of 200 mm, producing a cross-sectional area of 200 000 mm^2. A cross-section of slab I-200-C is illustrated in Figure 4.12(f), showing the placement of the reinforcements, which consisted of six 15.9 mm diameter ISOROD-GFRP bars in the longitudinal direction and 22 - 9.5 mm diameter ISOROD-GFRP bars in the transverse direction, fulfilling the requirements of the Canadian Design Code (CSA 1994). Slab I-200-C was originally designed to fail by crushing of the concrete prior to rupturing of the GFRP bars according to the Canadian Design Code (CSA 1984).

Prior to the initiation of cracking, the slab exhibited linear behaviour as shown in Figure 4.9, with an initial loading rate of 0.6 mm/min.. Initiation of cracking occurred at a load resistance of 44.0 kN and a midspan deflection of 1.23 mm. All the cracks that developed in slab I-200-C are shown in Figures 4.20 and 4.22. The initial crack, crack 1, was observed within the constant moment zone approximately 360 mm inside the right

loading point with an immediate height of 165 mm. Once the crack occurred, the load resistance immediately reduced to 27.6 kN (37.3% reduction).

The application of load was continued until crack 2 developed within the constant moment zone at a load resistance of 47.4 kN, approximately 260 mm inside the left loading point with an immediate height of 175 mm. The load resistance instantly reduced to 30.4 kN (38.6% reduction) and a total midspan deflection of 6.01 mm developed. While crack 2 was developing, crack 1 branched into two cracks 10 mm apart, starting at the bottom of the slab and ending at the approximate height of the original branch of 165 mm.

Loading was continued until crack 3 developed within the constant moment zone at a load resistance of 52.4 kN, approximately 50 mm to the left of right loading point with an immediate height of 175 mm. A reduction in load resistance of 14.0 kN (31.8% reduction) to 38.4 kN was observed instantaneously, generating a total deflection of 10.00 mm. Although crack 2 showed negligible change, crack 1 propagated vertically 15 mm during the development of crack 3.

Crack 4 developed upon the continuation of loading, at a load resistance of 57.9 kN, within the constant moment zone directly under the left loading point with an immediate height of 170 mm. The load resistance instantly reduced to 46.4 kN (26.1% reduction), producing a total deflection of 14.29 mm. Cracks 2 and 3 increased in height

by 10 mm and 15 mm respectively while crack 4 was developing, and negligible effects were observed in crack 1.

At a load resistance of 63.9 kN, the development of a fifth crack, V1, was observed within the shear-flexural zone approximately 180 mm to the right of the right loading point with an immediate height of 170 mm. The load resistance reduced to 60.5 kN (8.2% reduction), bringing the total deflection to 19.04 mm. Crack 4 increased in height by 15 mm while the remaining existing cracks show negligible change while the fifth crack developed.

Loading was applied again until a sixth crack, V2, developed in the shear-flexural zone at a load resistance of 68.2 kN, approximately 290 mm to the left of the left loading point. The height of the crack immediately reached 170 mm while the load resistance reduced to 61.7 kN (14.8% reduction), producing a total deflection of 23.40 mm. The previously existing cracks showed negligible change while crack V2 developed.

At a load resistance of 74.1 kN, due to the excessive deflections, the load rate was increased to 1.2 mm/min. to speed up the testing, and the loading was continued. At a load resistance of 88.1 kN, the seventh crack, crack 5, developed within the constant moment zone approximately 470 mm to the right of the left loading point with an immediate height of 150 mm. The load resistance reduced to 81.2 kN (15.7% reduction) instantly, creating a total deflection of 34.45 mm.

All the cracks continued to propagate left and right along the position of the embedded steel mesh as the loading was continued. As the load resistance reached 158.1 kN, excessive shear deformations occurred at the position of crack V2 and the GFRP bars ruptured in shear.

4.2.1.7 Slab S-200-T

Slab S-200-T consisted of a 1000 mm wide one-way slab with a thickness of 200 mm, producing a cross-sectional area of 200 000 mm^2. A cross-section of slab S-200-T is illustrated in Figure 4.12(g), showing the placement of the reinforcements, which consisted of six No. 10 steel rebars in the longitudinal direction and 22 - No. 10 steel rebars in the transverse direction, fulfilling the requirements of the Canadian Design Code (CSA 1994). Slab S-200-T was originally designed to fail by yielding of the steel rebars prior to crushing of the concrete according to the Canadian Design Code (CSA 1984).

Prior to the initiation of cracking, the slab exhibited linear behaviour as shown in Figure 4.10, with an initial loading rate of 0.6 mm/min.. Initiation of cracking occurred at a load resistance of 79.0 kN and a midspan deflection of 4.42 mm. All the cracks that developed in slab S-200-T are shown in Figures 4.20 and 4.23. The initial cracks, cracks 1 to 4, were observed within the constant moment zone approximately 125 mm, 590 mm, 380 mm and 800 mm to the left of the right loading point, with immediate heights of 150

mm, 130 mm, 145 mm and 140 mm respectively. Once the cracks occurred, the load resistance immediately reduced to 74.5 kN (5.7% reduction).

The application of load was continued until a crack, V1, developed within the shear-flexural zone at a load resistance of 88.7 kN, approximately 80 mm to the right of the right loading point with an immediate height of 145 mm. The load resistance instantly reduced to 81.1 kN (9.6% reduction) and a total midspan deflection of 6.62 mm developed. While crack V1 was developing, cracks 1 to 4 showed negligible change.

Loading was continued until crack V2 developed outside the constant moment zone at a load resistance of 92.1 kN, approximately 65 mm to the right of right loading point with an immediate height of 155 mm. A reduction in load resistance of 7.0 kN (8.9% drop) to 85.1 kN was observed instantaneously, generating a total deflection of 7.89 mm. All of the previously existing cracks showed an average increase in height of approximately 20 mm.

Cracks 5 and 6 developed, upon achieving the yield load resistance of 101.6 kN, within the constant moment zone approximately 640 mm and 260 mm to the left of the right loading point respectively. The immediate height of both cracks was 140 mm. The load resistance instantly reduced to 97.1 kN (5.6% reduction), producing a total deflection of 11.01 mm. At the same load resistance, a crack in the shear-flexural zone, V3, was also observed, approximately 335 mm to the right of the right loading point, attaining a height

of 135 mm. Negligible effects were observed in the previously existing cracks while cracks 5, 6 and V3 developed.

The load rate was increased to 1.2 mm/min. once the load resistance reached 104.1 kN. At a load resistance of 113.4 kN, the development of a tenth crack, V4, was observed within the shear-flexural zone approximately 310 mm to the left of the left loading point, with an immediate height of 125 mm. The load resistance reduced to 107.2 kN (7.8% reduction), bringing the total deflection to 29.60 mm. While crack V4 was developing, the previously existing cracks increased in height by an average of 20 mm with cracks 1, 3 and 4 branching into two cracks and propagating towards the closest loading points with respect to each individual crack.

Once again the load rate was increased to 2.4 mm/min. to speed up testing. Loading was continued until cracks 7, 8 and 9 developed in the constant moment zone, at a load resistance of 125.7 kN, approximately 580 mm, 55 mm and 965 mm to the right of the left loading point respectively. The height of cracks 7 to 9 immediately reached 175 mm, 160 mm and 100 mm and the load resistance instantly reduced to 120.9 kN (6.1% reduction), producing a total deflection of 54.60 mm. Crack 7 was observed only on side A of the slab. As it propagated to side B, along the bottom of the slab, it connected with crack 2, as shown in Figure 4.24. Crack V4 increased in height by 35 mm while the remaining existing cracks showed negligible change as cracks 7 to 9 developed.

Due to the excessive deflections, the load rate was increased to 3.0 mm/min. to speed up the testing, and the loading was continued. At a load resistance of 144.0 kN, crack V5 developed within the shear-flexural zone approximately 460 mm to the right of the right loading point with an immediate height of 140 mm. The load resistance reduced to 139.0 kN (6.3% reduction) instantly, creating a total deflection of 116.4 mm. The four previously existing flexural-shear cracks propagated an average of 40 mm towards their respective loading points, while the remaining flexural cracks within the constant moment zone propagated an average 40 mm vertically during the development of crack V5.

The final crack, V6, developed within the shear-flexural zones once the load resistance reached 152.2 kN. The position of the crack was approximately 490 mm to the left of the left loading point with an immediate height of 140 mm. The previously existing cracks all propagated along the position of the embedded steel mesh while the final crack was developing.

Once the loading reached 155.9 kN, excessive deflections occurred until the concrete in the compression zone above the position of cracks 1 and 6 crushed.

4.2.1.8 Slab LL-200-C

Slab LL-200-C consisted of a 1000 mm wide one-way slab with a thickness of 200 mm, producing a cross-sectional area of 200 000 mm^2. A cross-section of slab LL-200-C is illustrated in Figure 4.12(h), showing the placement of the reinforcements, which consisted of six 8.0 mm diameter Leadline-CFRP rods in the longitudinal direction and 33 - 8.0 mm diameter Leadline-CFRP rods in the transverse direction, fulfilling the requirements of the Canadian Design Code (CSA 1994). Slab LL-200-C was originally designed to fail by crushing of the concrete prior to rupturing of the CFRP rods according to the Canadian Design Code (CSA 1984).

Prior to the initiation of cracking, the slab exhibited linear behaviour as shown in Figure 4.11, with an initial loading rate of 0.6 mm/min.. Initiation of cracking occurred at a load resistance of 51.0 kN and a midspan deflection of 3.53 mm. All the cracks that developed in slab LL-200-C are shown in Figures 4.20 and 4.25. The initial crack, crack 1, was observed within the constant moment zone approximately 60 mm inside the right loading point with an immediate height of 160 mm. Once the crack occurred, the load resistance immediately reduced to 41.1 kN (19.4% reduction).

The application of load was continued until crack 2 developed within the constant moment zone, at a load resistance of 53.6 kN, approximately 430 mm inside the right loading point with an immediate height of 180 mm. The load resistance instantly reduced

to 44.5 kN (17.8% reduction) and a total midspan deflection of 8.48 mm developed. While crack 2 was developing, crack 1 showed no change in height.

Loading was continued until crack 3 developed within the constant moment zone, the second time the load resistance reached 53.2 kN, approximately 200 mm to the right of left loading point with an immediate height of 175 mm. A reduction in load resistance of 7.1 kN (13.9% reduction) to 46.1 kN was observed instantaneously, generating a total deflection of 10.66 mm. Cracks 1 and 2 both propagated vertically approximately 10 mm while crack 3 was developing.

Crack 4 developed upon the continuation of loading, at a load of 54.6 kN, within the constant moment zone directly under the left loading point with an immediate height of 155 mm. The load resistance instantly reduced to 52.2 kN (4.7% reduction), producing a total deflection of 12.11 mm. Negligible effects were observed in the previously existing cracks while crack 4 developed.

The load rate was increased to 1.2 mm/min. once the load resistance reached 55.1 kN. At a load resistance of 58.6 kN, the development of crack 5 was observed within the constant moment zone approximately 370 mm to the right of the left loading point with an immediate height of 170 mm. The load resistance reduced to 55.4 kN (6.3% reduction), bringing the total deflection to 14.14 mm. The previously existing cracks showed negligible change while crack 5 developed.

The load was applied again until a sixth crack, V1, developed in the shear-flexural zone, at a load resistance of 65.5 kN, approximately 290 mm to the right of the right loading point with a height of 170 mm. An instantaneous reduction in load resistance of 63.2 kN (4.5% reduction) was observed, producing a total deflection of 18.10 mm. The previously existing cracks showed negligible change during the development of crack V1.

At a load resistance of 74.6 kN, a seventh crack, V2, developed outside the constant moment zone approximately 220 mm to the left of the left loading point with an immediate height of 95 mm. The load resistance reduced to 71.2 kN (6.7% reduction) instantly, creating a total deflection of 22.16 mm. Negligible effects were observed in the remaining existing cracks.

Crack V3 developed within the shear-flexural zones once, the load resistance reached 92.6 kN, approximately 500 mm to the left of the left loading point with a height of 175 mm.

The final crack developed, at a load resistance of 147.6 kN, outside the constant moment zone approximately 500 mm to the right of the right loading point with a height of 175 mm. All the previously existing cracks propagated excessively in the horizontal direction while the final crack developed.

Once the loading reached 259.1 kN, the slab failed as all six rods slipped with respect to the left end of the slab. Just prior to the failure load, bond cracks were observed on the bottom of the slab along the position of three of the six rods. Once the failure occurred, bond cracks were observed along the bottom of the slab at the position of all six rods starting at crack 4 and continuing to the left end of the slab.

4.2.2 Crack Widths

The crack widths of the cracks developed within the constant moment zone of all eight slabs were measured and recorded, and are shown in Figure 4.26 to 4.31, with the exception of slabs I-150-B and I-200-A. These slabs developed crack widths equal to or greater than 1.0 mm immediately after the initiation of the first cracks.

4.2.3 Strains

4.2.3.1 Strains at Top of Slabs

The compressive strains in the outer most compression fibres of the concrete slabs, top of the slabs, within the flexural zone was recorded during testing through the use of manual DEMEC point readings. The load-compression strain behaviour is presented, with the average values of the three zones of DEMEC point stations along the top of the slabs, (refer to Figures 3.9 for DEMEC point stations and zones) and are presented in Figures 4.32 to 4.39.

4.2.3.2 Strains at Level of Reinforcements

The load-tensile strain behaviour at the reinforcement level of all eight slabs was recorded using electrical resistant strain gauges, with the exception of specimens S-150-T and S-200-T, which were attached directly to the ISOROD-GFRP bars and Leadline-CFRP rods, and by manual DEMEC point readings within the flexural zone of the slabs (refer to Figure 3.7 and Figure 3.8 for Strain Gauge positions and DEMEC point stations). The average load-tensile strain behaviour at the level of reinforcement using this data is presented in Figures 4.40 to 4.47. All individual data including all DEMEC point readings and strain gauge readings are presented in a technical report prepared at the University of Manitoba (Michaluk 1995).

4.2.4 Bond Slippage of Reinforcements

The lone slab which displayed any slippage during the testing was slab LL-200-C. The Leadline reinforcement slipped considerably, over 100 mm, at the left end of the slab with respect to side A, as the ultimate load resistance of 259.1 kN was achieved. At the ultimate load, bond cracks were observed at the bottom of the slab at all six Leadline CFRP rod positions, beginning at the extreme left end of the slab and ending at the position of crack 4 (1250 mm in total length). The load resistance immediately reduced to approximately 40 kN. The observed bond failure cracks and slippage of the CFRP rods are shown in Figures 4.48 and 4.49.

4.2.5 Failure Modes

The predicted and observed ultimate loads and failure modes for all eight slabs are presented in Table 4.4. Figures 4.50 to 4.57 present all eight slabs in their final positions after achieving their respective failure loads.

Table 4.1: Concrete properties for all eight slabs.

Cast No.	Specimens Mark No.	f'_c [MPa]	f_R [MPa]	E_c [MPa]	ε'_c [%]
1	S-150-T S-200-T	60.0	7.2	32340	-------
2	I-150-C I-200-C	66.0	6.23	36547	0.236
3	I-150-A I-200-A	63.9	4.73	35177	0.252
4	I-150-B LL-200-C	66.3	6.66	38526	0.259

Table 4.2: Tensile properties of ISOROD GFRP bars.

Test by:	Tensile Stress [MPa]		Ultimate Strain [%]		Elastic Modulus [MPa]	
	Average Values	Standard Deviation	Average Values	Standard Deviation	Average Values	Standard Deviation
Chaallal and Benmokrane (1993)	692	19.4	1.767	.047	41333	1247
Grieef (1996)	696	33.4	1.542	.087	45250	240
Michaluk (1996)	599.2	21.5	1.414	.050	42166	876

Table 4.3: Tensile properties of Leadline CFRP rods (Abdelrahman 1995).

Anchorage Type	Ultimate Stress MPa		Ultimate Force kN		Ultimate Strain %		Elastic Modulus GPa	
	Average Value	σ_n*	Average Value	σ_n*	Average Value	σ_n*	Average Value	σ_n*
Concrete Block	2950	24.3	139.5	1.17	1.56	0.04	187	6.1
Wedge type, reported by the manufac. company	1970 (guaranteed) 2250 (maximum)		93.2 (guaranteed) 106.4 (maximum)		1.3 1.3		147 147	
wedge type, tested at U. of M.	2280	223	107.8	10.5	1.29	0.12	177	3.3

σ_n* denotes standard deviation

Table 4.4: Summary of test results.

Slab	P_{cr} kN	$\Delta P/P_{cr}$ %	Predicted Ultimate Load kN	Ultimate Load P_{ult} kN	Ultimate Deflection Δ_{ult} mm	Predicted Failure Mode	Observed Failure Mode
S-150-T	40.6	8.1	107.2*	109.6*	29.0*	Yield of Rebars	Yield of Rebars
I-150-A	24.1	49.4	73.6	60.6	103.6	Rupture of Reinf.	Rupture of Reinf.
I-150-B	32.9	49.5	109.5	80.4	125.7	Balanced	Rupture of Reinf.
I-150-C	27.0	36.7	135.9	74.6	101.1	Concrete Crushing	Shear
S-200-T	79.0	9.1	111.7*	101.6*	10.3*	Yield of Rebars	Yield of Rebars
I-200-A	43.9	49.9	77.5	47.1	28.3	Rupture of Reinf.	Rupture of Reinf.
I-200-C	44.0	34.3	246.5	158.1	80.8	Concrete Crushing	Shear
LL-200-C	51.0	19.4	202.8	259.1	118.8	Concrete Crushing	Bond

* Values at yielding.

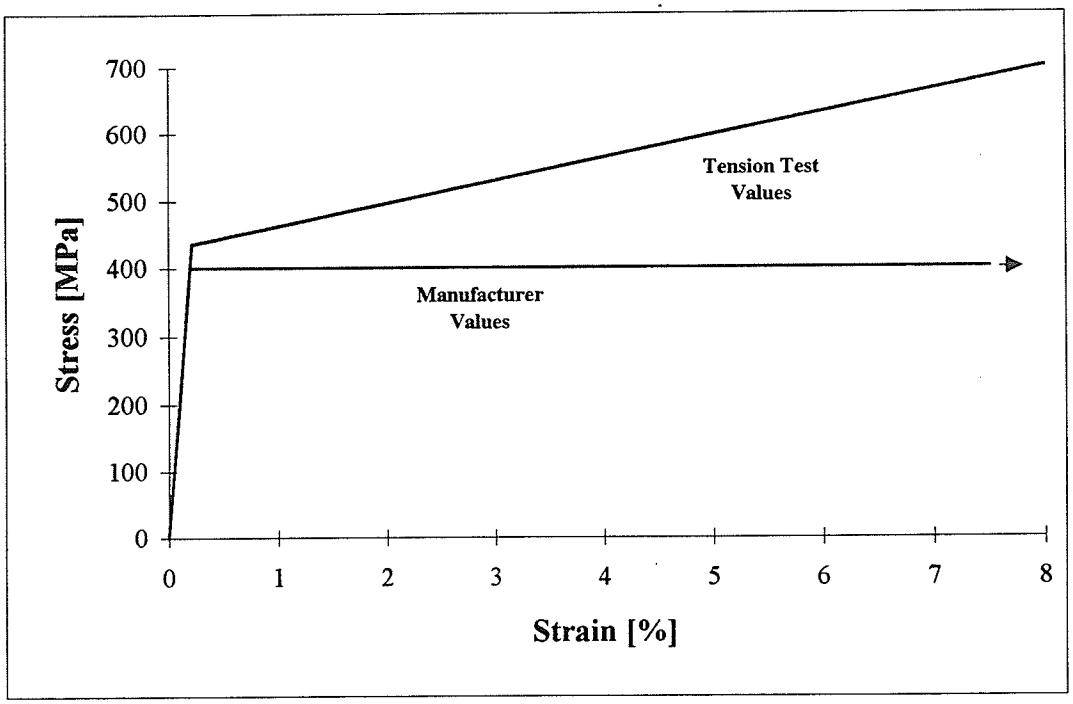

Figure 4.1: Tensile stress-strain behaviour of steel rebars.

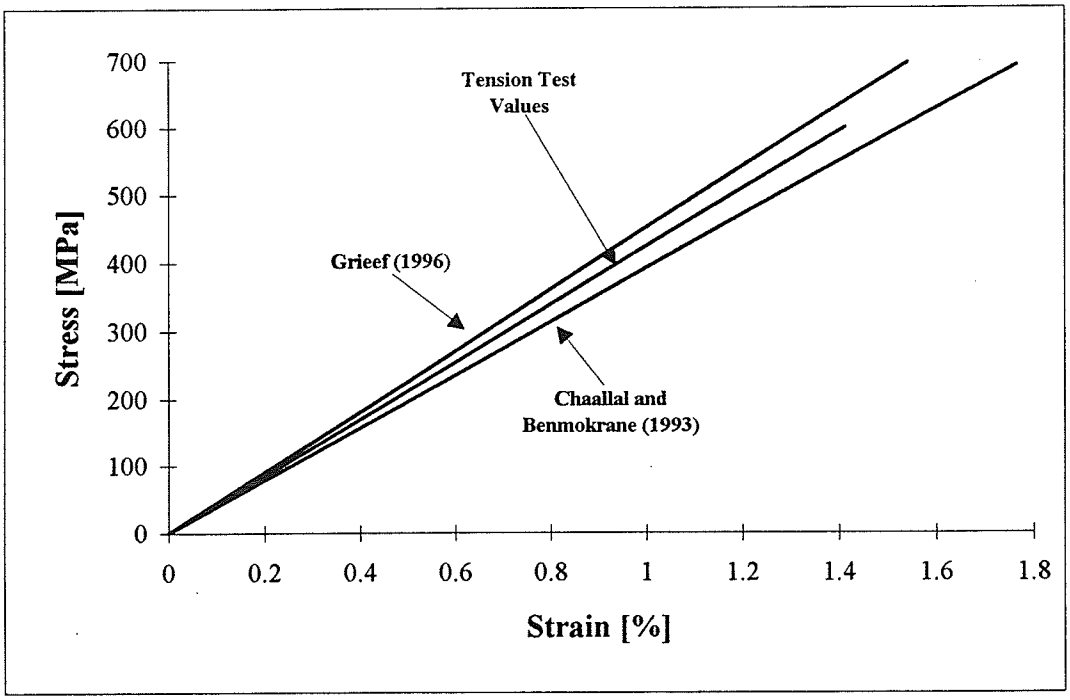

Figure 4.2: Tensile stress-strain behaviour of ISOROD-GFRP bars.

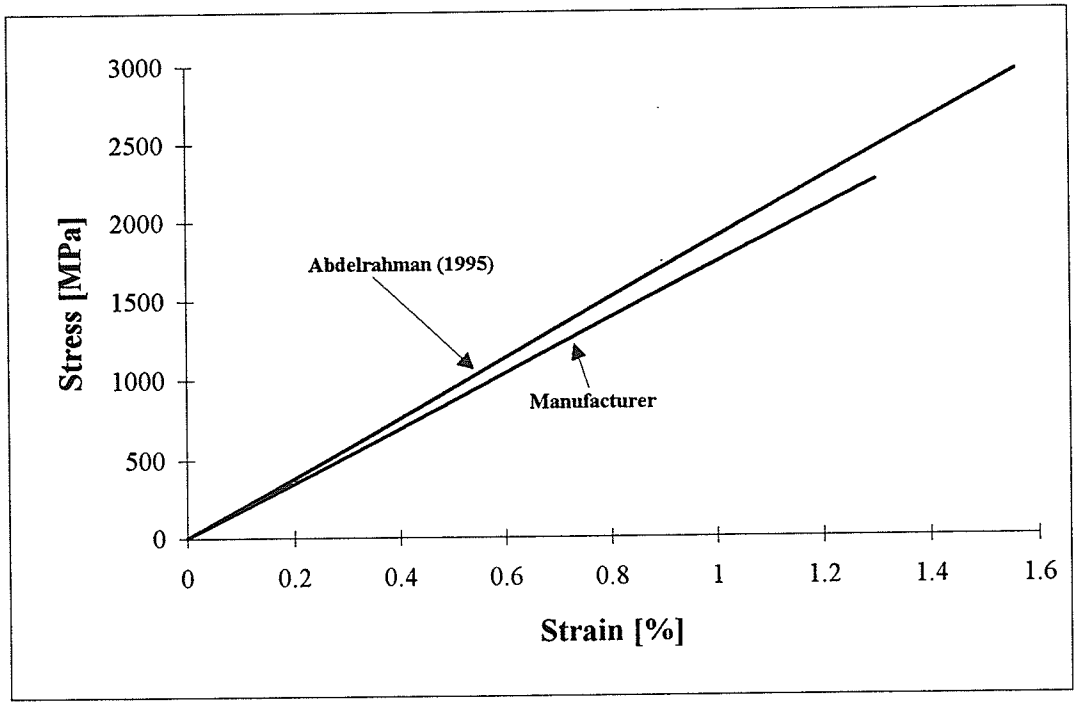

Figure 4.3: Tensile stress-strain behaviour of Leadline-CFRP rods.

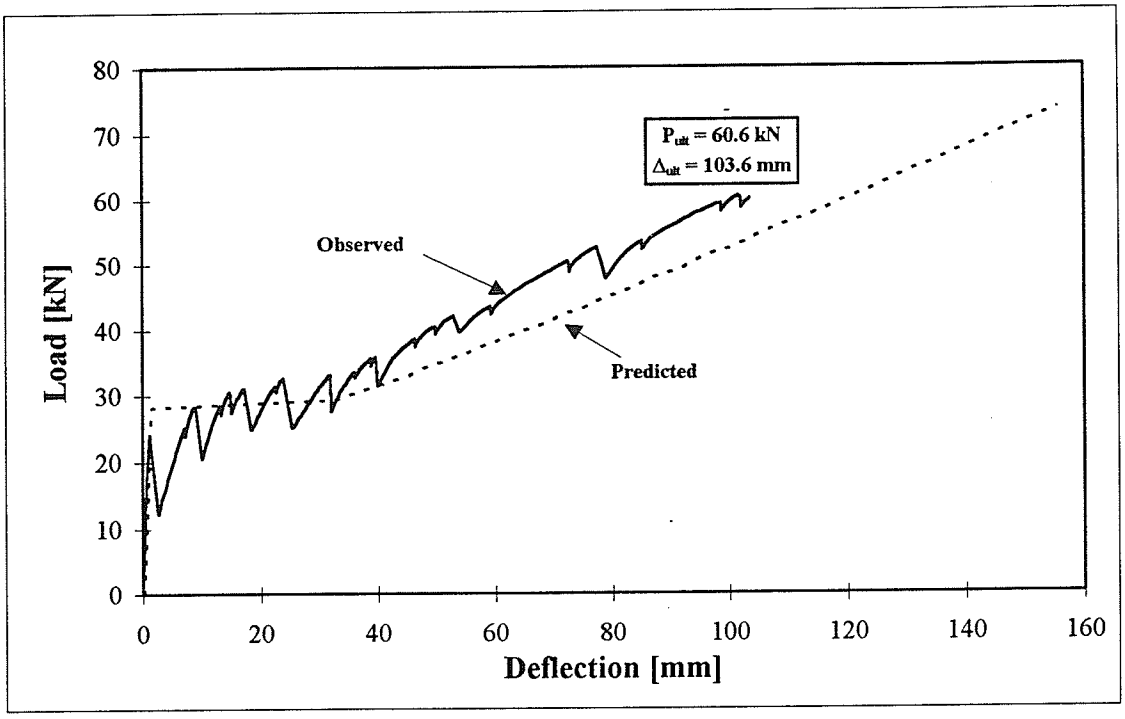

Figure 4.4: Predicted and observed midspan load-deflection diagram for slab I-150-A.

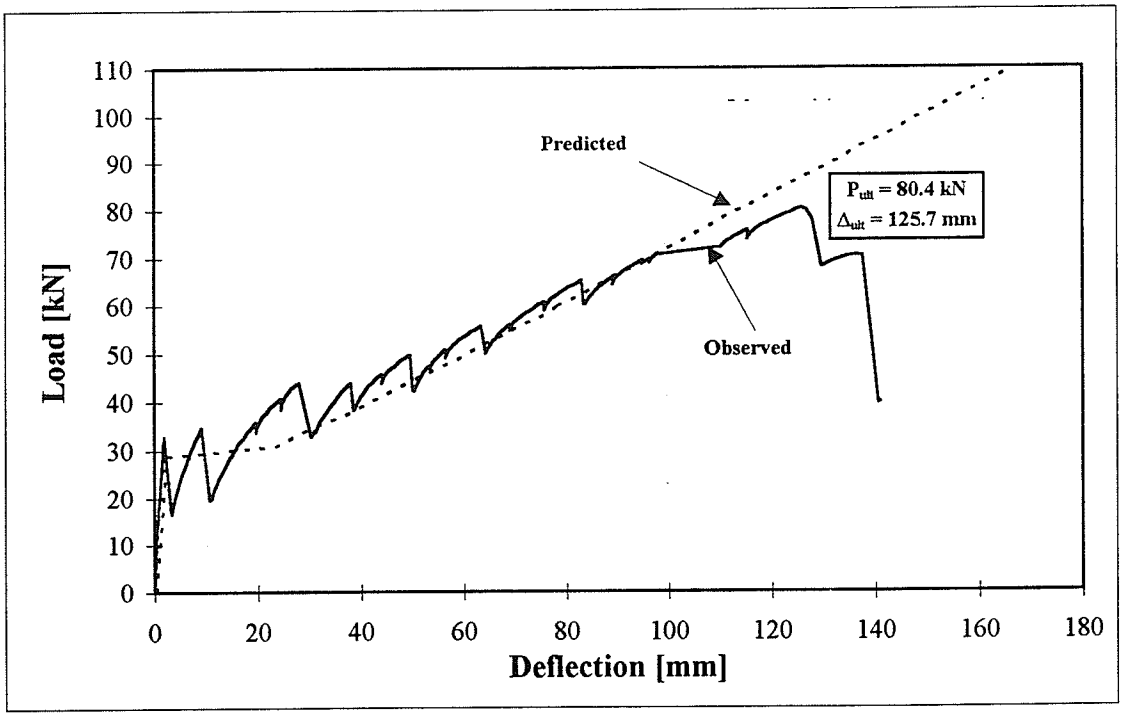

Figure 4.5: Predicted and observed midspan load-deflection diagram for slab I-150-B.

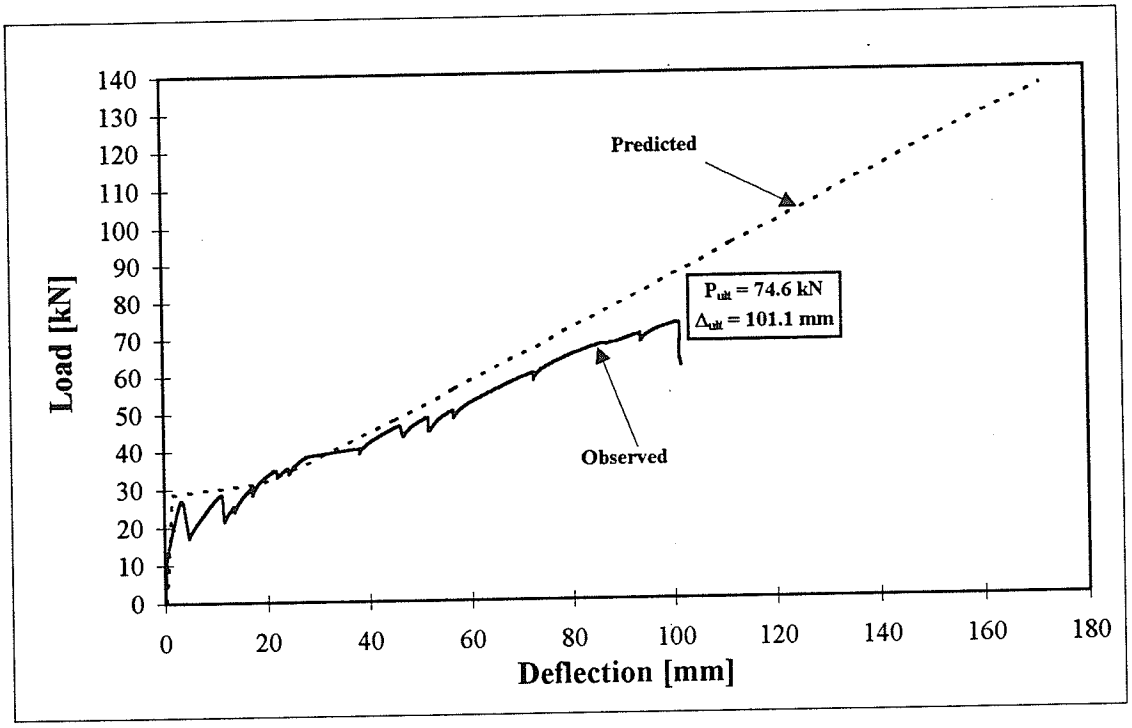

Figure 4.6: Predicted and observed midspan load-deflection diagram for slab I-150-C.

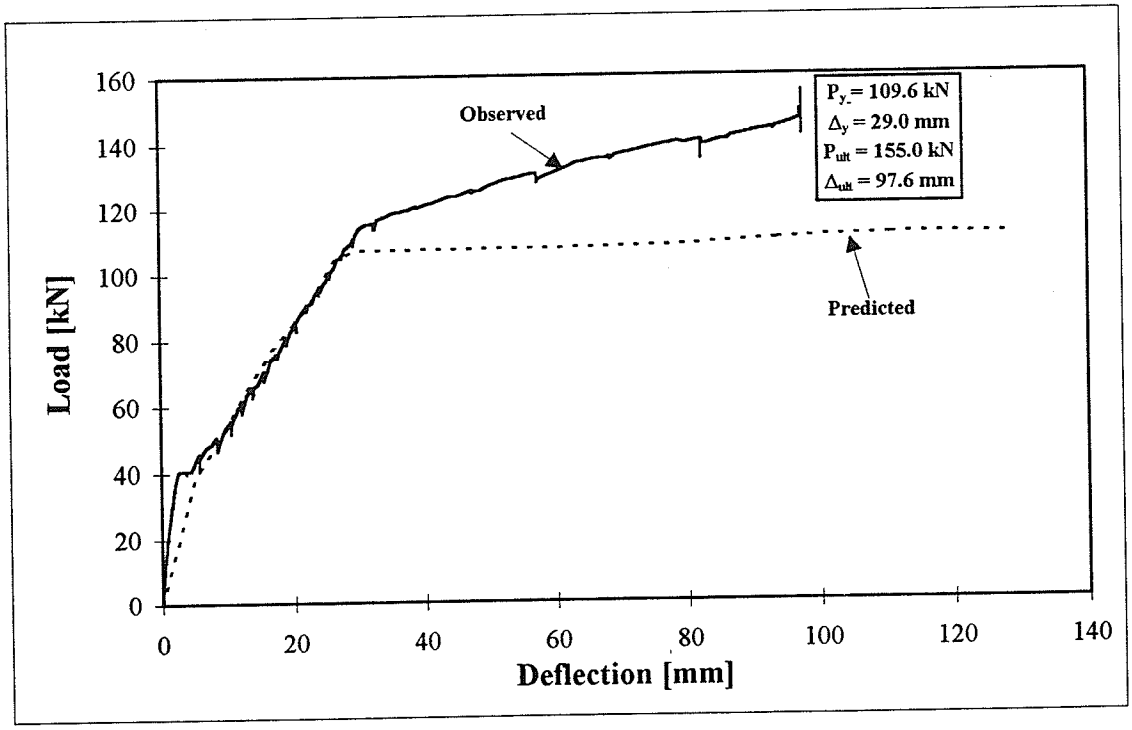

Figure 4.7: Predicted and observed midspan load-deflection diagram for slab S-150-T.

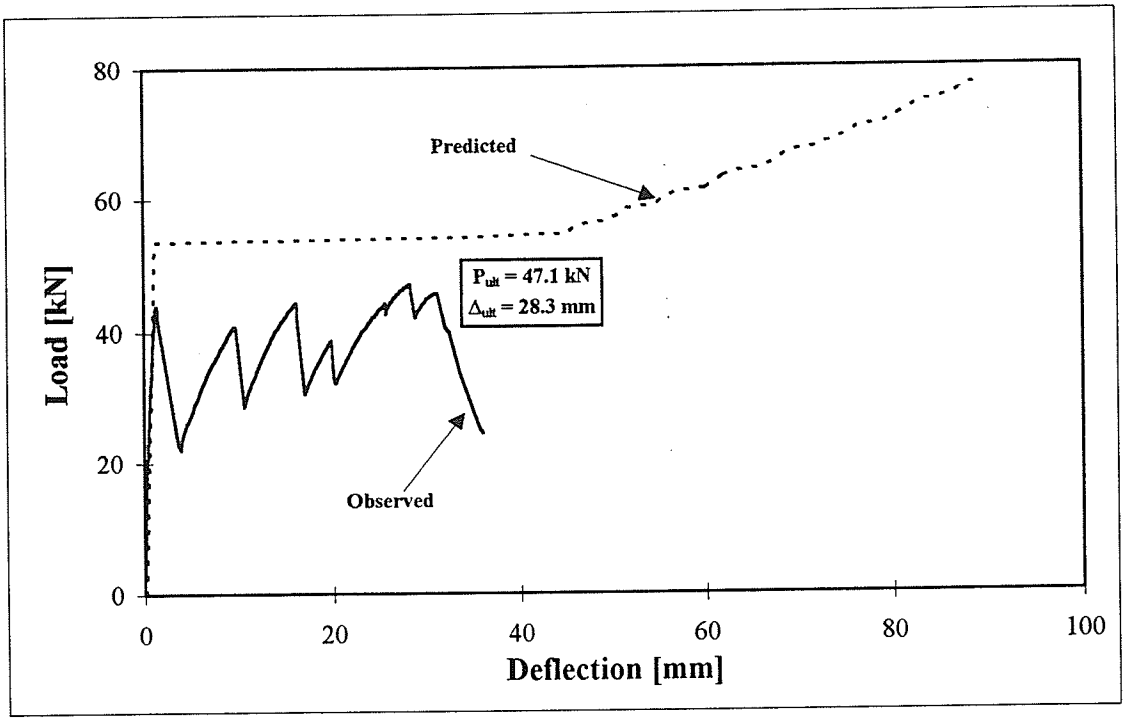

Figure 4.8: Predicted and observed midspan load-deflection diagram for slab I-200-A.

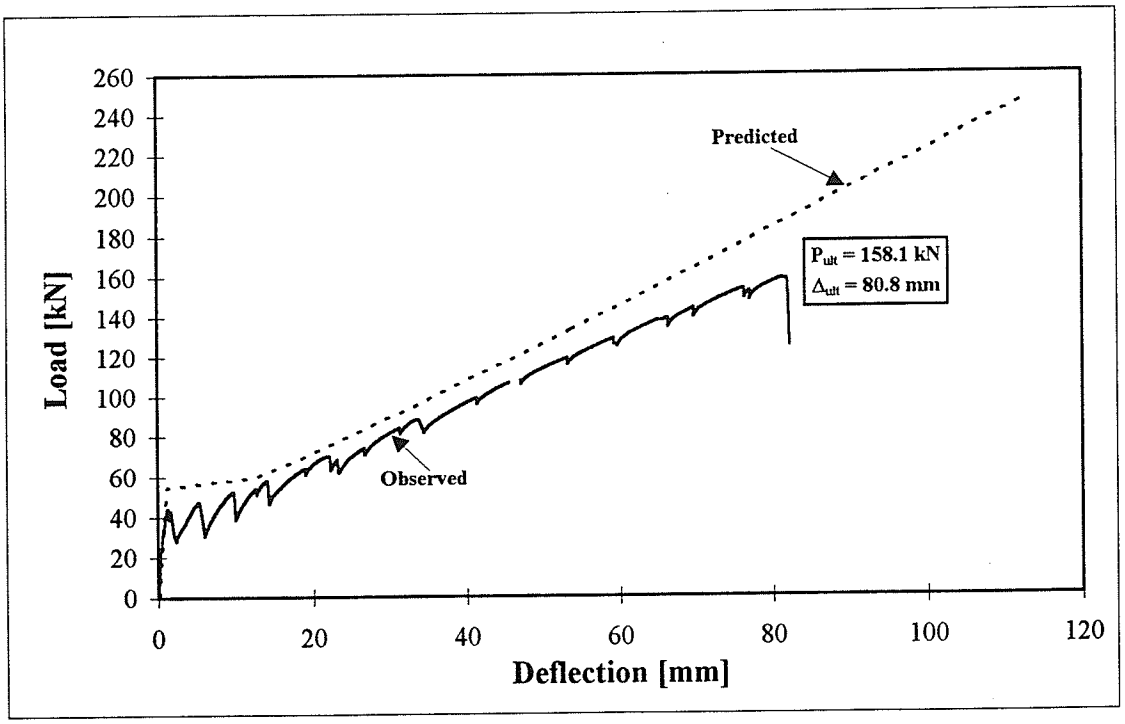

Figure 4.9: Predicted and observed midspan load-deflection diagram for slab I-200-C.

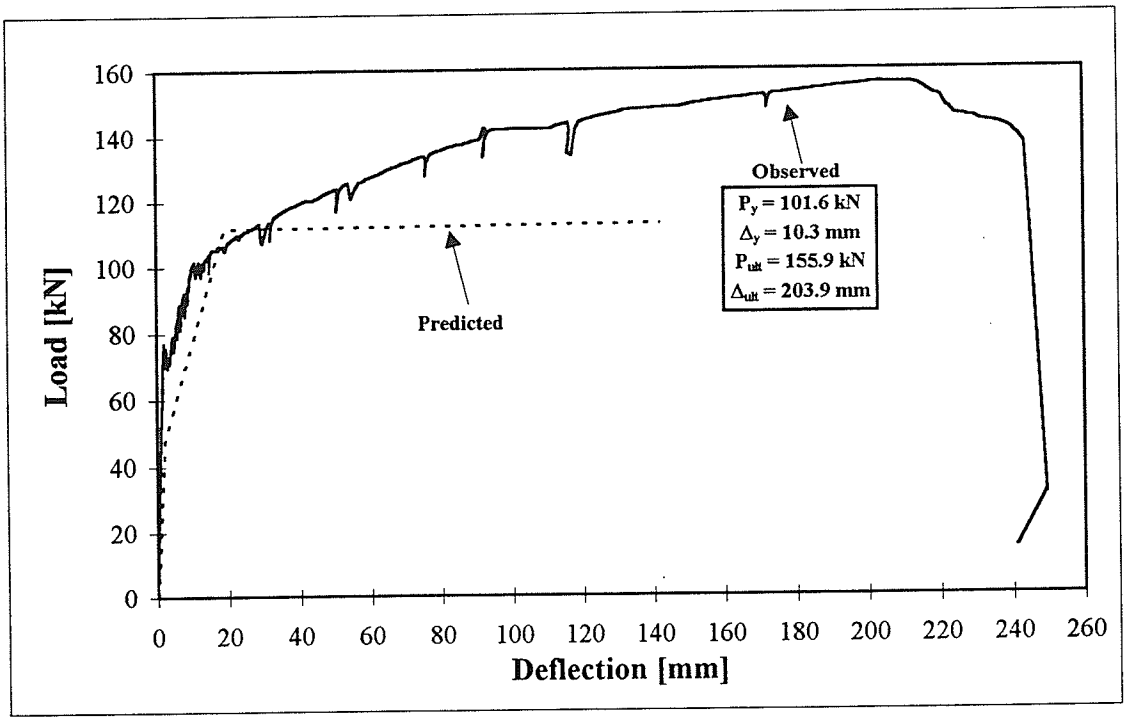

Figure 4.10: Predicted and observed midspan load-deflection diagram for slab S-200-T.

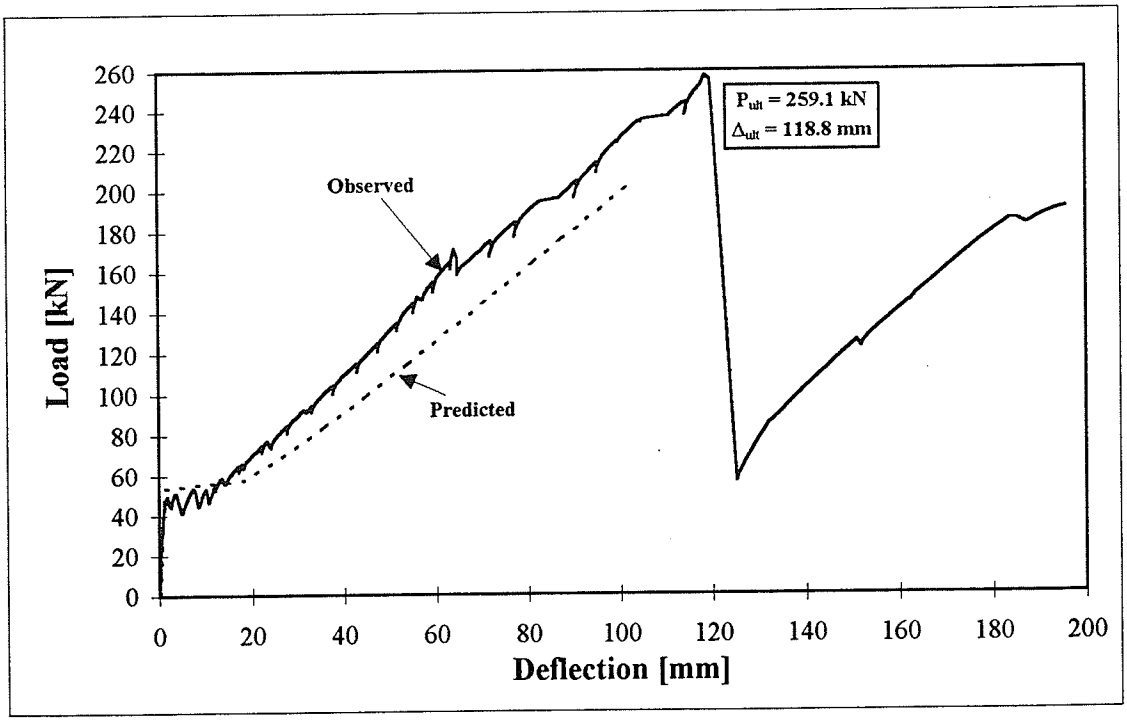

Figure 4.11: Predicted and observed midspan load-deflection diagram for slab LL-200-C.

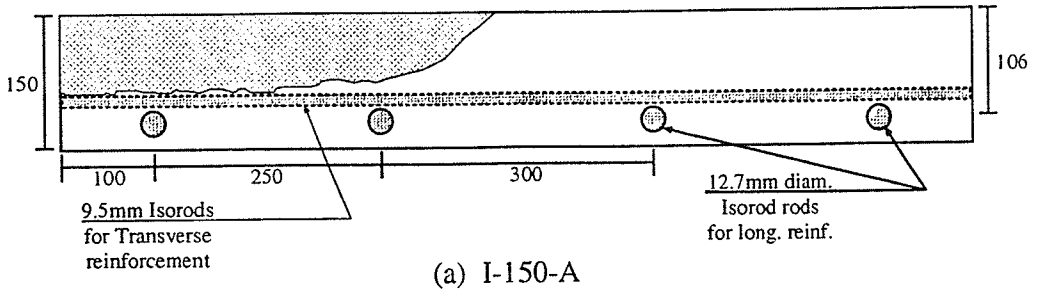

(a) I-150-A

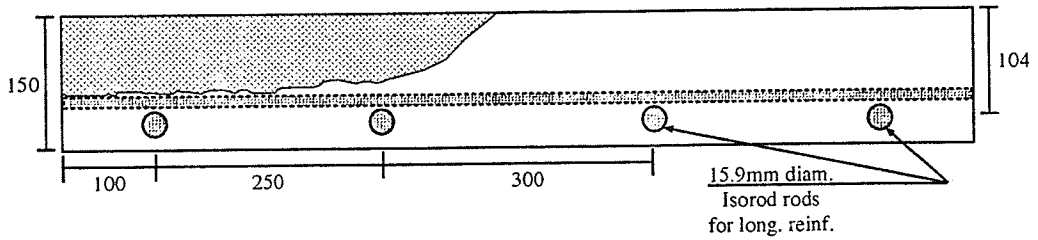

(b) I-150-B

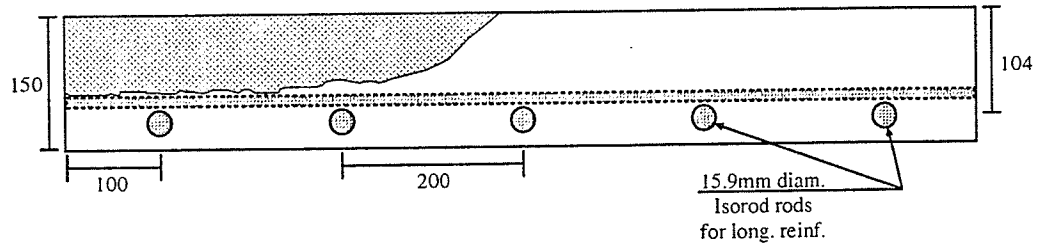

(c) I-150-C

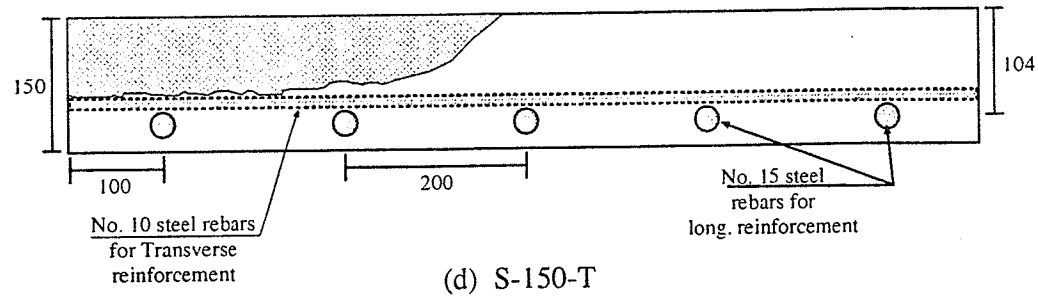

(d) S-150-T

Figure 4.12 (a) to (d): Cross-sections of the 150 mm thick slabs.

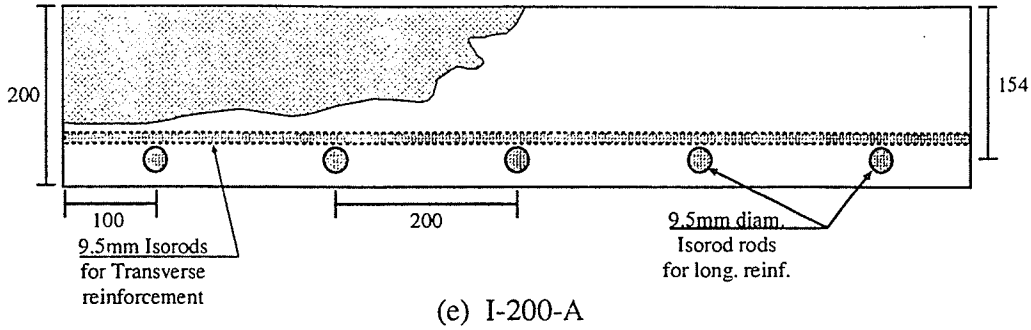

(e) I-200-A

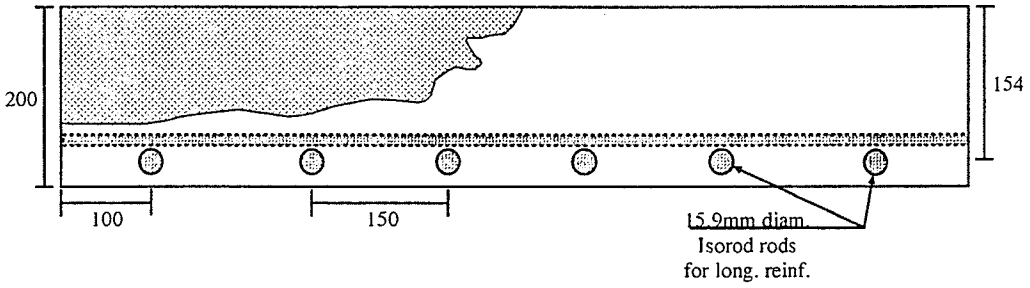

(f) I-200-C

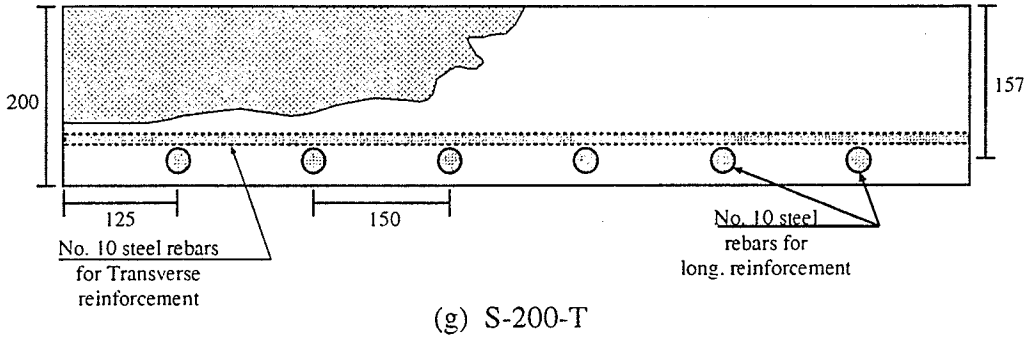

(g) S-200-T

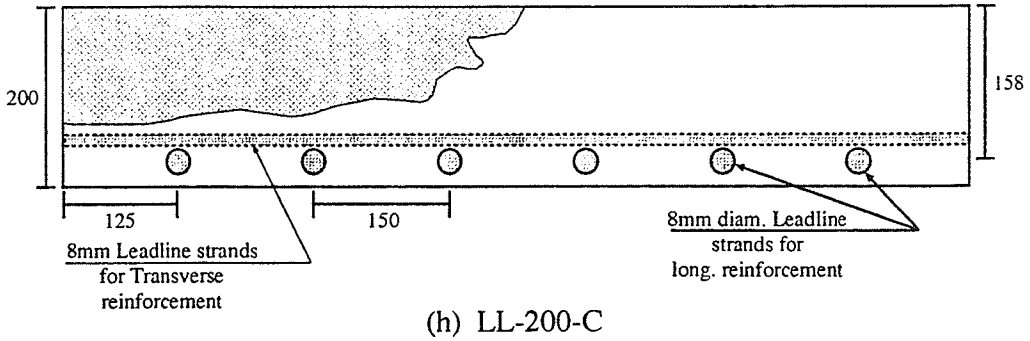

(h) LL-200-C

Figure 12 (e) to (h): Cross-sections of the 200 mm thick slabs.

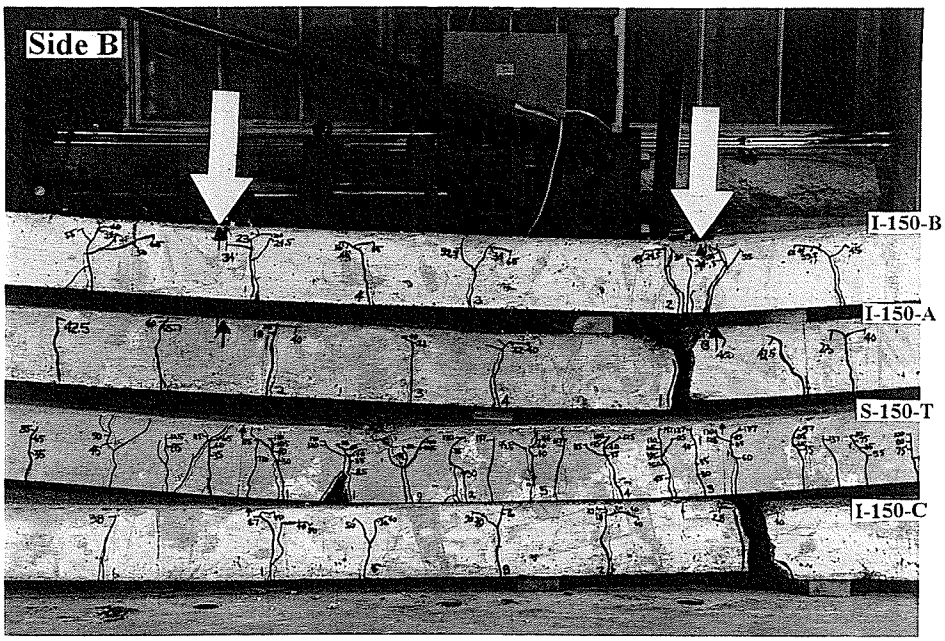

Figure 4.13: Crack patterns of the 150 mm thick slabs.

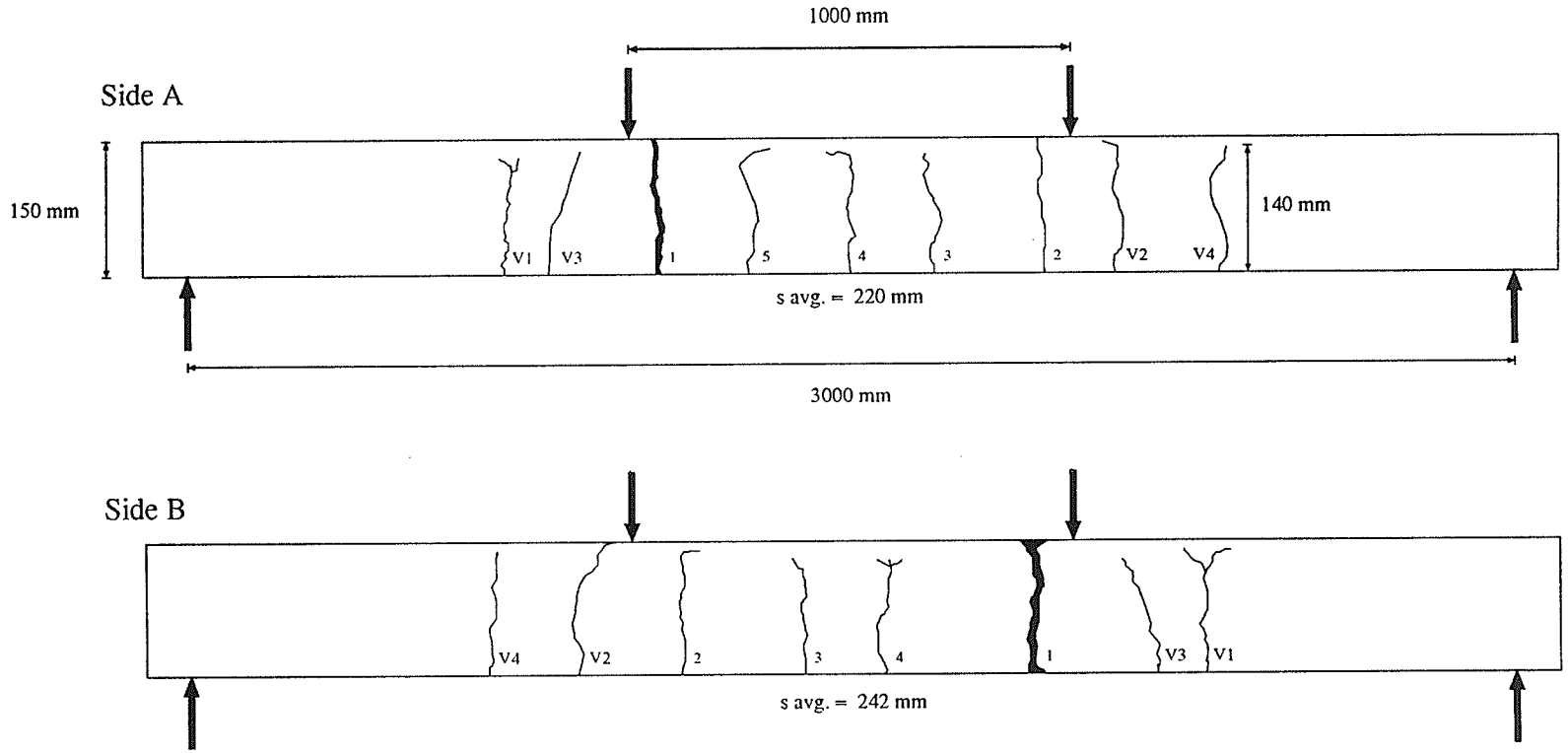

Figure 4.14: Crack patterns of slab I-150-A.

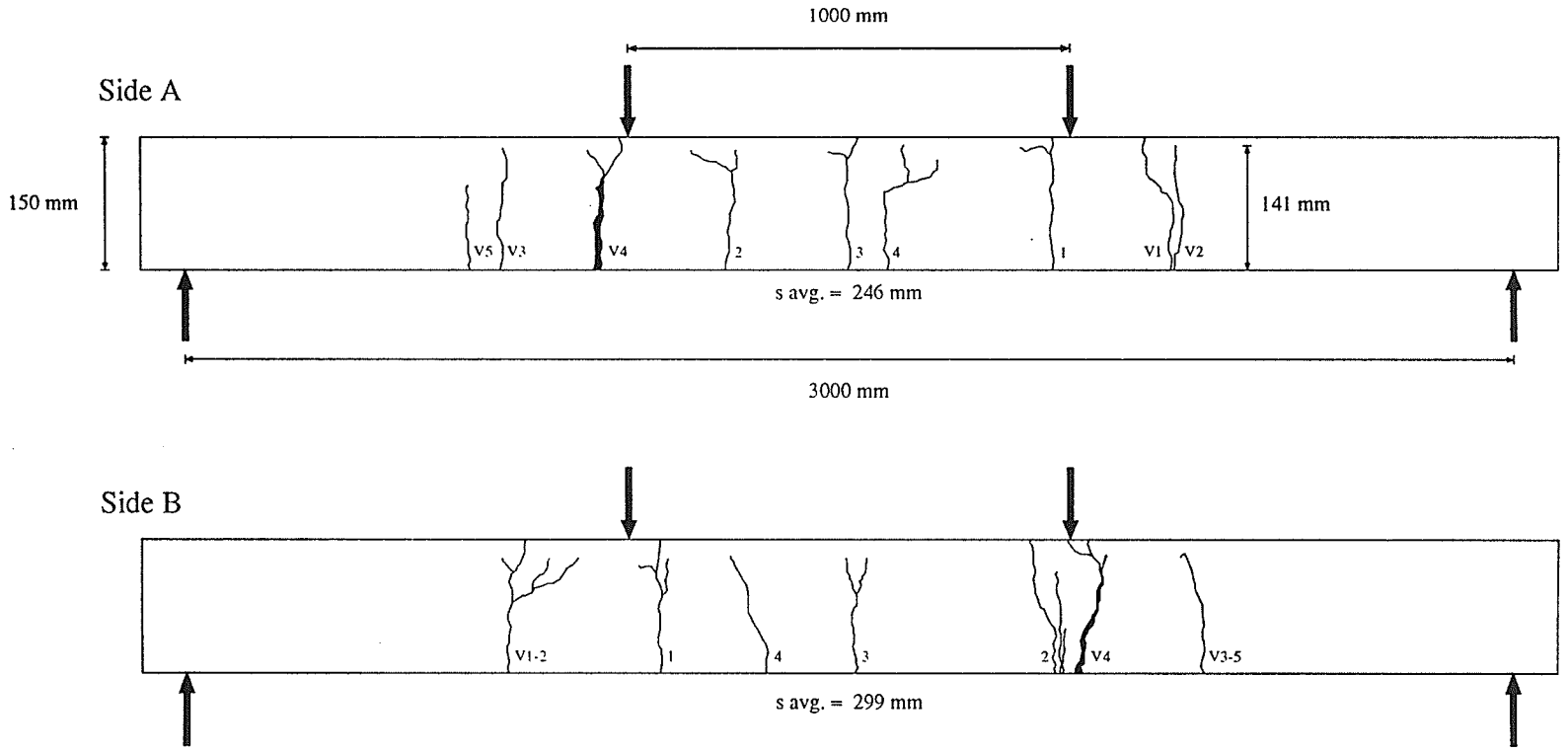

Figure 4.15: Crack patterns of slab I-150-B.

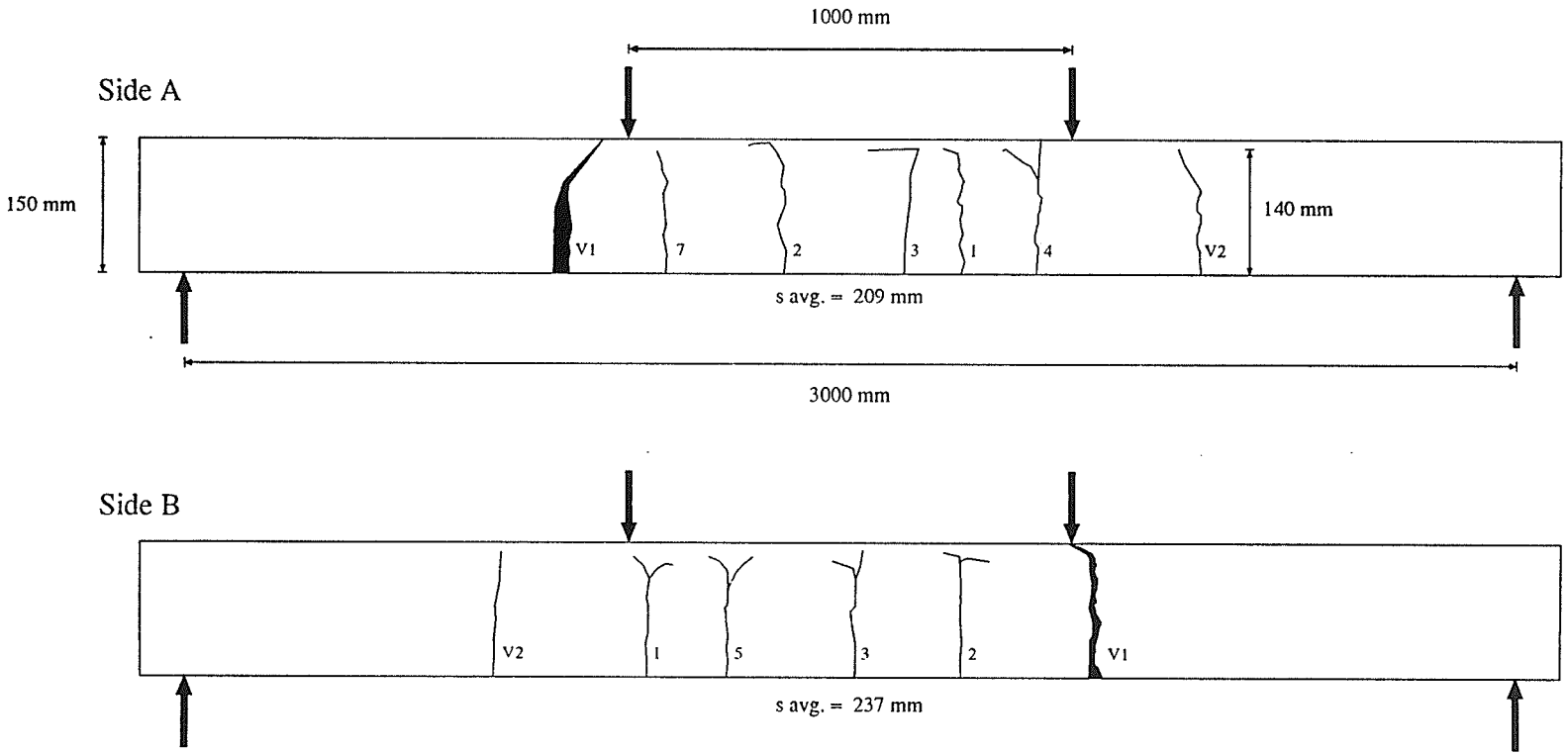

Figure 4.16: Crack patterns of slab I-150-C.

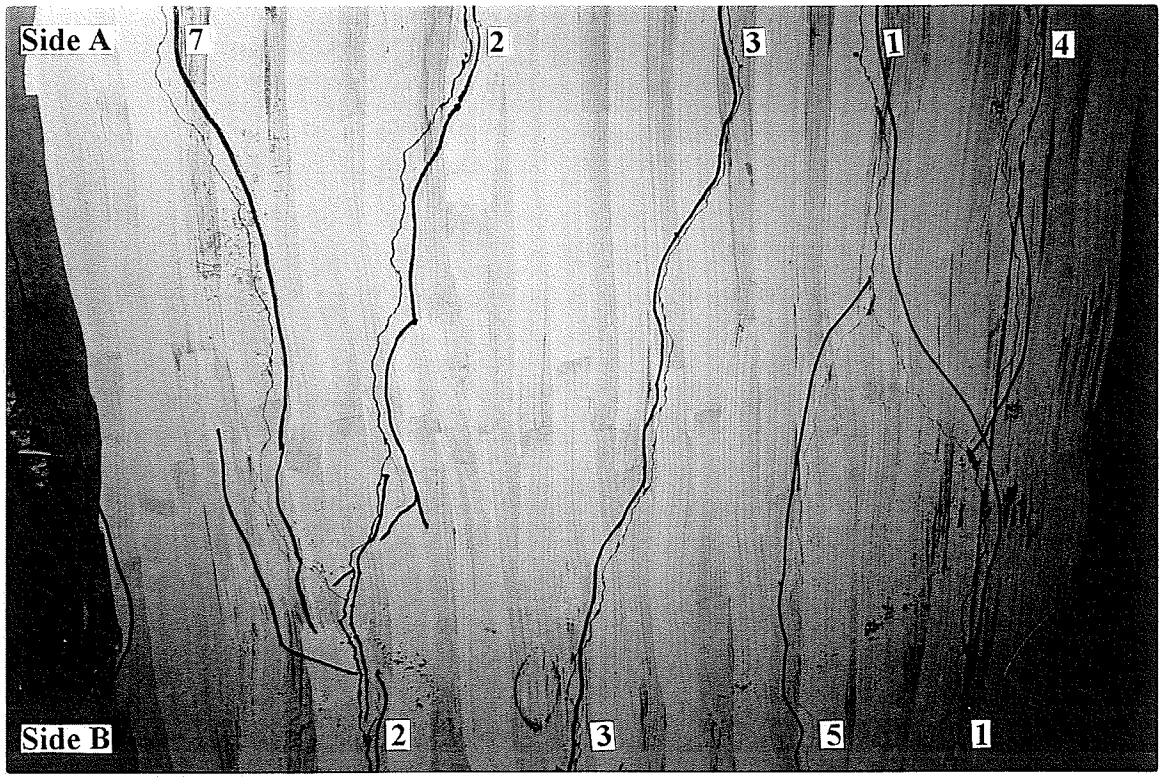

Figure 4.17: Bottom view of slab I-150-C after failure.

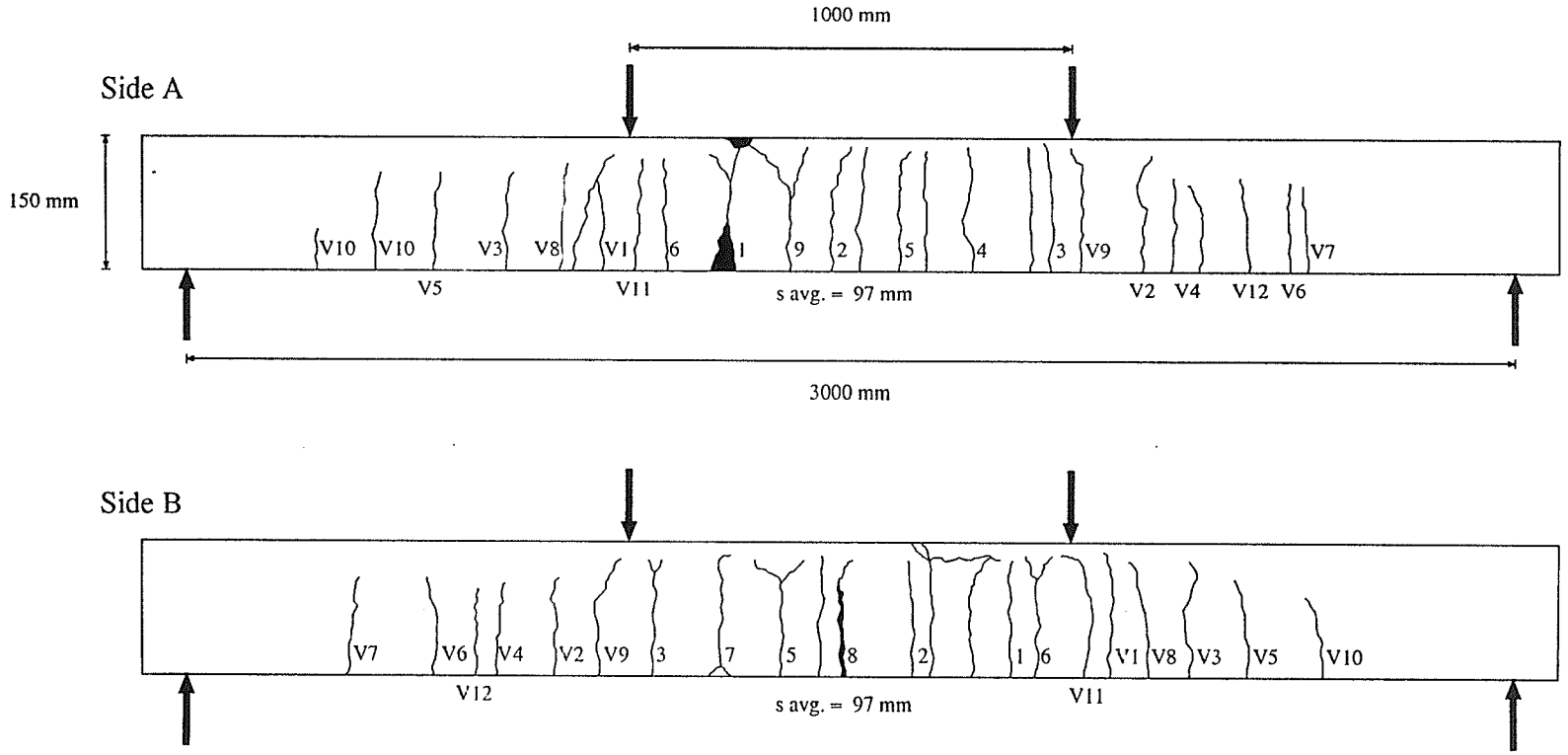

Figure 4.18: Crack patterns of slab S-150-T.

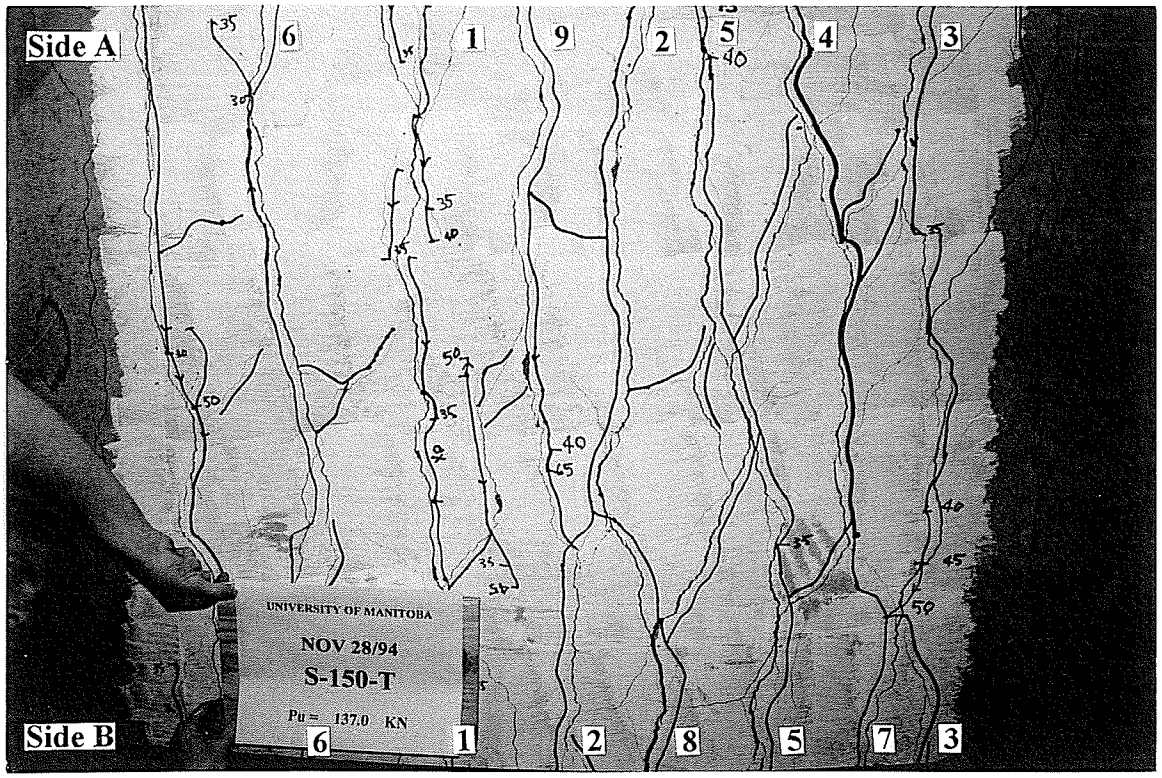

Figure 4.19: Bottom view of slab S-150-T after failure.

Figure 4.20: Crack patterns of the 200 mm thick slabs.

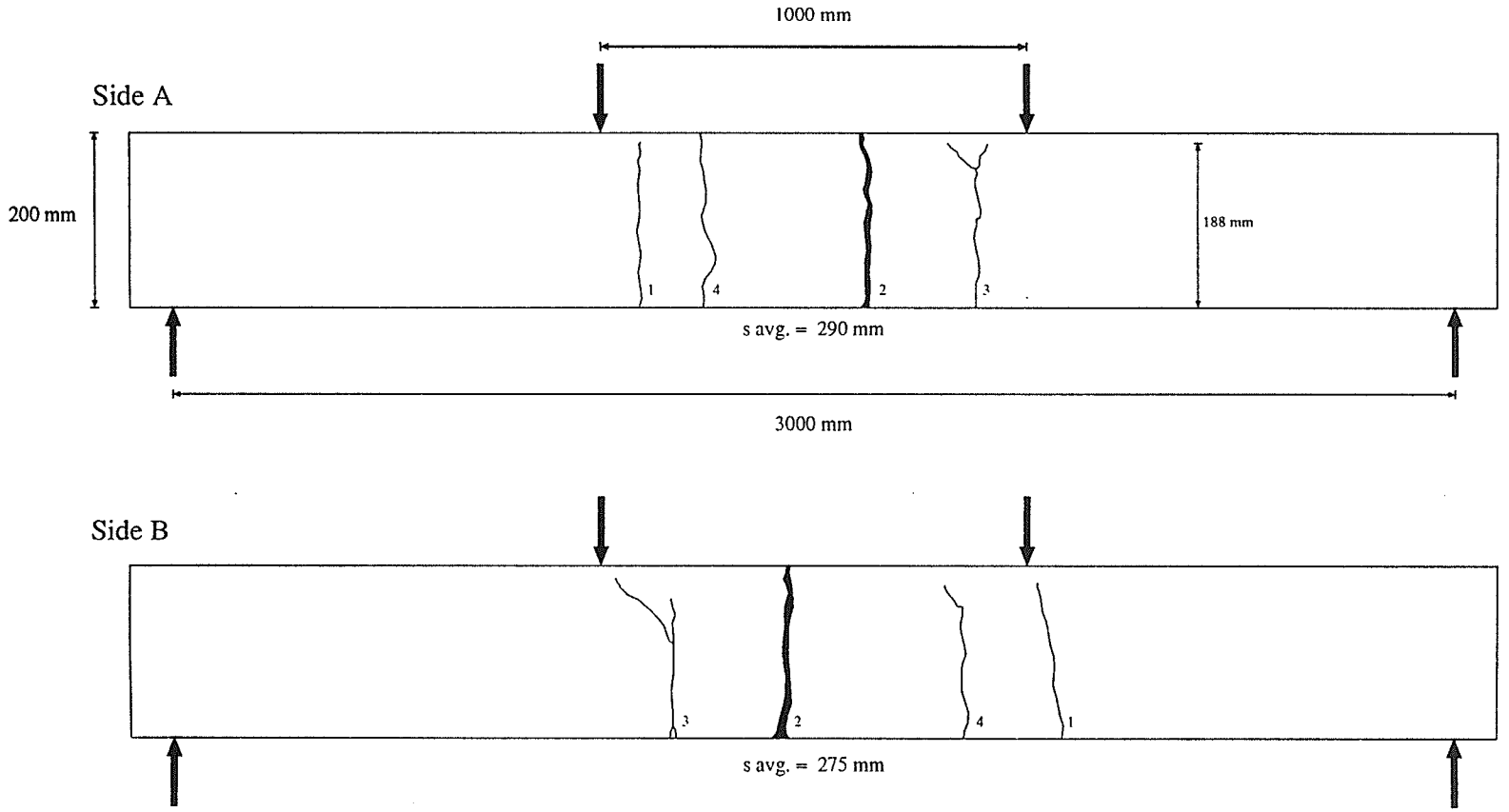

Figure 4.21: Crack patterns of slab I-200-A.

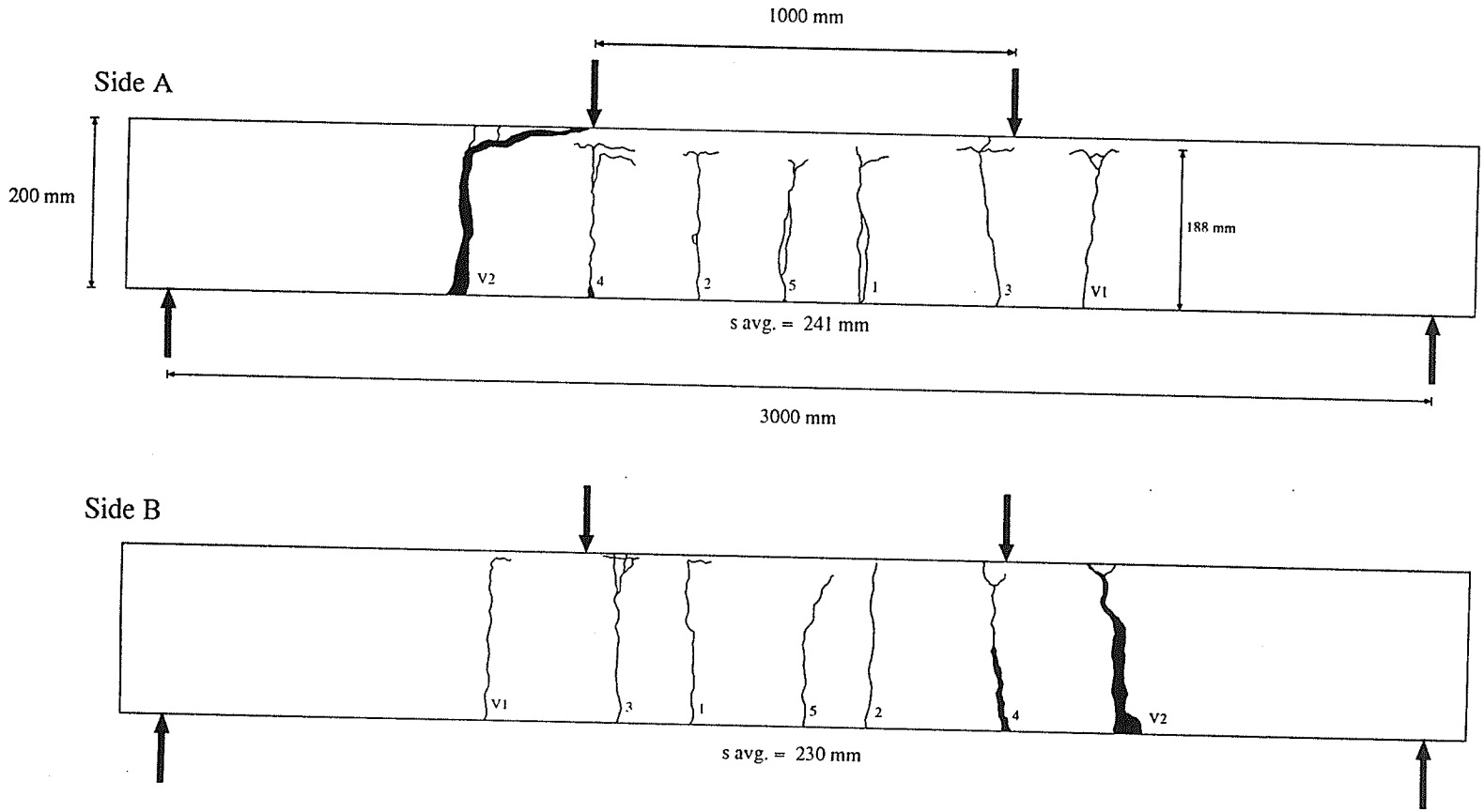

Figure 4.22: Crack patterns of slab I-200-C.

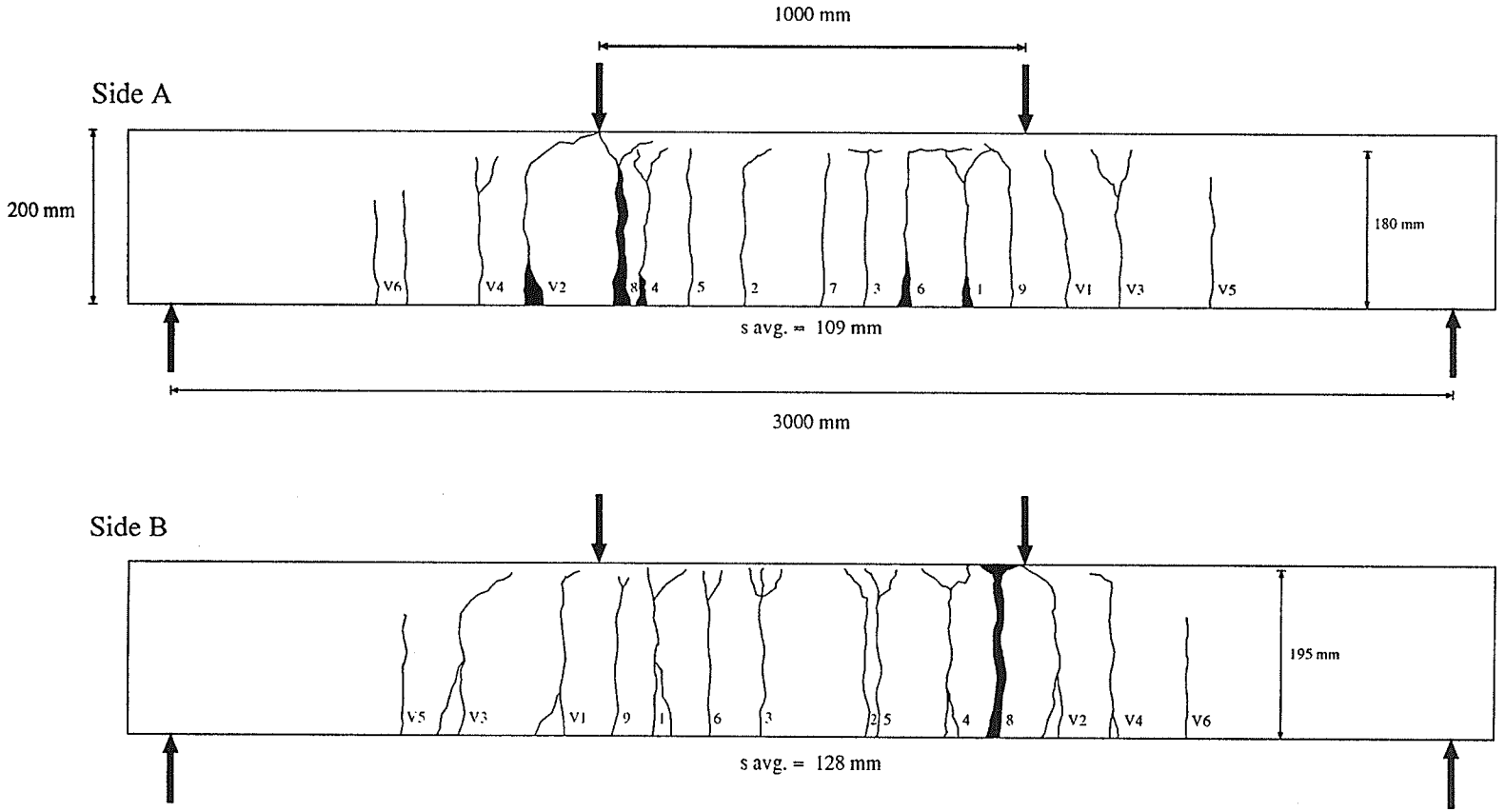

Figure 4.23: Crack patterns of slab S-200-T.

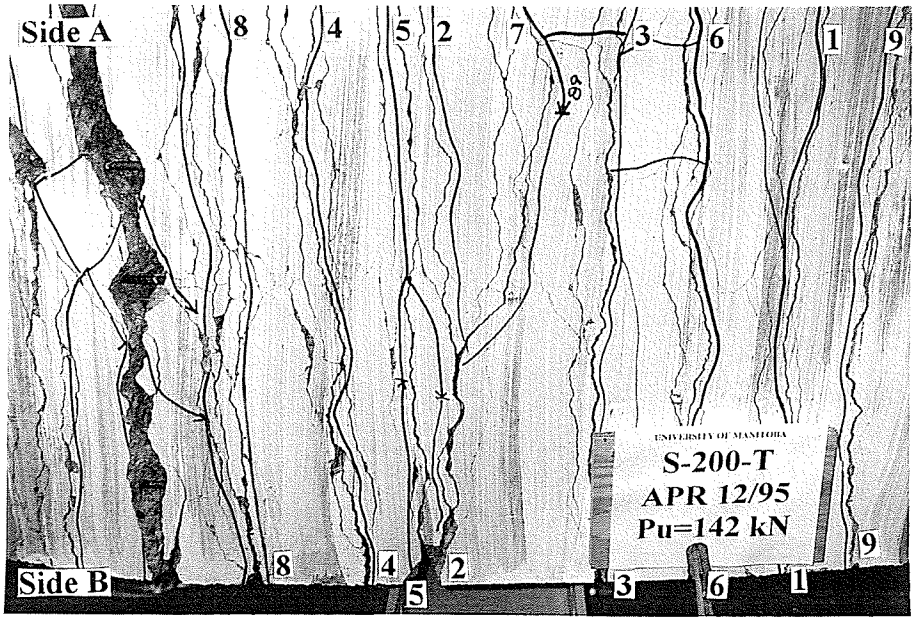

Figure 4.24: Bottom view of slab S-200-T after failure.

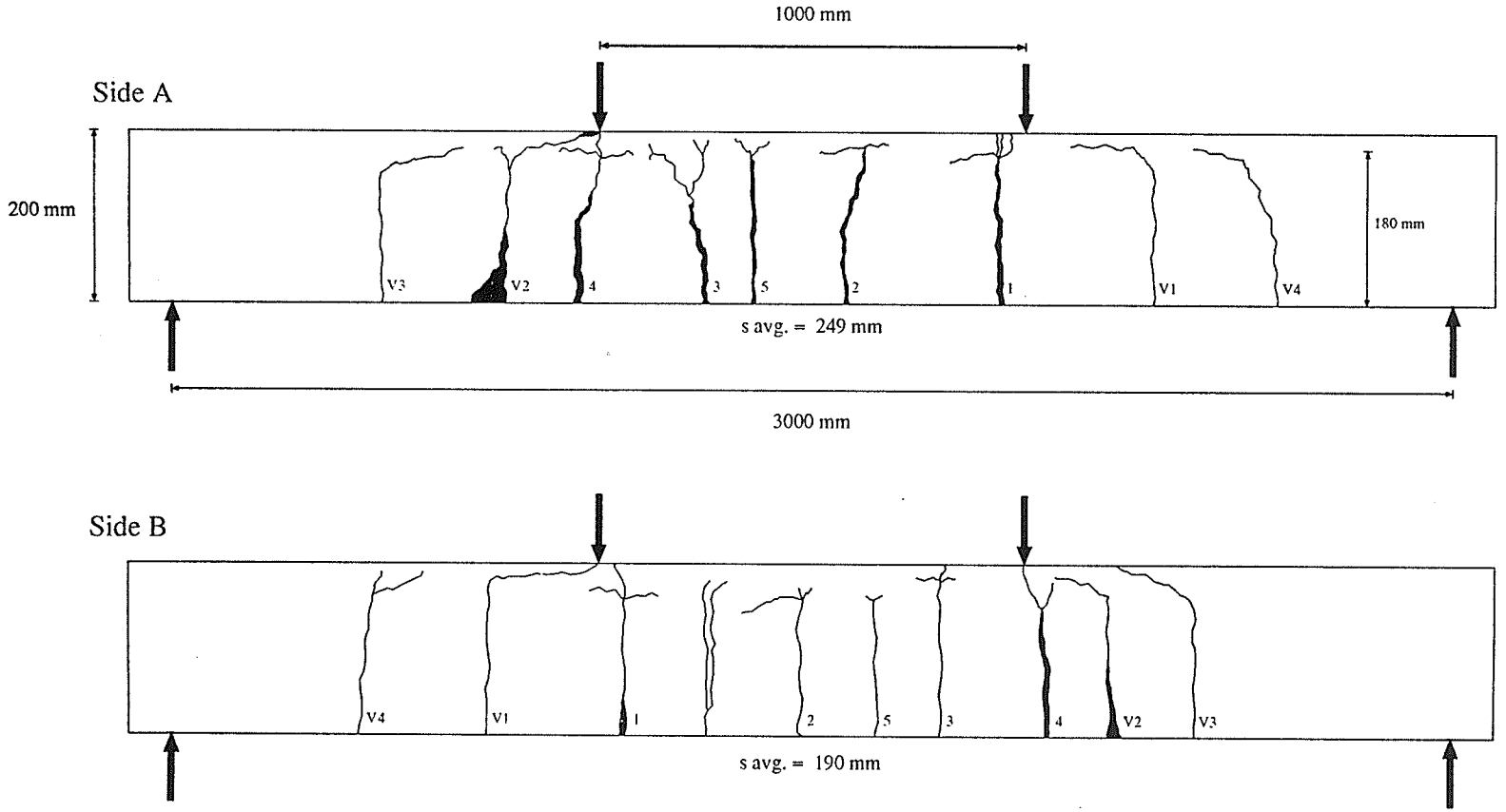

Figure 4.25: Crack patterns of slab LL-200-C.

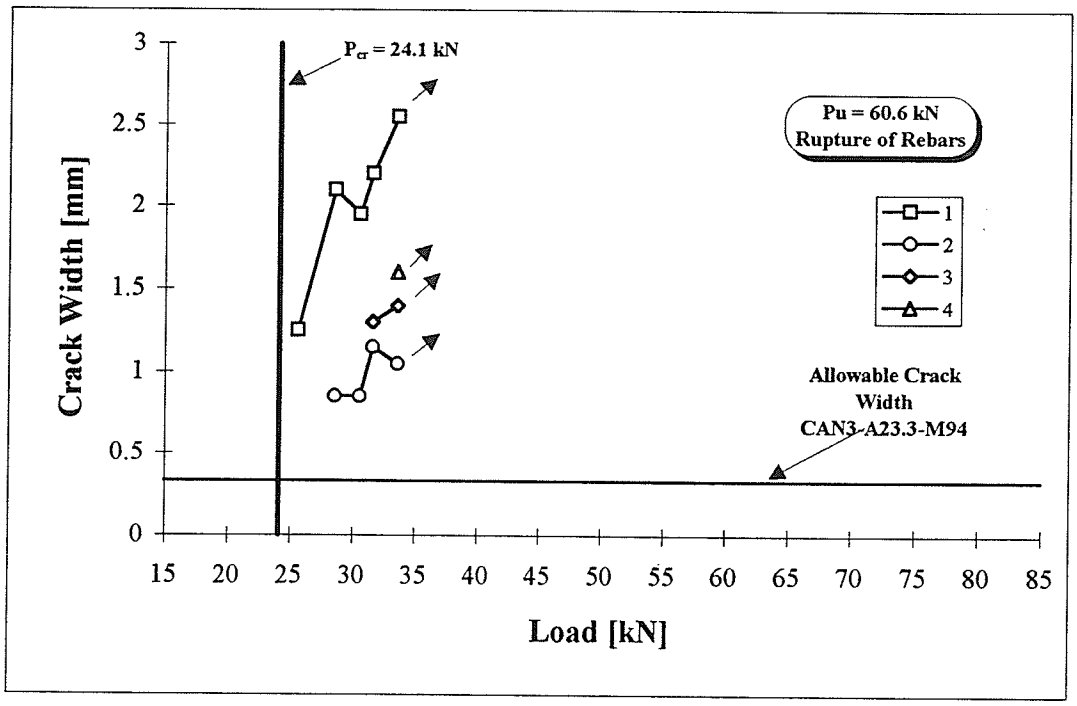

Figure 4.26: Crack widths vs. load diagram for slab I-150-A.

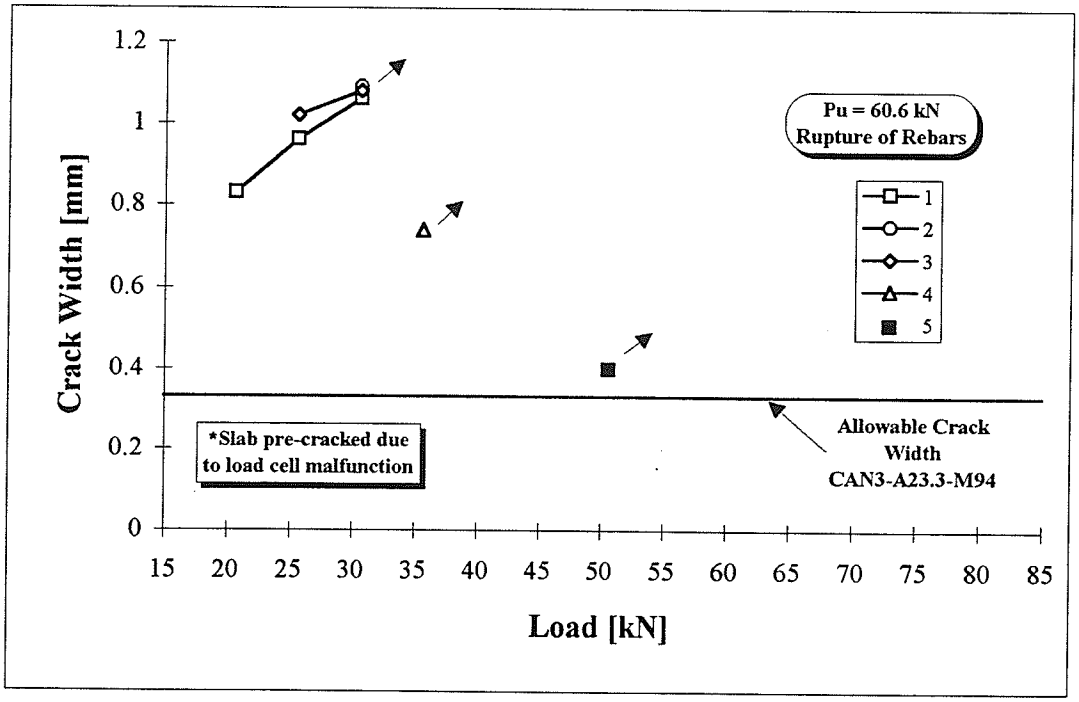

Figure 4.27: Crack widths vs. load diagram for slab I-150-C.

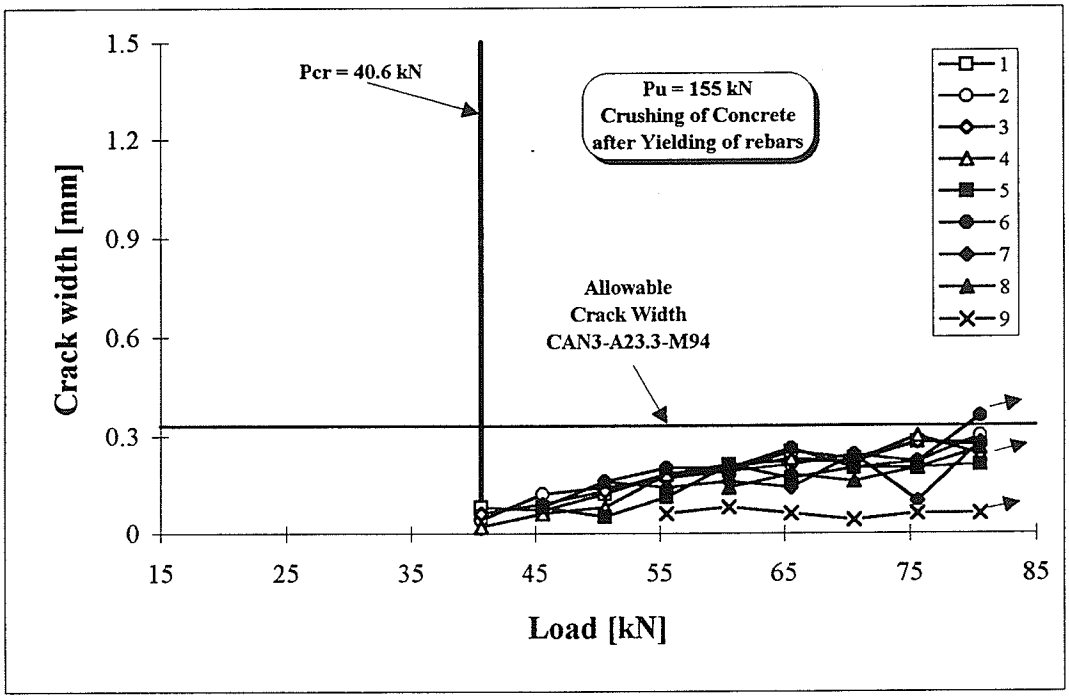

Figure 4.28: Crack width vs. load for slab S-150-T.

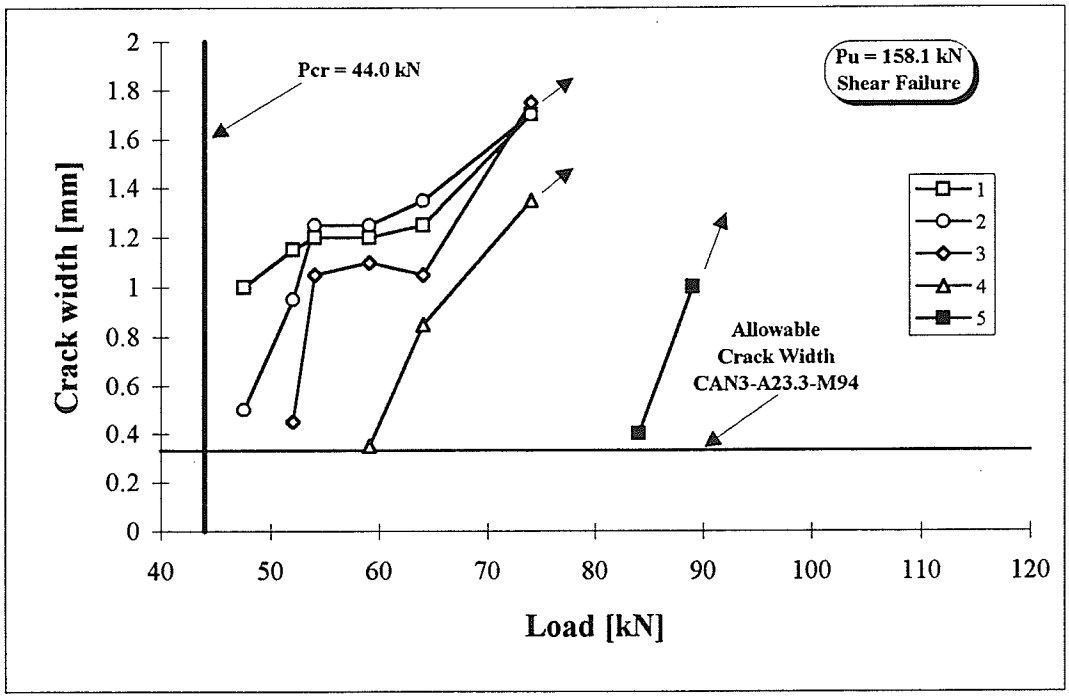

Figure 4.29: Crack width vs. load for slab I-200-C.

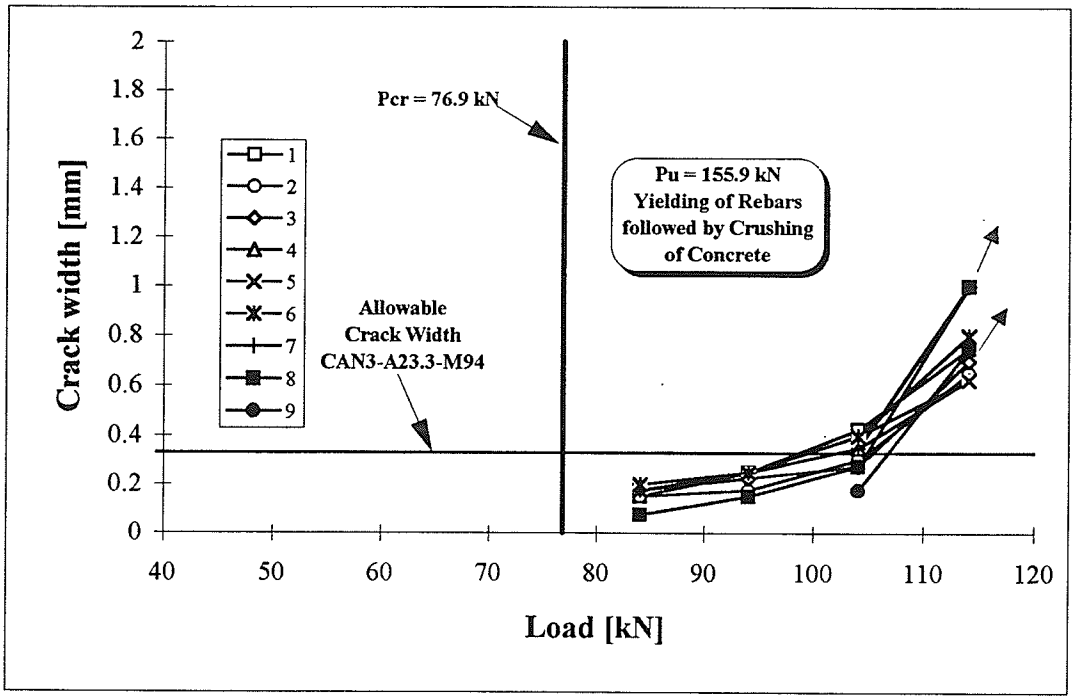

Figure 4.30: Crack width vs. load for slab S-200-T.

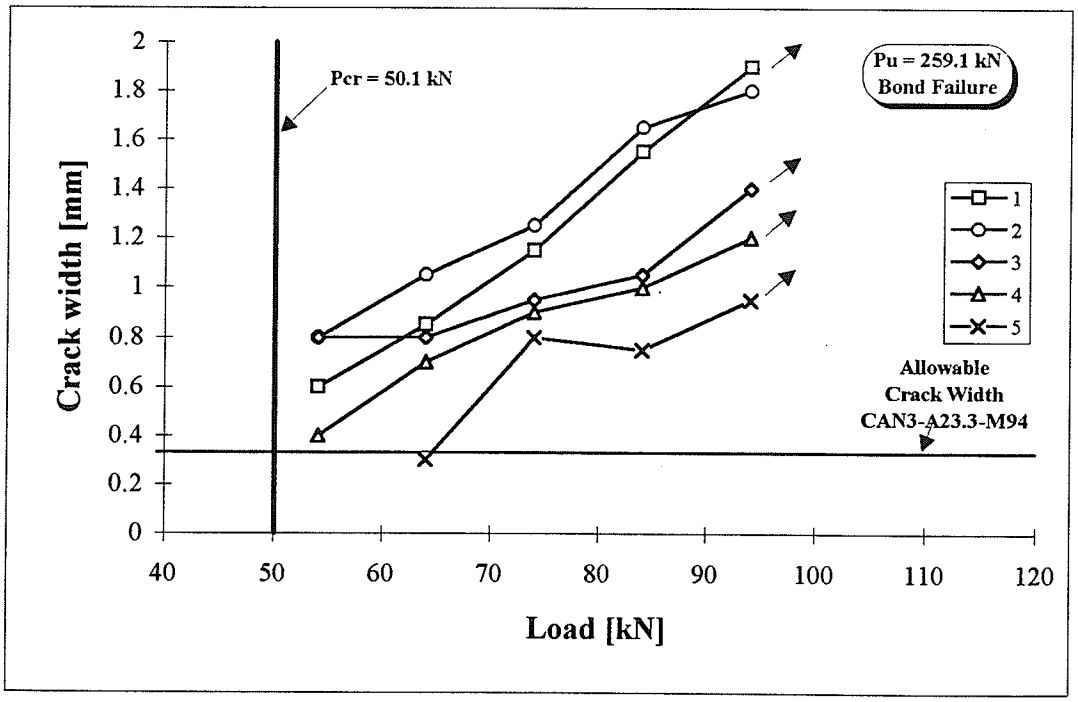

Figure 4.31: Crack width vs. load for slab LL-200-C.

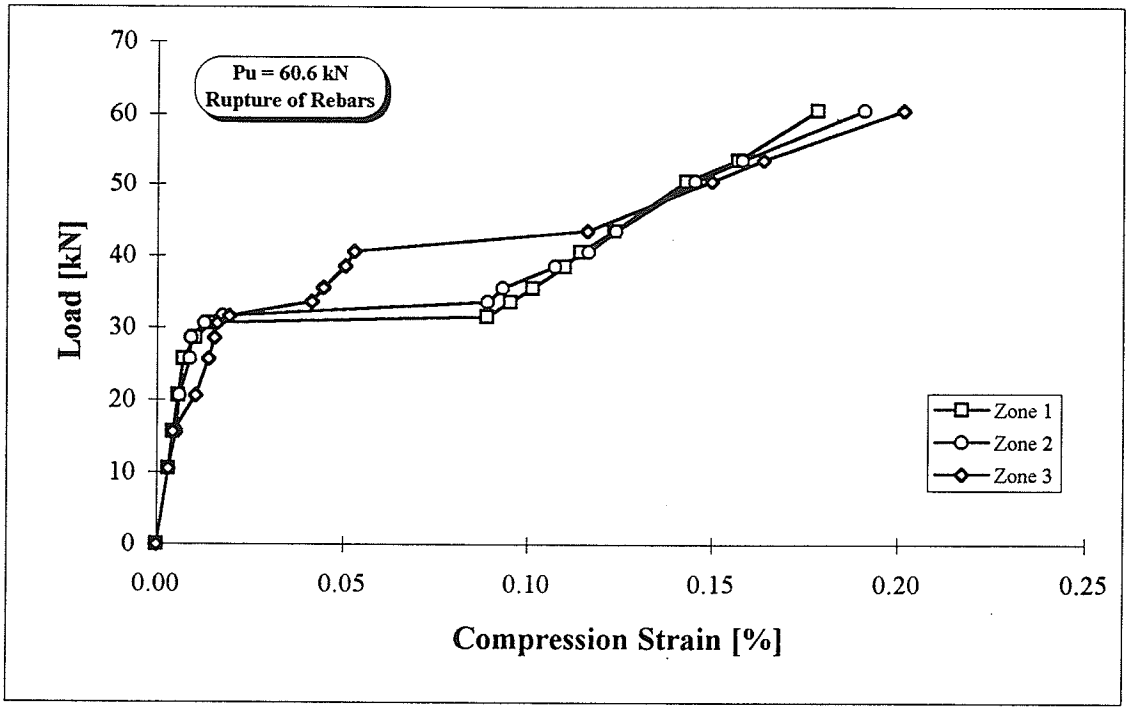

Figure 4.32: Load-compression strain behaviour at the top of slab I-150-A.

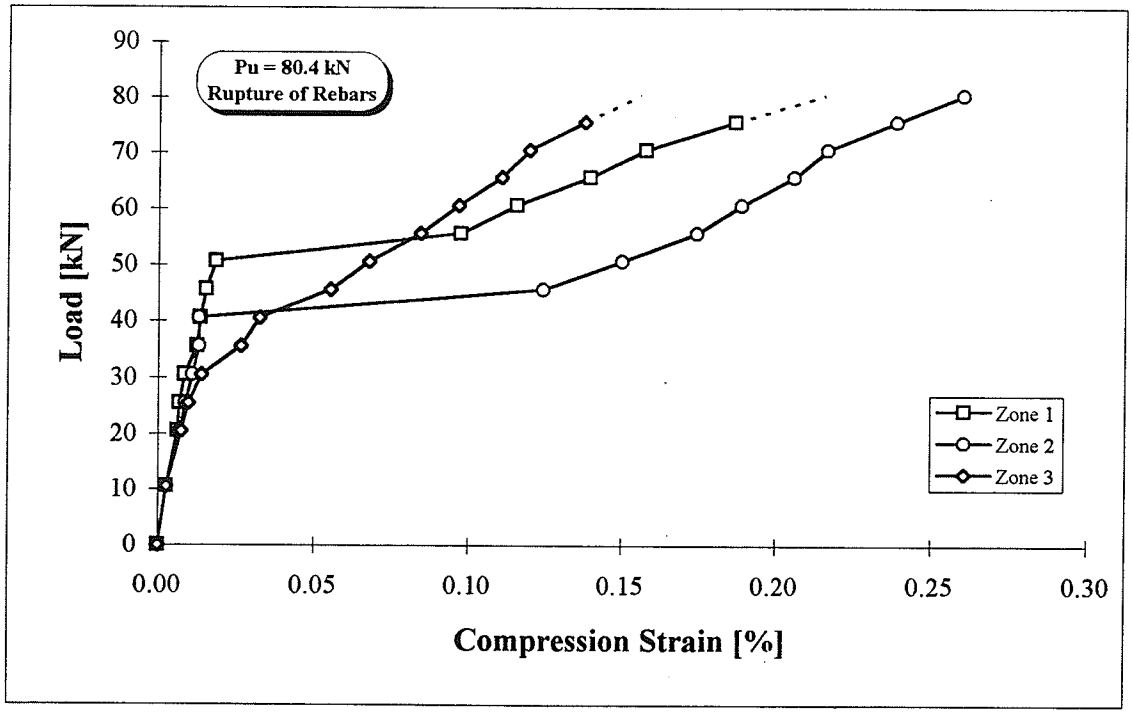

Figure 4.33: Load-compression strain behaviour at the top of slab I-150-B.

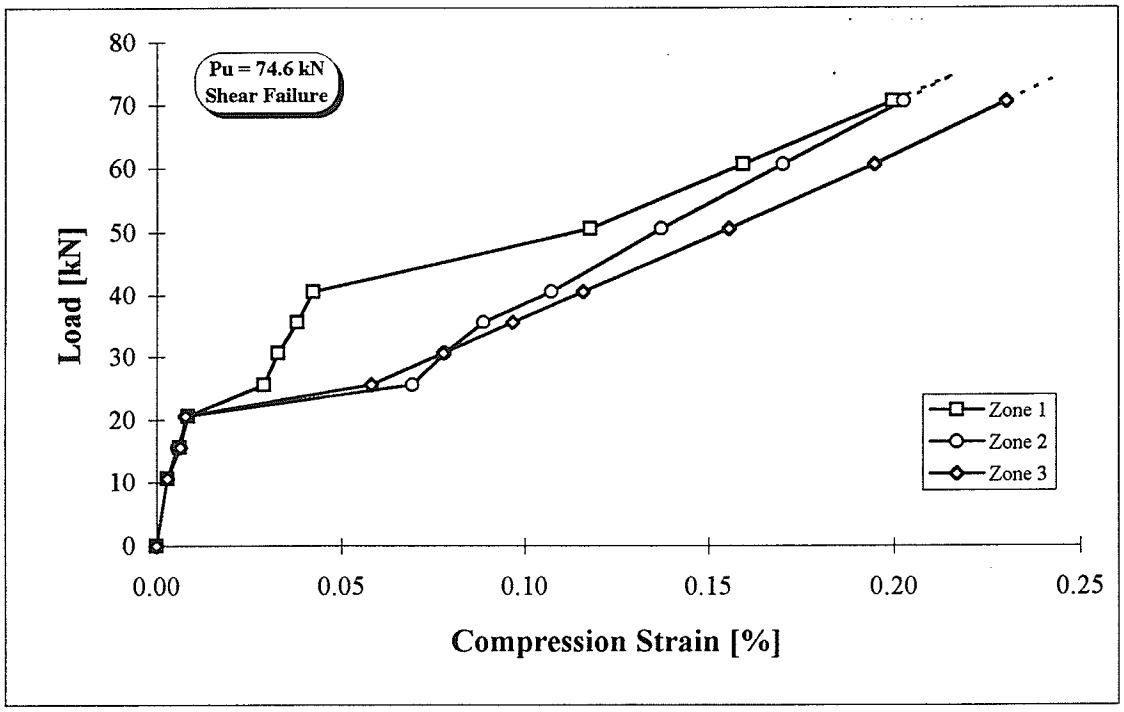

Figure 4.34: Load-compression strain behaviour at the top of slab I-150-C.

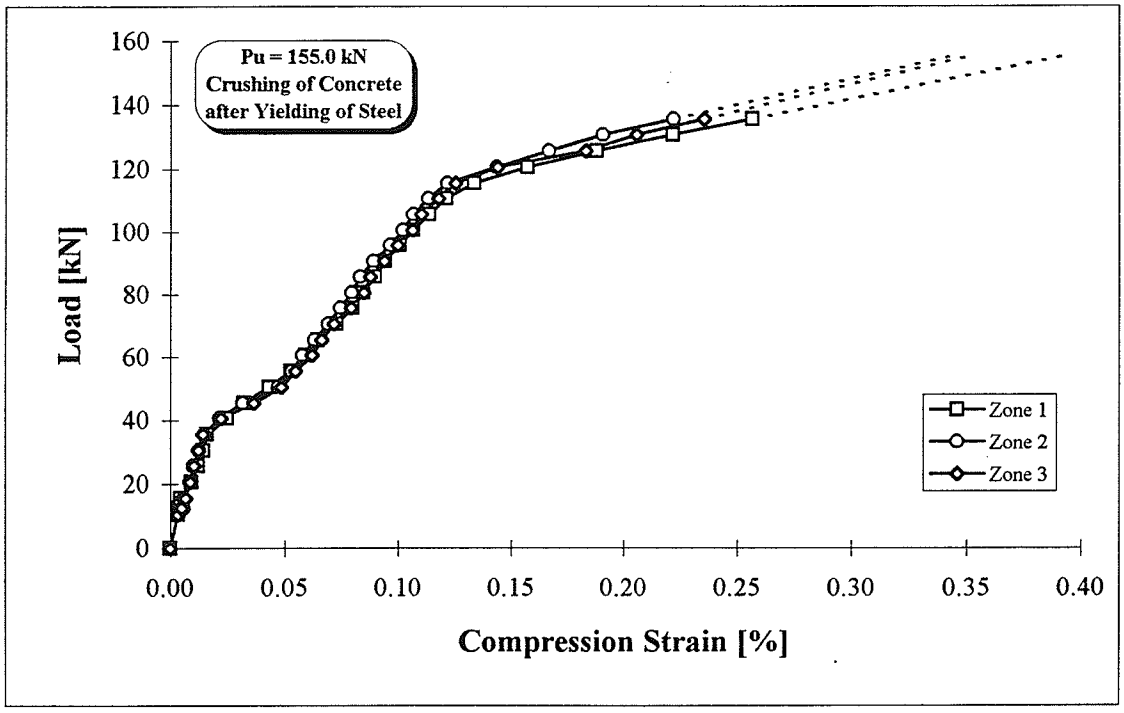

Figure 4.35: Load-compression strain behaviour at the top of slab S-150-T.

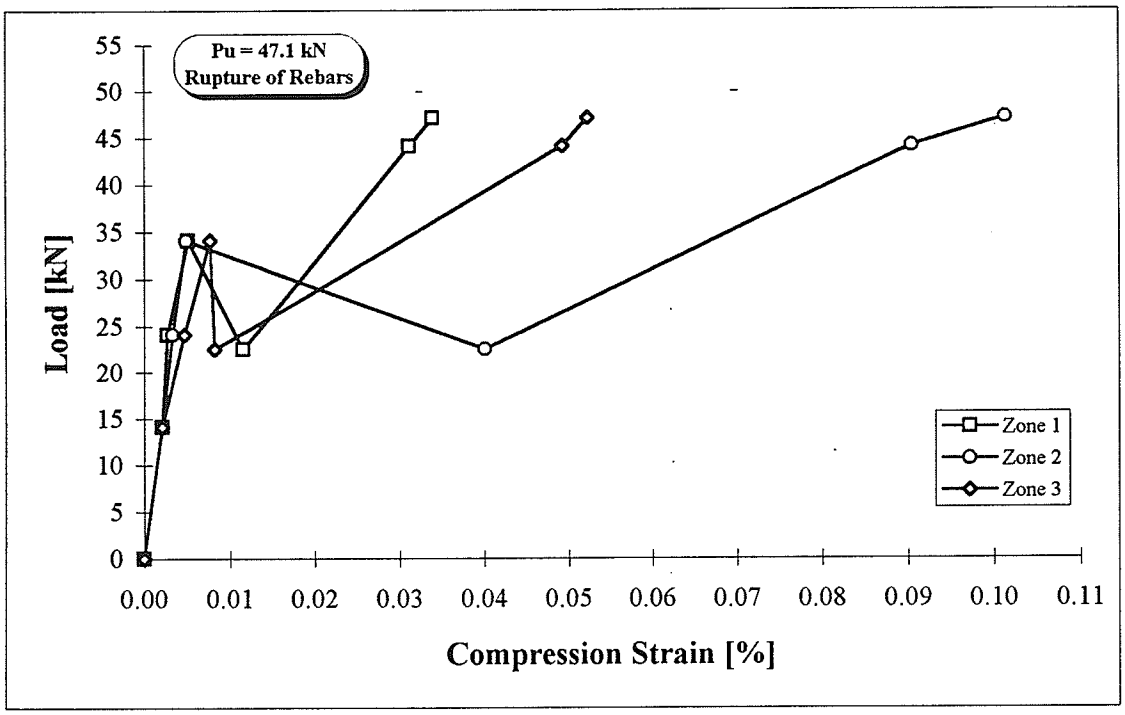

Figure 4.36: Load-compression strain behaviour at top of slab I-200-A.

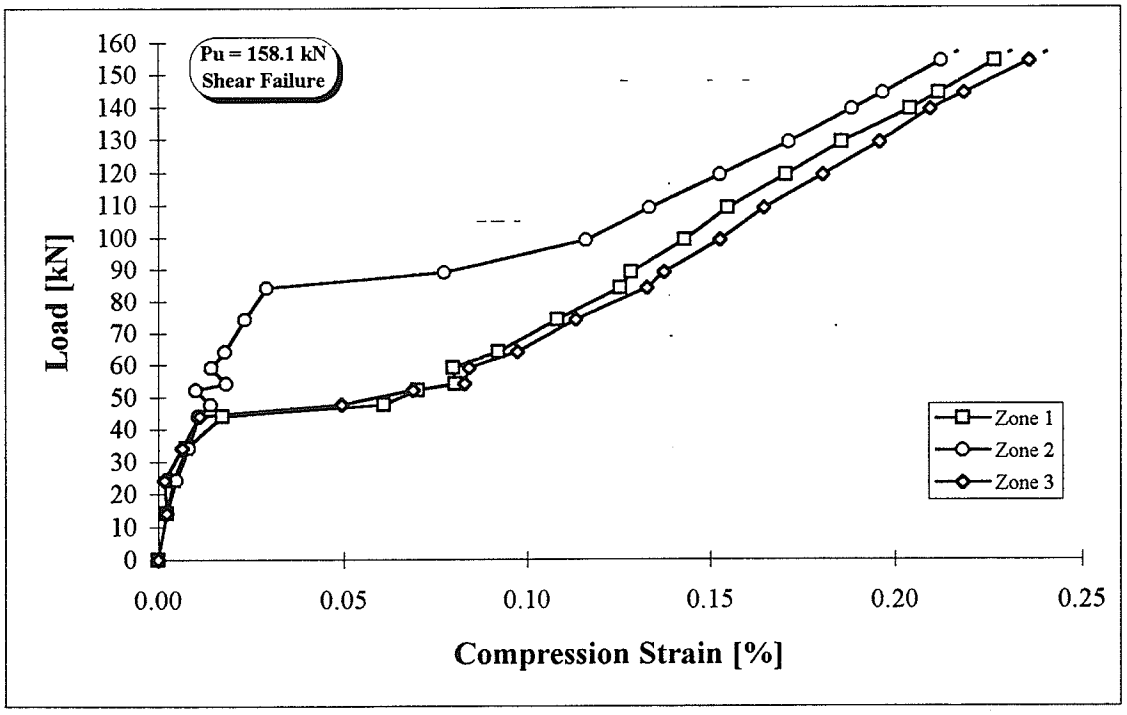

Figure 4.37: Load-compression strain behaviour at top of slab I-200-C.

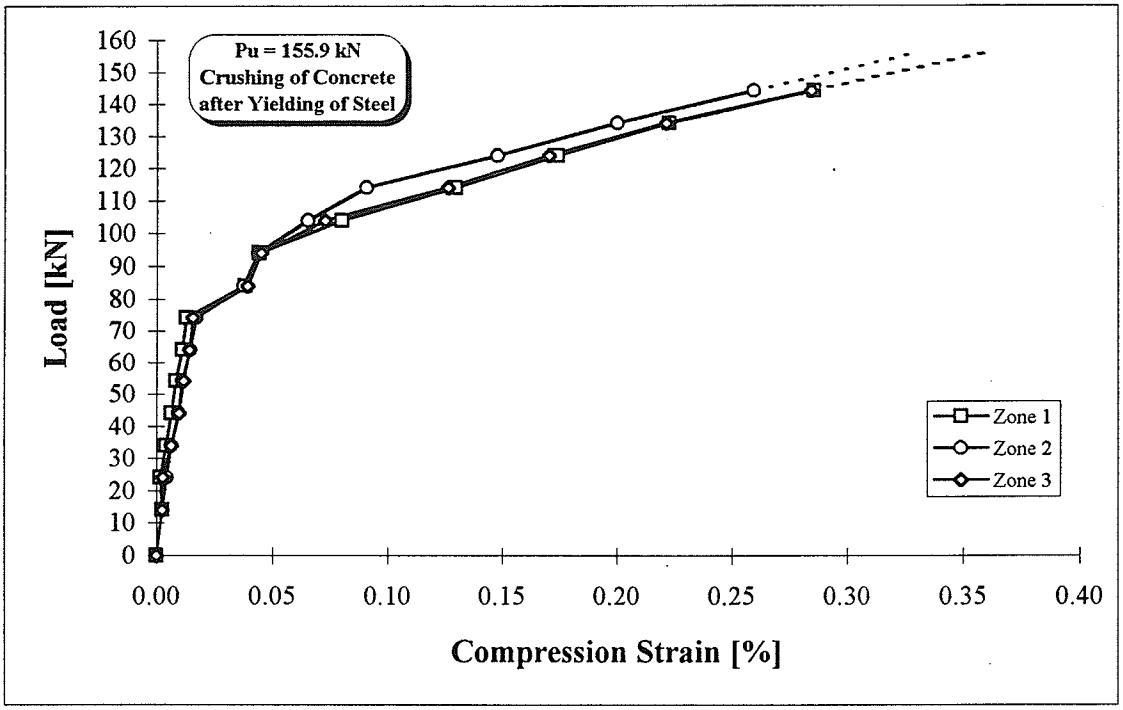

Figure 4.38: Load-compression strain behaviour at top of slab S-200-T.

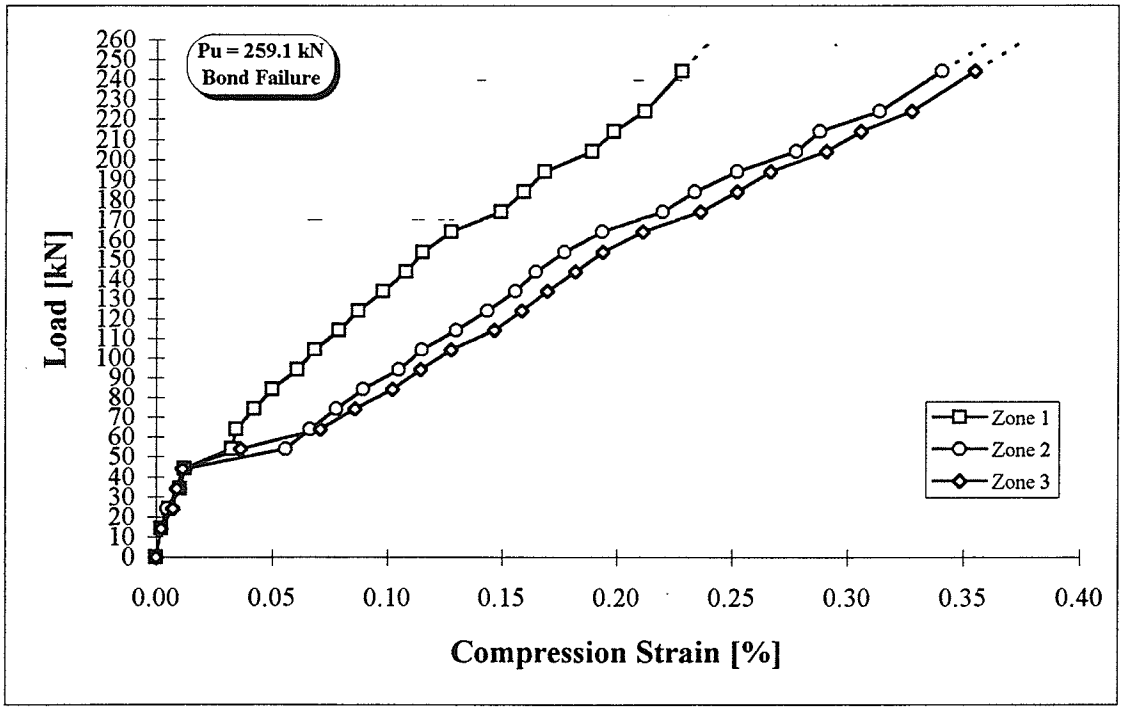

Figure 4.39: Load-compression strain behaviour at top of slab LL-200-C.

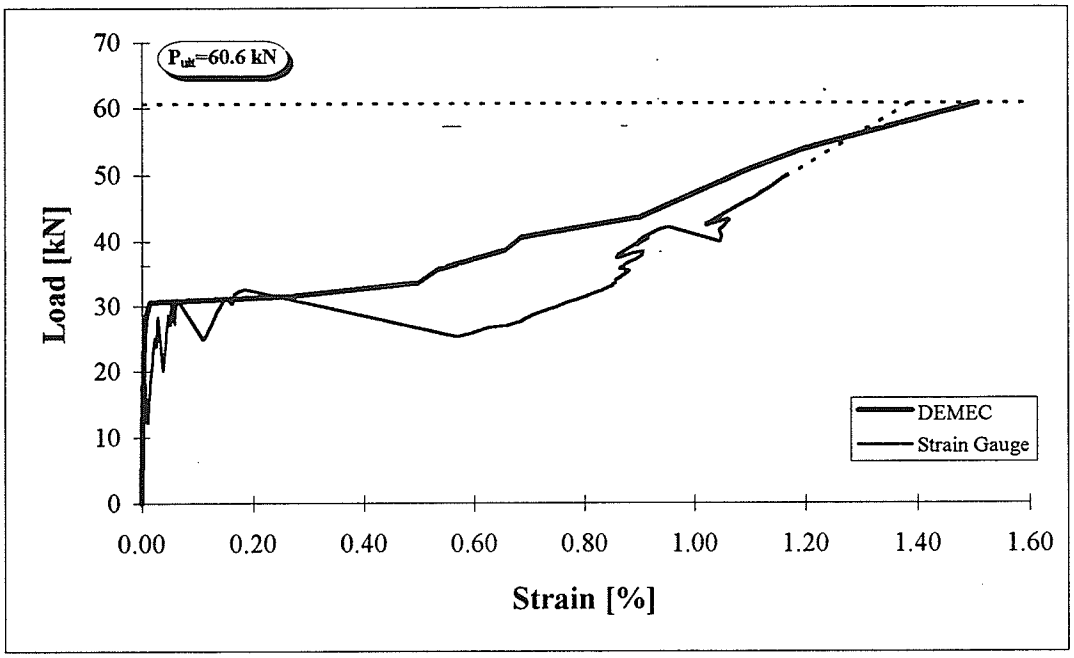

Figure 4.40: Load-tensile strain behaviour at the reinforcement level of slab I-150-A.

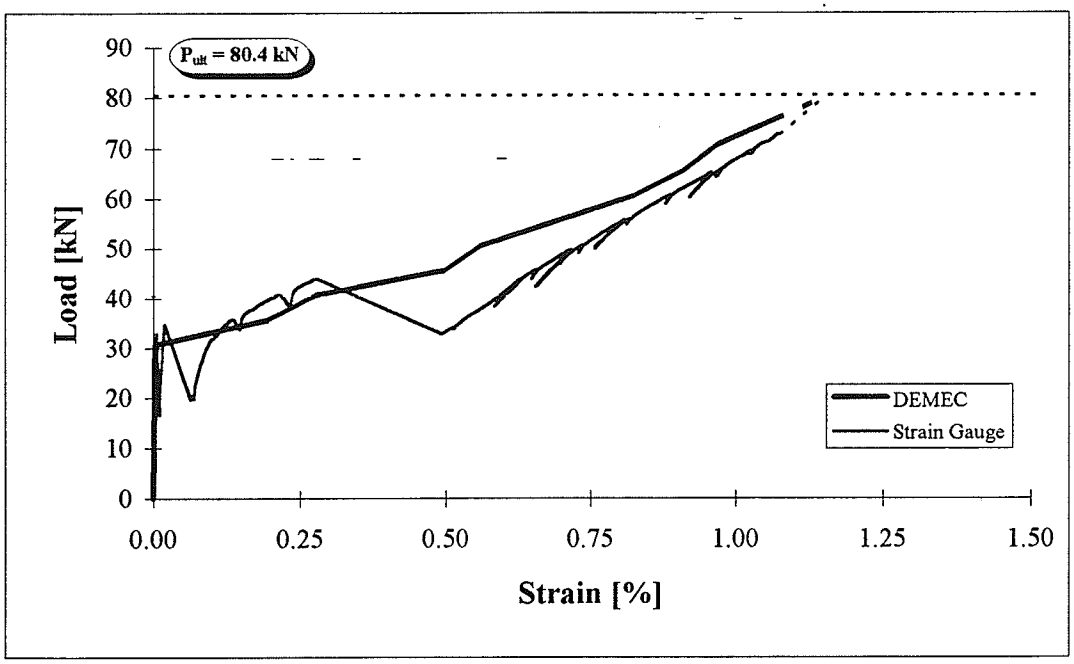

Figure 4.41: Load-tensile strain behaviour at the reinforcement level of slab I-150-B.

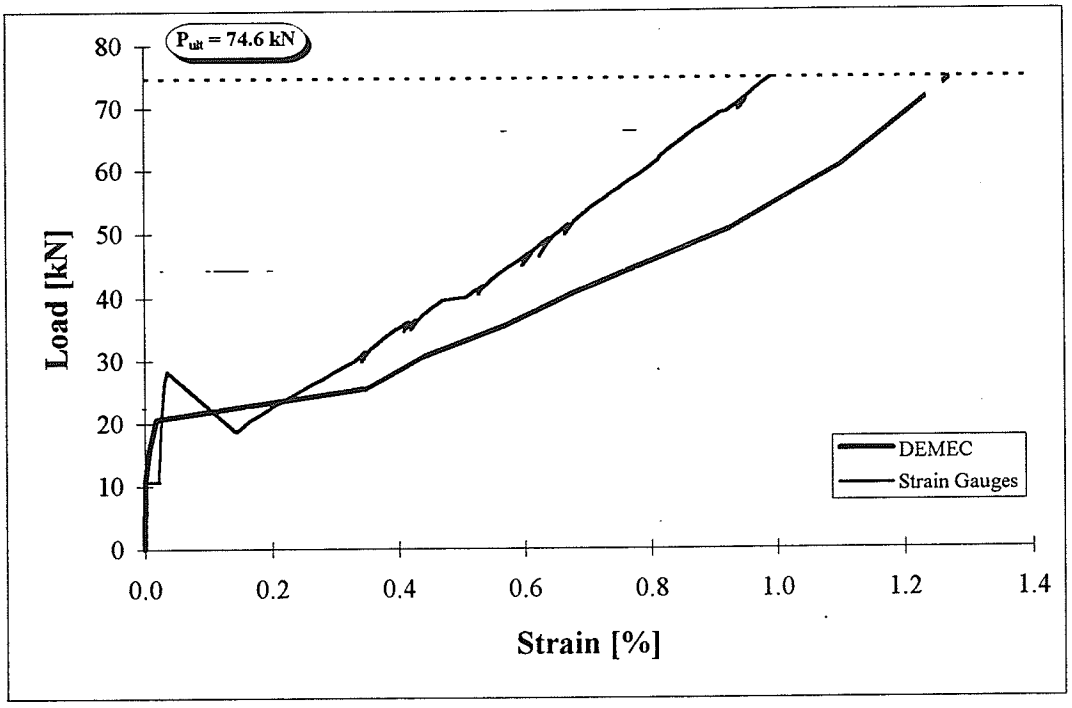

Figure 4.42: Load-tensile strain behaviour at the reinforcement level of slab I-150-C.

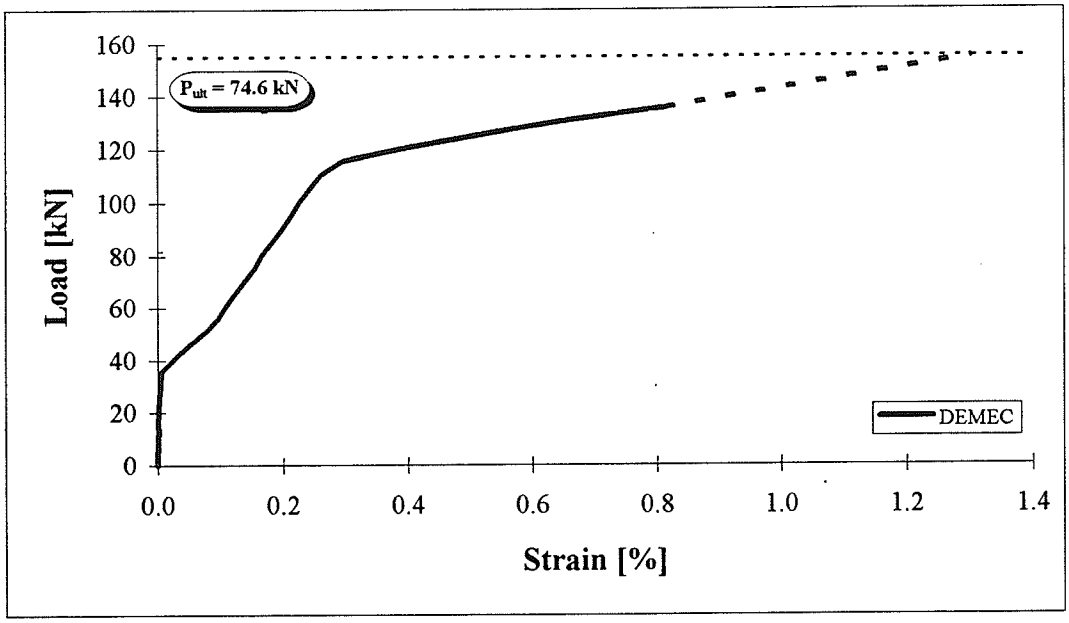

Figure 4.43: Load-tensile strain behaviour at the reinforcement level of slab S-150-T.

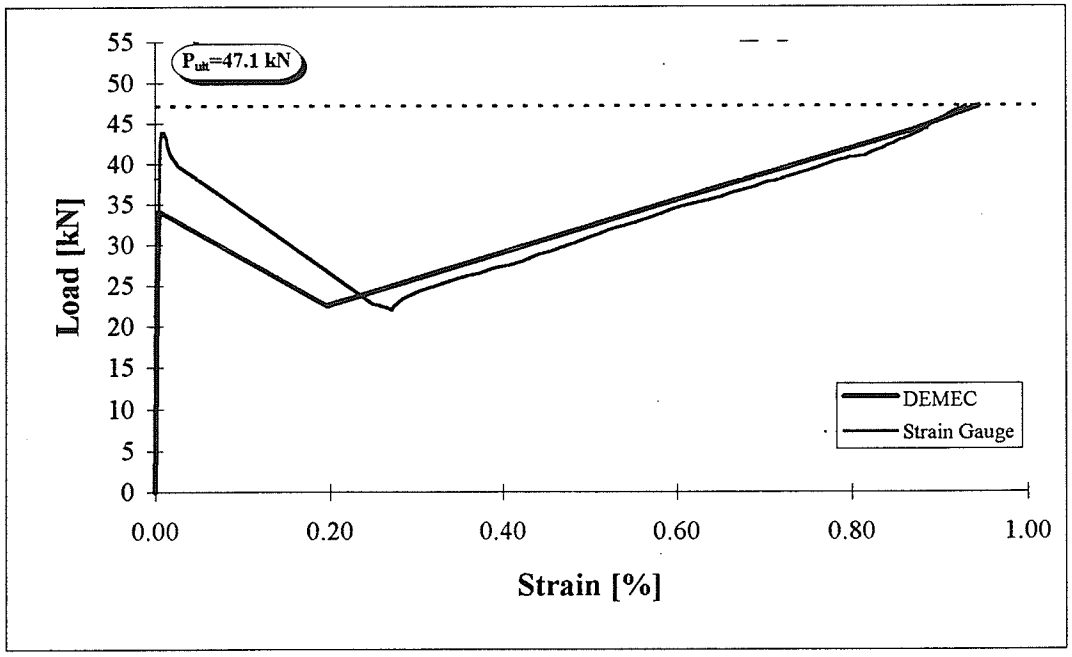

Figure 4.44: Load-tensile strain behaviour at the reinforcement level of slab I-200-A.

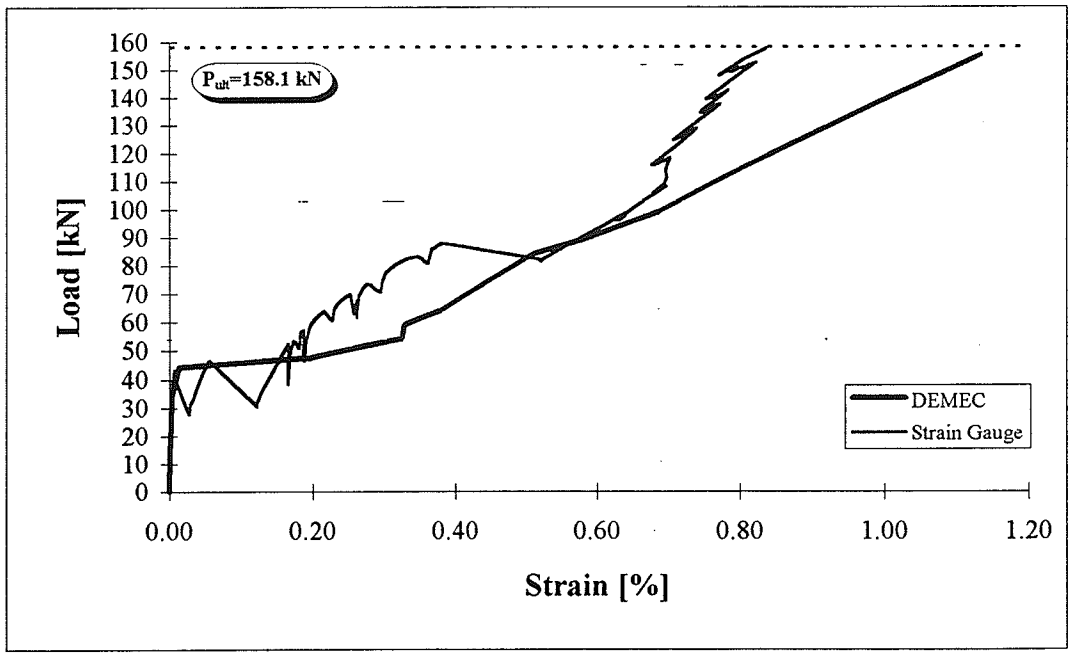

Figure 4.45: Load-tensile strain behaviour at the reinforcement level of slab I-200-C.

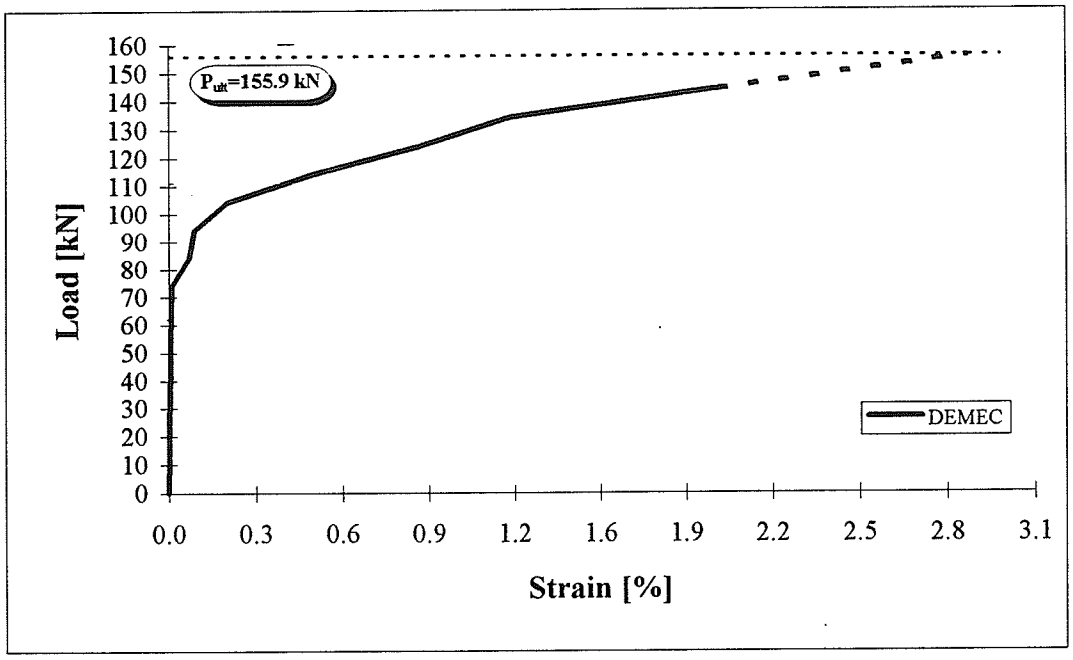

Figure 4.46: Load-tensile strain behaviour at the reinforcement level of slab S-200-T.

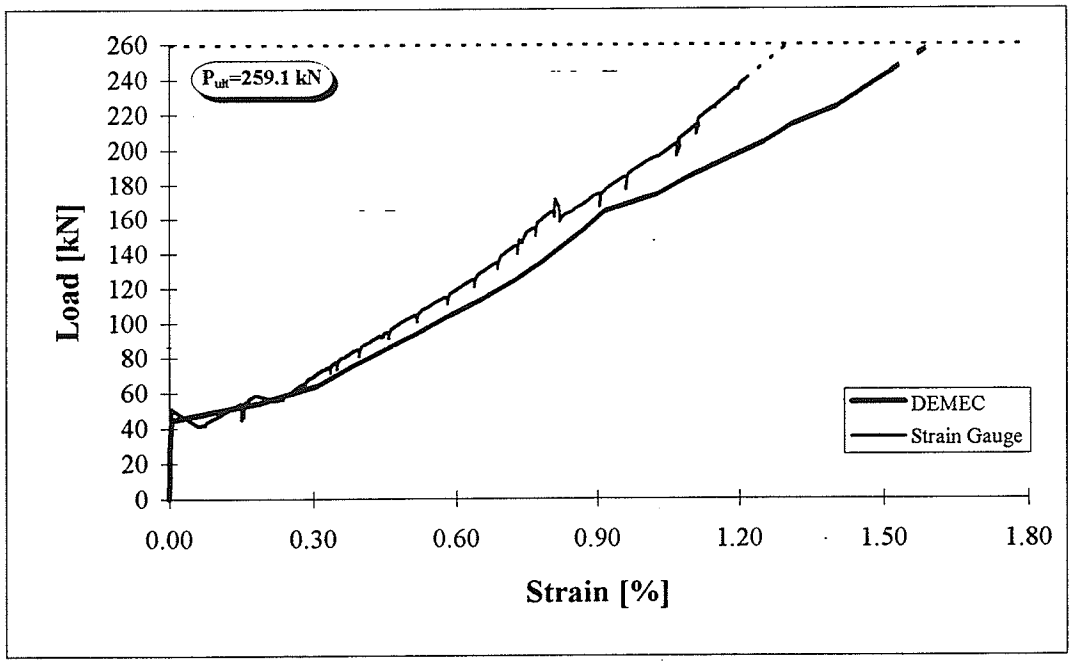

Figure 4.47: Load-tensile strain behaviour at the reinforcement level of slab LL-200-C.

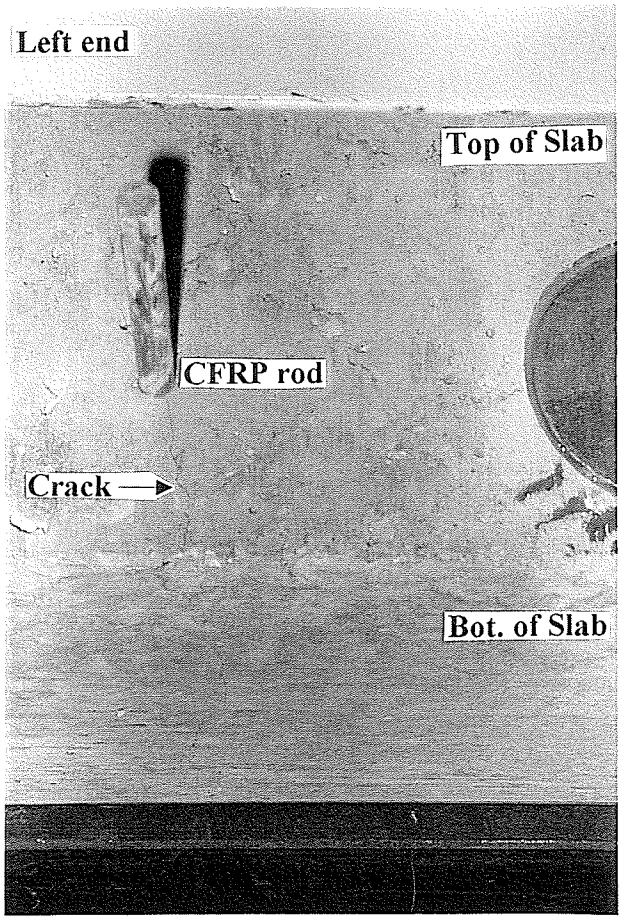

Figure 4.48: Bond cracks at left end of slab LL-200-C after failure.

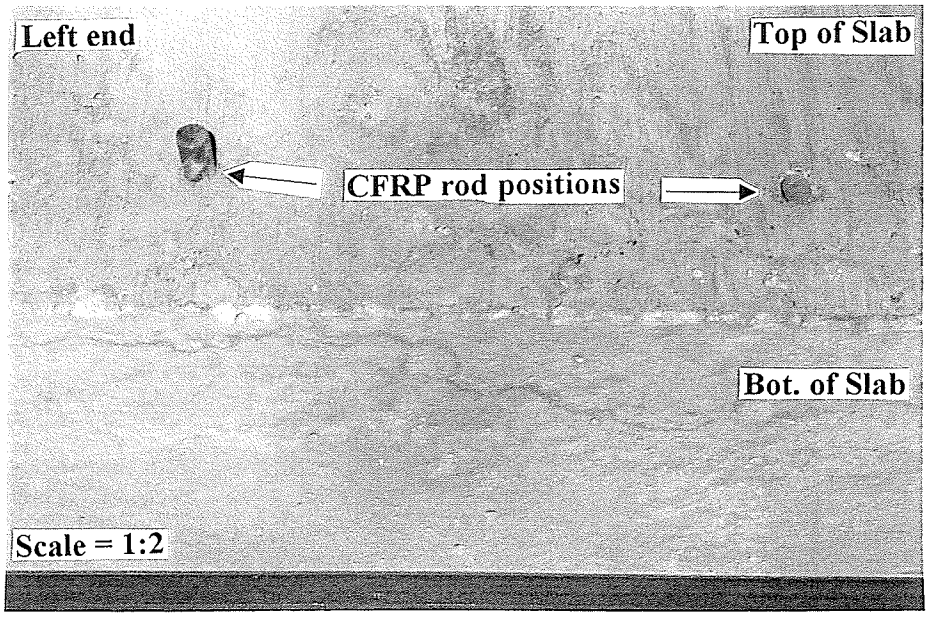

Figure 4.49: CFRP rod slippage at left end of slab LL-200-C.

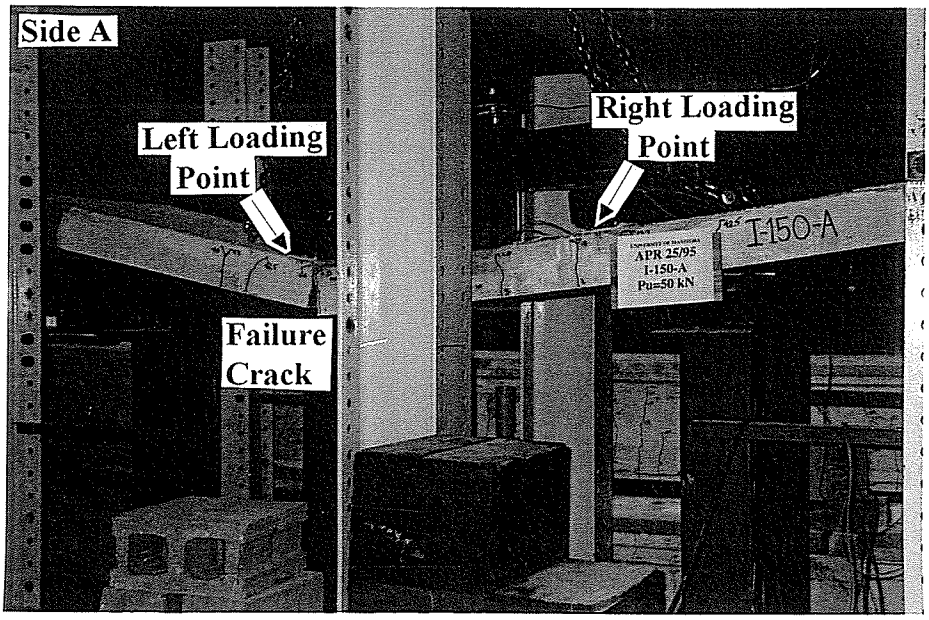

Figure 4.50: Failure position of slab I-150-A.

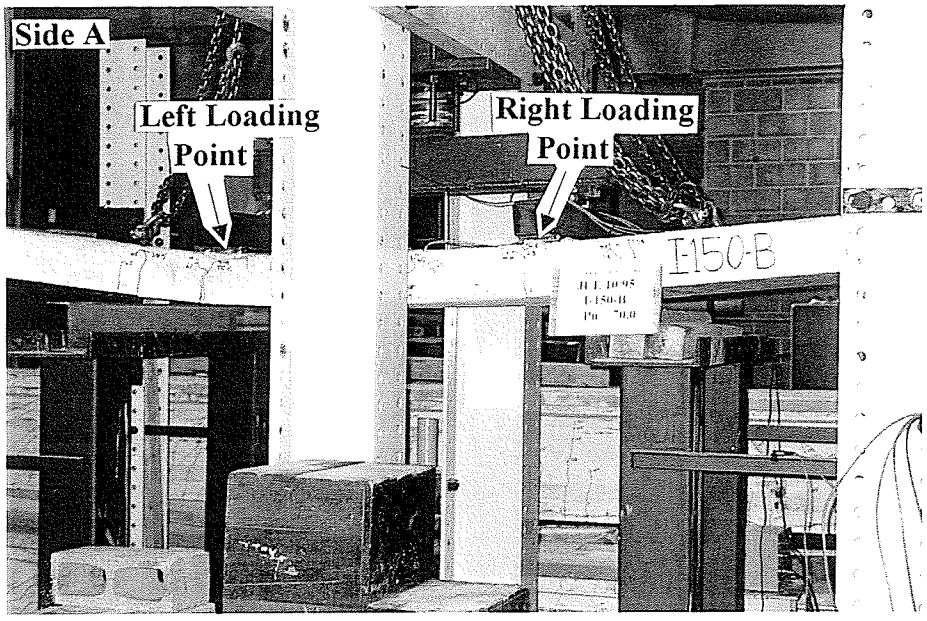

Figure 4.51: Failure position of slab I-150-B.

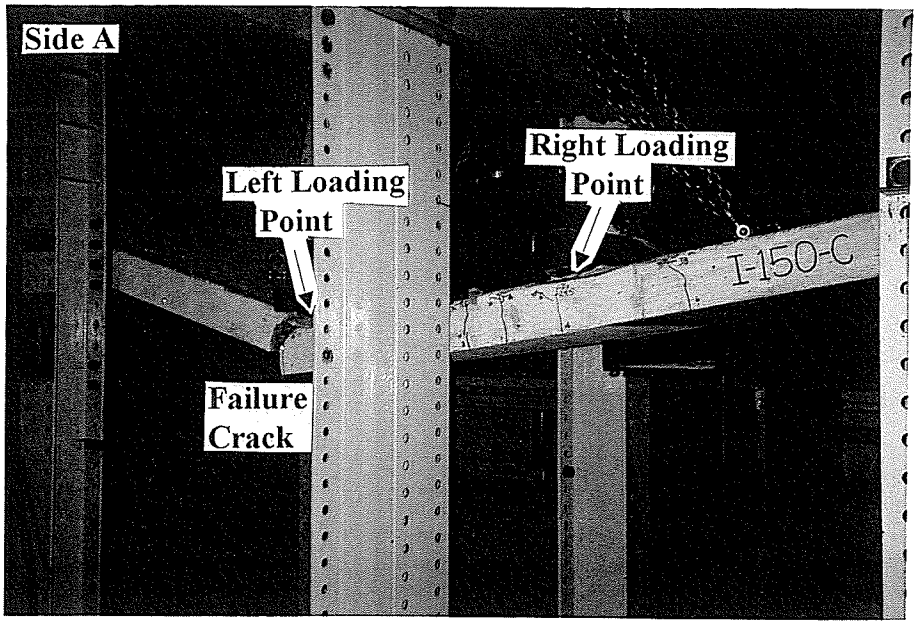

Figure 4.52: Failure position of slab I-150-C.

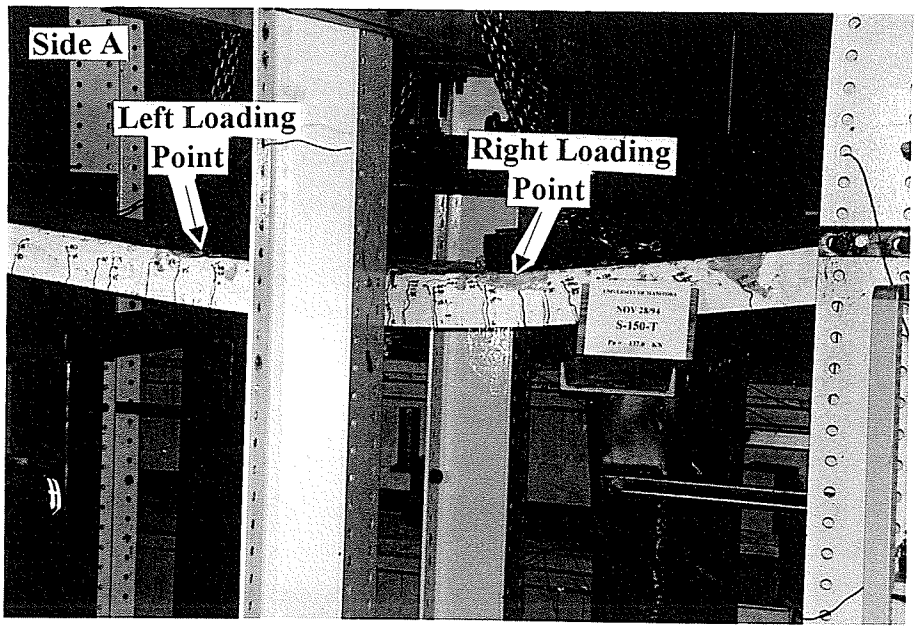

Figure 4.53: Failure position of slab S-150-T.

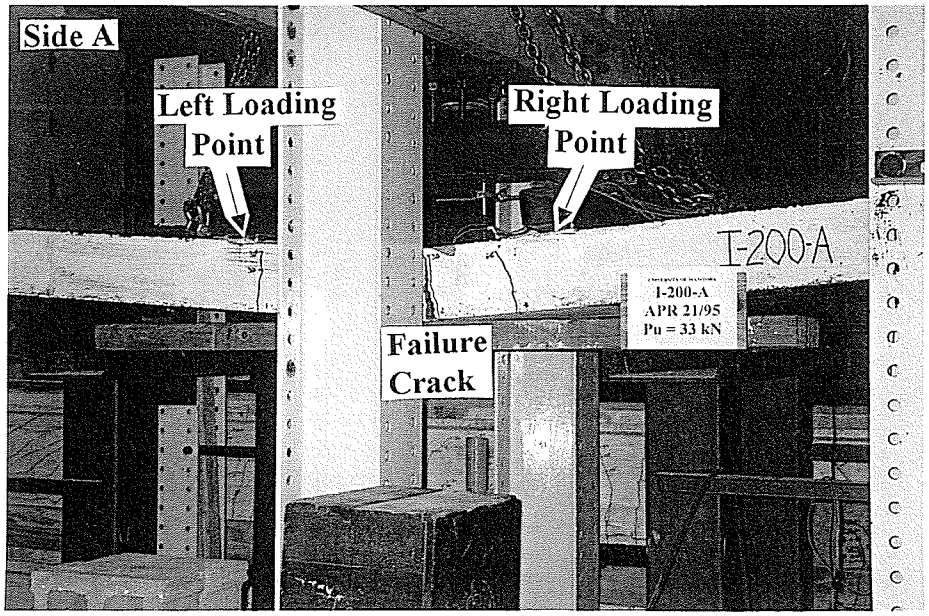

Figure 4.54: Failure position of slab I-200-A.

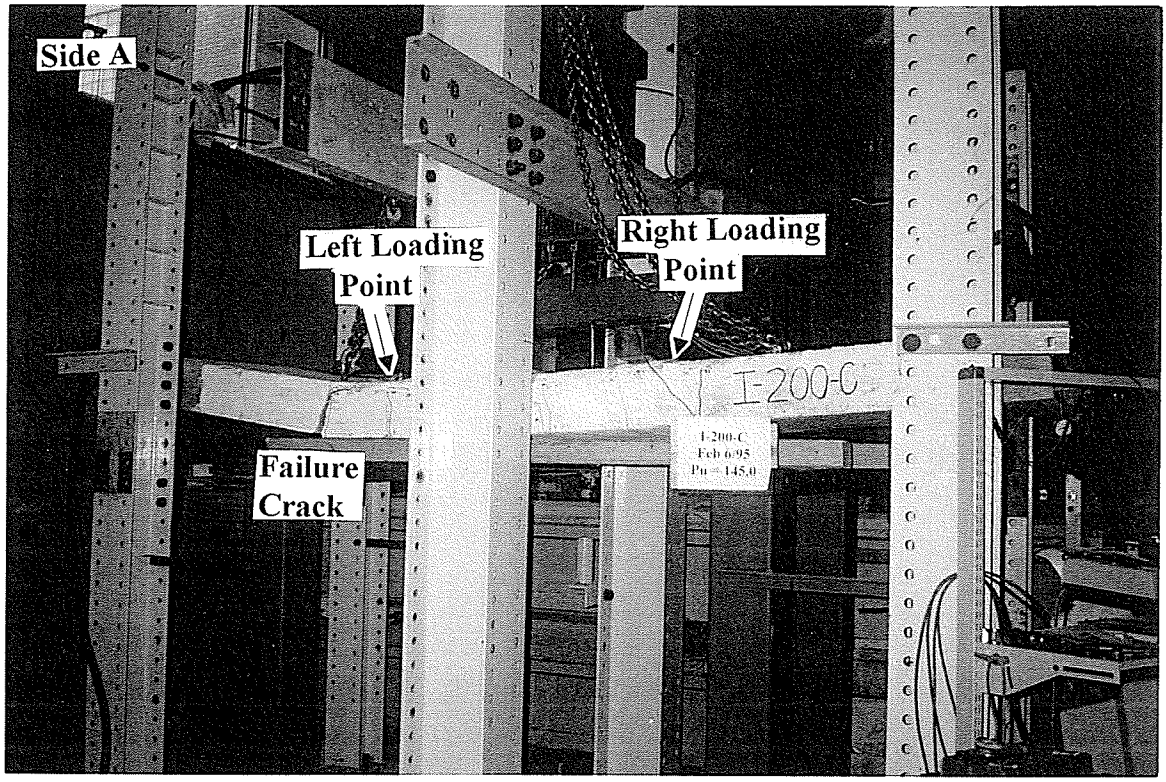

Figure 4.55: Failure position of slab I-200-C.

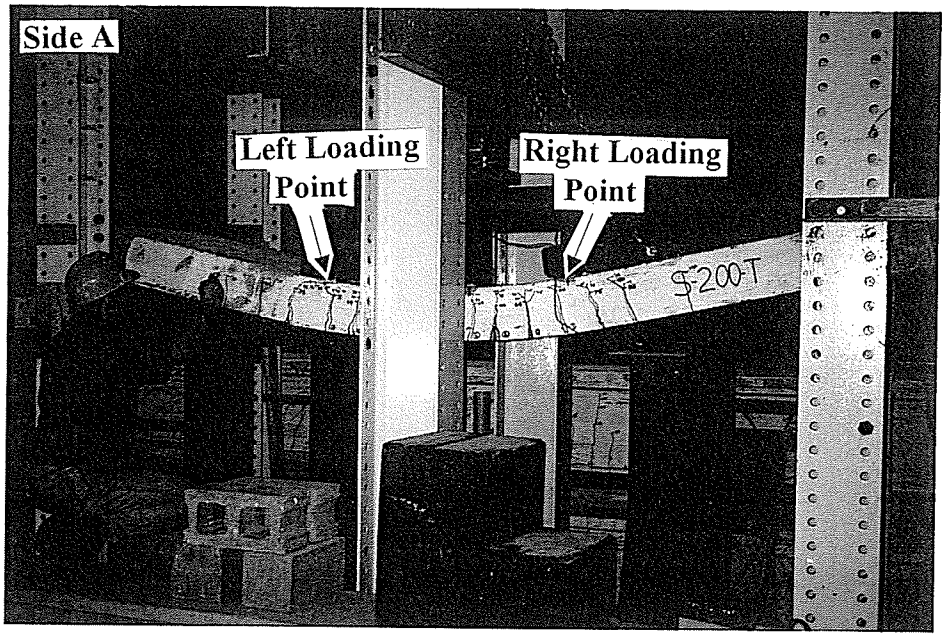

Figure 4.56: Failure position of slab S-200-T.

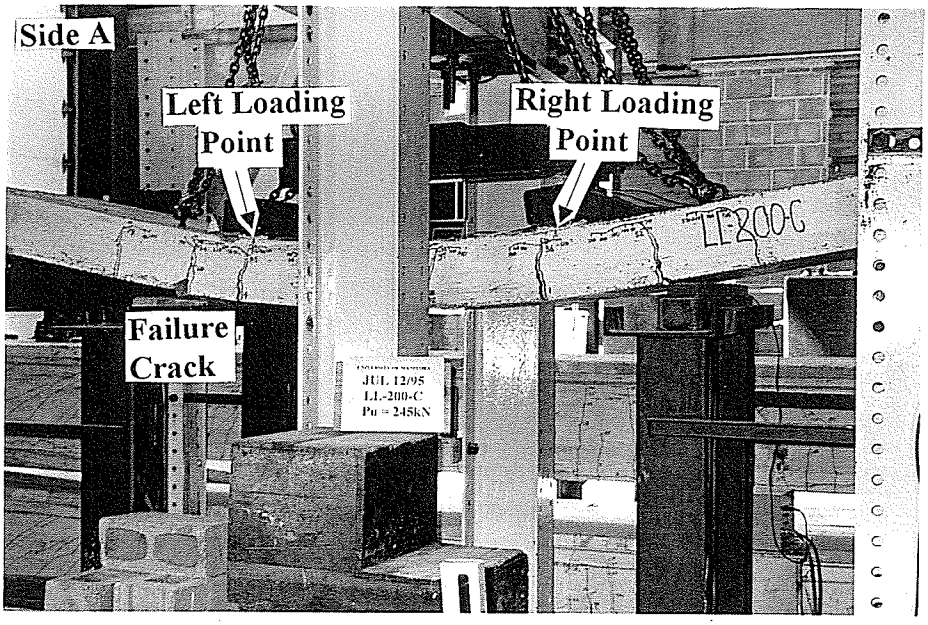

Figure 4.57: Failure position of slab LL-200-C.

CHAPTER 5

DISCUSSION OF EXPERIMENTAL RESULTS

5.0 GENERAL

In this chapter, the flexural behaviour of all eight slabs tested in this program is discussed. The observed experimental results, presented previously in Chapter 4, are used to describe the flexural behaviour, crack patterns and the modes of failure of all eight slabs. A comparison between the behaviours of the GFRP reinforced slabs, and the steel and CFRP reinforced slabs is also made.

5.1 FLEXURAL BEHAVIOUR

In general, all the ISOROD reinforced slabs exhibited linear behaviour prior to cracking, followed by sudden, wide and deep cracks, accompanied by large deflections. Test results and observed modes of failure for the slabs tested in this program are given

in Table 4.4. It should be noted that prior to failure of all the FRP reinforced slabs gave an ample warning effect through large deflections and extensive cracking.

The load-deflection behaviour of the 150 mm thick slabs reinforced by three reinforcement ratios of ISOROD and one slab reinforced by steel reinforcements, are shown in Figure 5.1. In comparison to the slab reinforced by the same steel reinforcement ratio, the behaviour of the slab reinforced by ISOROD bars indicates a significant reduction in stiffness after the initiation of the first crack. This behaviour is attributed to the low elastic modulus of GFRP bars in comparison to steel reinforcements. This characteristic caused significantly large crack widths and depths for all slabs reinforced by ISOROD reinforcements. Since the slabs were tested under a stroke control condition, initiation of the cracks is reflected by large reductions in the load resistance, and consequently the obvious step-wise behaviour, shown in Figure 5.1, as the cracks develop. This behaviour is reflected by the large values, given in Table 4.4, of the average drop in the load resistance, ΔP, to the load corresponding to the initiation of the first crack, P_{cr}, for the slabs reinforced by ISOROD-GFRP bars, in comparison to the slabs reinforced by steel.

Slabs I-150-A and I-150-B failed due to rupture of the reinforcements. Slab I-150-C was designed to fail by crushing of the concrete. However, this slab failed prematurely due to the shear failure of the ISOROD-GFRP bars at the location of a major crack outside the constant moment zone, as shown in Figure 5.2. The steel

reinforced slab, S-150-T, behaved classically by reduction in the stiffness after the initiation of the first crack, yielding, reflected by the measured large deflections, and failure due to the crushing of the concrete in the compression zone at a location within the constant moment zone of the slab.

Based on the behaviour described above, the experimental program was revised to test only two 200 mm thick slabs reinforced by ISOROD-GFRP bars, slabs I-200-A and I-200-C. These slabs were designed to fail by rupture of the ISOROD-GFRP reinforcements and crushing of the concrete respectively. Along with the control slab reinforced by steel reinforcements, a fourth slab, 200 mm thick reinforced by CFRP reinforcements, was included into the program. The CFRP reinforced slab was originally designed to fail by crushing of the concrete, to observe if a premature shear failure, observed in the over-reinforced GFRP slabs, would occur.

The load-deflection behaviour of the two-200 mm thick slabs reinforced by ISOROD-GFRP, and the slab reinforced by steel are shown in Figure 5.3. Slab I-200-A failed by rupture of the ISOROD reinforcements. Slab I-200-C failed prematurely due to shear failure of the ISOROD-GFRP bars at the location of a major diagonal crack outside the constant moment zone, as shown in Figure 5.4. The steel reinforced slab, S-200-T, failed, as designed, by crushing of the concrete in the compression zone.

The load-deflection behaviour of three slabs reinforced by similar reinforcement ratios using GFRP, CFRP and steel reinforcements, are shown in Figure 5.5. The slab reinforced by Leadline reinforcements, LL-200-C, designed to fail by crushing of the concrete, failed due to slippage of the Leadline reinforcements at one end of the slab. The flexural bond strength of the Leadline reinforcement at failure is estimated to be 4.6 MPa, which is similar to the values measured by tests done at the University of Manitoba (Domenico et al 1996), and less than the flexural bond strength of steel reinforcements. However, the ultimate load was significantly higher than the other two slabs, due to the relatively high tensile strength of the CFRP rods in comparison to the GFRP and steel reinforcements, as given in Tables 3.2 and 3.3. The measured ultimate tensile stress in the Leadline rods during testing approached 3000 MPa, which is well above the guaranteed ultimate tensile strength value of 1950 MPa, as shown in Table 3.3, and used in the original design of the slab. These values are in agreement with measured values obtained in tests done at the University of Manitoba (Abdelrahman 1995). The higher stress levels account for the unexpected level of bond stresses achieved during testing, and thus, the unexpected failure of the Leadline reinforced slab due to slippage of the reinforcements.

5.2 CRACK PATTERNS

Crack patterns of the 150 mm thick slabs reinforced by ISOROD-GFRP and steel reinforcements are shown in Figure 4.13. Averaged measured first crack widths and spacings for all the slabs tested in this program are given in Table 5.1. Crack widths

were recorded, as explained in Chapter 3 and presented in Chapter 4, but in order to obtain the actual first crack widths at the cracking loads for each slab, a linear regression of the recorded crack widths, as shown in Figures 5.6 to 5.10, is performed. Although the crack widths for slabs I-150-B and I-200-A were not monitored through the use of a microscope, the first crack widths could still be obtained through the use of DEMEC point station readings at the level of reinforcements, and are presented in Table 5.1. Due to a malfunction in the load cell, slab I-150-C was cracked prior to testing at an unknown load. Therefore, the first crack width was estimated using the second crack that developed in slab (i.e. the first crack that developed during testing). Since there were insufficient crack width measurements using the microscope for slab I-150-C, the first crack width was also estimated using DEMEC point station readings at the level of reinforcements. The averaged first crack widths for the 150 mm thick slabs reinforced by ISOROD reinforcements were larger than 1.0 mm, which is significantly higher than the allowable value of 0.33 mm specified by the Canadian Design Code (CSA 1994). In Table 5.1, the averaged first crack widths, w_{1F}, of the tested ISOROD-GFRP reinforced slabs are compared to the first crack widths, w_{1s}, of the slabs of similar thickness and reinforced by steel. In comparing slabs I-150-C and S-150-T, which had similar reinforcement ratios, the large crack widths which developed in the ISOROD reinforced slab averaged almost 19 times those developed in the steel reinforced slab. The larger crack widths result in an average crack spacing of 242 mm for the 150 mm thick slabs reinforced by ISOROD reinforcements, which is 2.3 times that observed for the similar slab reinforced by steel reinforcements. Since no slip was observed at the two ends of

the slabs, the large spacing of the cracks is not only due to the low elastic modulus of the reinforcement material, but also reflects a loss of bond between the concrete and the ISOROD reinforcements between the cracks. This could be triggered by possible debonding of the outer spiral layer of the glass fibre wrapped around the core of the ISOROD reinforcements.

This debonding phenomenon was observed during testing of reinforced concrete tension specimens using ISOROD reinforcements at the University of Manitoba (Clegg and Markos 1995), as shown in Figure 5.11(a). These tension specimens consisted of a single ISOROD bar embedded in concrete subjected to axial load through two cantilever ends, as shown in Figure 5.11(b). Separation and breaking of the deformations from the ISOROD bar surface during tension tests was also reported by others (Malvar 1995).

Crack patterns of the 200 mm thick slabs reinforced with ISOROD-GFRP, steel and Leadline-CFRP reinforcements are shown in Figure 4.18. Similarly, the crack spacing for slabs reinforced with GFRP bars were significantly larger in comparison to slabs reinforced by CFRP and steel reinforcements. The average first crack widths for slabs I-200-A and I-200-C were 1.310 mm and 0.562 mm respectively, which exceed the allowable limit value of 0.33 mm specified by the Canadian Design Code (CSA 1994). The average first crack width for slab I-200-A is over 14 times those observed in the steel reinforced slab, S-200-T, which has a similar reinforcement ratio. Once again, this behaviour is obviously due to the low elastic modulus of ISOROD-GFRP in comparison

to the elastic modulus of the steel reinforcements. Cracks were observed developing outside the constant moment zone in all the slabs tested in this program except in slab I-200-A.

5.3 MODES OF FAILURE

5.3.1 GFRP Reinforced Slabs

Slabs I-200-A, I-150-B and I-150-A all failed by rupturing of the ISOROD bars within the constant moment zone. The measured strains in the ISOROD reinforcements at the level of the reinforcements were lower than the expected ultimate strain of ISOROD reinforcements, resulting in lower than predicted ultimate loads, as previously shown in Table 4.4. The load-strain behaviour for the strain at the level of reinforcements, measured using six DEMEC point stations and two electrical strain gauges per ISOROD bar within the constant moment zone, for these slabs is shown in Figures 4.44, 4.41 and 4.40 respectively. Failure by rupture of the ISOROD-GFRP reinforcements within the constant moment zone, at strain levels lower than the ultimate strain levels achieved in tension tests, suggests that a reduction in strength of the ISOROD bars occurred during testing. As previously mentioned, and shown in Table 4.4, at the cracking load, slabs reinforced with ISOROD-GFRP reinforcements displayed large, sudden and deep cracks, producing a large reduction in load resistance, ΔP. The sudden impact caused by the transfer of tensile forces from the concrete to the ISOROD-GFRP bars at the time of cracking, could create localized failure of the

the ISOROD-GFRP bars, impeding the ISOROD-GFRP reinforcements achieving the ultimate tensile strengths obtained during tension tests. Using strain compatibility and the measured ultimate loads, the percentage of the ultimate tensile stresses of the ISOROD bars achieved at the level of reinforcement during testing, $\sigma_{Fexp}/\sigma_{Fu}$, of slabs I-200-A, I-150-A and I-150-B were calculated to be 76.8%, 95.4% and 81.0%, respectively. In Figure 5.12, load-deflection curves with similar scales for the three aforementioned slabs are presented in ascending order with respect to their bar diameters and percentage of reinforcements. All three slabs exhibit fairly linear behaviour after the initiation of cracking, as shown by the load-deflection envelope in Figure 5.12. As the bar diameters are increased from 9.5 mm to 12.7 mm, Figure 5.12(a) and 5.12(b), the percentage of achieved tensile stresses at the level of reinforcements increases from 76.8% to 95.4% of the ultimate tensile stress. This results in a reduction of the step-wise behaviour in the corresponding load-deflection curves, suggesting a reduction in the amount of localized failure of individual fibers of the ISOROD-GFRP bars. In accordance to the percentage of ultimate tensile stress achieved, the observed ultimate loads are closer to the predicted ultimate loads for the slabs achieving a higher percentage of the ultimate tensile stress at the level of reinforcements, as shown in Table 4.4. When the ISOROD bar diameter is increased from 12.7 mm to 15.9 mm, in slabs I-200-A and I-150-A respectively, as shown in Figure 5.12(b) and 5.12(c), the achieved percentage of ultimate tensile stress at the level of reinforcements decreases from 95.4% to 81.0%. Unlike steel rebars, GFRP bars are made of thousands of layers of glass fibers. As shown in Figure 5.13, the actual stresses

due to interlaminate shear lag leads to the development of a central region of the GFRP bar which is virtually unstressed. Thus, decreasing the effective area of the GFRP reinforcement, and in turn, increasing the tensile stresses in the remaining fibers within the GFRP bar. Figure 5.12 suggests that increases in the ISOROD bar diameter above 12.7 mm results in a reduction of ISOROD-GFRP bar strength due to interlaminate shear lag, therefore, lower ultimate tensile stress levels are achieved in the larger diameter ISOROD-GFRP bars. This phenomenon was also observed during tension tests done by others (Malvar 1995) on GFRP bars, including ISOROD reinforcements.

These findings lead to the development of a proposed tensile force equation, based on Equation 1, which will account for the tensile behaviour of ISOROD-GFRP bars as reinforcement in concrete members.

$$T = \beta_1 \beta_2 A_F \sigma_{Fu} \quad [kN] \qquad \text{Eqn. 5.1}$$

The material factors, β_1 and β_2, account for the reductions in tensile strengths of the GFRP bars due to the diameter effect and the general behaviour of the specific type of GFRP bar while embedded in concrete. The material factor to account for the diameter effect, β_1, is based on the reduction of stressed area of the GFRP bar due to interlaminate shear lag, and is determined by tension tests. The material factor to account for the general behaviour of the specific type of GFRP bar (i.e. ISOROD), β_2, depends on the reinforcement ratio, and is based on the manufacturing process of the bar, the type of resins used, the type of deformations and the bond strength of the GFRP

bar. Determination of material factor β_2 is achieved by bending tests of the specific GFRP bar in concrete specimens.

Due to the 25% reduction in ultimate tensile strength observed in slab I-200-A, which had a reinforcement ratio of 0.230%, further testing should be done to obtain a minimum reinforcement ratio for GFRP reinforced concrete members, ρ_{Fmin}, based on flexural design conditions.

The two ISOROD reinforced slabs originally designed to fail by crushing of the concrete, I-150-C and I-200-C, failed prematurely by shear of the ISOROD-GFRP bars at the location of a major crack in the flexural-shear zone. These failures were deemed premature, since the measured ultimate shear loads of 37.3 kN and 79.1 kN for slabs I-150-C and I-200-C respectively, are significantly lower than shear capacities predicted by the Canadian Design Code (CSA 1994). The Canadian Design Code equation, based on Equation 2, predicts shear capacities of 169.0 kN and 250.2 kN respectively.

CSA CAN3-A23.3-M94 [SI]:

$$V_c = 0.2\sqrt{f_c'}\,b_w d \qquad [N] \qquad \text{Eqn. 5.2}$$

The diagonal shear cracks for both specimens, shown in Figures 5.2 and 5.4, were significantly wide and deep. Failure occurred due to rupture of the ISOROD-GFRP bars at the location of the cracks due to dowel action, as shown in Figure 5.14. The

measured crack widths, in both slabs, prior to failure was approximately 15 mm, and extended vertically almost the entire depth of the slab, leaving a compression zone depth of approximately 15 mm. The large width and depth of the cracks virtually eliminates any shear resistance that could be provided along the cracks due to aggregate interlocking and allows for only a very small shear resistance within the reduced compression zone. As a result, the remaining shear resistance was provided mainly by the dowel action of the ISOROD bars across the cracks, causing the premature failure described.

The dowel strength of the ISOROD reinforcements is estimated to range from 7.5% to 13.8% of the ultimate tensile strength, based on the experimental results of slabs I-150-C and I-200-C. This range of dowel strength agrees with the value of 8.7% of the ultimate tensile strength, obtained for the dowel strength of ISOROD bars at the University of Manitoba (Grieef 1996).

Further comparisons of the measured ultimate shear loads of slabs I-150-C and I-200-C can be made with respect to the shear capacity equations from the ACI Design Code (ACI 1990), based on Equations 5.3 and 5.4, the Japanese Society of Civil Engineers (JSCE) Design Code 1984 (JSCE 1984), based on Equation 5.5, the recommendation by Machida (1996) for the JSCE 1996 Design Code, based on Equation 5.6, and the Comité Euro-International du Béton and Fédération Internationale

de la Précontrainte (CEB-FIP) Design Code (CEB-FIP 1978), based on Equation 5.7, and are presented as the unmodified equations in Figures 5.15 and 5.16.

ACI Clause 11.3.2.1 [SI]:

$$V_c = \left(\frac{\sqrt{f_c'} + 120\rho \left(\frac{V_u d}{M_u} \right)}{7} \right) b_w d \le 0.3\sqrt{f_c'} b_w d \qquad [N] \qquad \text{Eqn. 5.3}$$

$$\text{where:} \qquad \frac{V_u d}{M_u} = d/a$$

ACI Clause 11.3.1.1[SI]:

$$V_c = \left(\frac{\sqrt{f_c'}}{6} \right) b_w d \qquad [N] \qquad \text{Eqn. 5.4}$$

JSCE 1984 [SI]:

$$V_c = 0.94 f_c'^{1/3} \left(1 + \beta_d + \beta_\rho + \beta_n \right) b_w d \quad [kg] \qquad \text{Eqn. 5.5}$$

$$\text{where:} \quad \beta_d = \sqrt[4]{100/d} - 1 \ge 0 \qquad (d \text{ in } [cm])$$

$$\beta_\rho = \sqrt{100\rho} - 1 \le 0.73$$

$$\beta_n = M_o / M_d \le 1 \qquad (M_o = \text{decompression moment}$$

$$M_d = \text{applied moment at section})$$

$$f_c' \quad [kg/cm^2]$$

Machida (JSCE 1996) [SI]:

$$V_c = 0.9\beta_d\beta_\rho\beta_n f_c'^{1/3} b_w d \quad [kg] \qquad \text{Eqn. 5.6}$$

where: $\beta_d = \sqrt[4]{100/d} \le 1.5$ (d in [cm])

$\beta_\rho = \sqrt[3]{100\rho} \le 1.5$

$\beta_n = 1 + M_o/M_d \le 2.0$ (M_o = decompression moment

M_d = applied moment at section)

f_c' $[kg/cm^2]$

CEB-FIP [SI]:

$$V_c = \tau_{Rd}\kappa(1+50\rho)b_w d \qquad [N] \qquad \text{Eqn. 5.7}$$

where: $\tau_{Rd} = 0.00842(f_c' - 50) + 5 \qquad (for\ f_c' \ge 50\ MPa)$

$\kappa = 1.6 - d \ge 1.0 \qquad (d\ in\ [m])$

$\rho \ge 0.02$

Figures 5.15 and 5.16 show that all of the shear capacity equations drastically overestimate the shear capacities of slabs I-150-C and I-200-C. Due to the large difference in the elastic modulus values of GFRP reinforcements, E_F, and steel rebars, E_s, Equations 5.2 to 5.7 can be modified to include the ratio of the two elastic modulii, E_F/E_s.

The two proposed shear modification methods, using the E_F/E_s ratio applied to Equations 5.2 to 5.7, are explained and compared in the following sections.

5.3.1.1 Proposed Shear Modification Method 1

The shear capacity equation, V_c, is based on the shear strength contributions from the concrete in the compression zone, the aggregate interlock along the crack and the dowel action of the longitudinal reinforcement, as illustrated in Figure 5.17 (MacGregor 1988). Due to the low elastic modulus of GFRP, larger and deeper cracks develop in the GFRP reinforced concrete slabs in comparison to the steel reinforced concrete slabs. This results in a reduced compression zone and loss of aggregate interlock. Therefore, the first modification method, labeled Modified 1 on Figures 5.15 and 5.16, considers the E_F/E_s ratio as a multiplication factor to be applied to the entire shear capacity equations, Equations 5.2 to 5.7. This results in Equations 5.8 to 5.13.

CSA CAN3-A23.3-M94 (Modified 1) [SI]:

$$V_c = 0.2\left(\frac{E_F}{E_s}\right)\sqrt{f_c'}\,b_w d \qquad [N] \qquad \text{Eqn. 5.8}$$

ACI Clause 11.3.2.1 (Modified 1) [SI]:

$$V_c = \left(\frac{\sqrt{f_c'} + 120\rho\left(\frac{V_u d}{M_u}\right)}{7}\right)\left(\frac{E_F}{E_s}\right)b_w d \le 0.3\sqrt{f_c'}\,b_w d \qquad [N] \qquad \text{Eqn. 5.9}$$

ACI Clause 11.3.1.1 (Modified 1) [SI]:

$$V_c = \left(\frac{\sqrt{f_c'}}{6}\right)\left(\frac{E_F}{E_s}\right) b_w d \qquad [N] \qquad \text{Eqn. 5.10}$$

JSCE 1984 (Modified 1) [SI]:

$$V_c = 0.94 f_c'^{1/3}\left(1 + \beta_d + \beta_\rho + \beta_n\right)\left(\frac{E_F}{E_s}\right) b_w d \qquad [kg] \qquad \text{Eqn. 5.11}$$

Machida (JSCE 1996) (Modified 1) [SI]:

$$V_c = 0.9 \beta_d \beta_\rho \beta_n f_c'^{1/3}\left(\frac{E_F}{E_s}\right) b_w d \quad [kg] \qquad \text{Eqn. 5.12}$$

CEB-FIP (Modified 1) [SI]:

$$V_c = \tau_{Rd} \kappa (1 + 50\rho)\left(\frac{E_F}{E_s}\right) b_w d \qquad [N] \qquad \text{Eqn. 5.13}$$

5.3.1.2 Proposed Shear Modification Method 2

Proposed by Machida (1996), the second modification method, labeled Modified 2 on Figures 5.15 and 5.16, considers only the reduction in shear capacity due to the impact of the elastic modulus on the reinforcement ratio. Therefore, the multiplication factor of E_F/E_s is applied only to the reinforcement ratio, ρ, portion of the shear capacity equations, Equations 5.2 to 5.7, resulting in Equations 5.14 to 5.19.

CSA CAN3-A23.3-M94 (Modified 2) [SI]: (no change from Method 1)

$$V_c = 0.2\left(\frac{E_F}{E_s}\right)\sqrt{f_c'}\,b_w d \qquad [N] \qquad \text{Eqn. 5.14}$$

ACI Clause 11.3.2.1 (Modified 2) [SI]:

$$V_c = \left(\frac{\sqrt{f_c'} + 120\rho\left(\frac{V_u d}{M_u}\right)\left(\frac{E_F}{E_s}\right)}{7}\right) b_w d \le 0.3\sqrt{f_c'}\,b_w d \qquad [N] \qquad \text{Eqn. 5.15}$$

ACI Clause 11.3.1.1 (Modified 2) [SI]: (no change from Method 1)

$$V_c = \left(\frac{\sqrt{f_c'}}{6}\right)\left(\frac{E_F}{E_s}\right) b_w d \qquad [N] \qquad \text{Eqn. 5.16}$$

JSCE 1984 (Modified 2) [SI]:

$$V_c = 0.94 f_c'^{1/3}\left(1 + \beta_d + \beta_\rho + \beta_n\right) b_w d \qquad [kg] \qquad \text{Eqn. 5.17}$$

where: $\beta_\rho = \sqrt{100\rho\left(\frac{E_F}{E_s}\right)} - 1 \le 0.73$

Machida (JSCE 1996) (Modified 2) [SI]:

$$V_c = 0.9\beta_d\beta_\rho\beta_n f_c'^{1/3}\left(\frac{E_F}{E_s}\right)b_w d \quad [kg] \qquad \text{Eqn. 5.18}$$

$$\text{where:} \quad \beta_\rho = \sqrt[3]{100\rho\left(\frac{E_F}{E_s}\right)} \le 1.5$$

CEB-FIP (Modified 2) [SI]:

$$V_c = \tau_{Rd}\kappa\left(1 + 50\rho\left(\frac{E_F}{E_s}\right)\right)b_w d \qquad [N] \qquad \text{Eqn. 5.19}$$

5.3.1.3 Comparison of Proposed Shear Modifications

The measured ultimate shear loads were compared for slabs I-150-C and I-200-C with respect to their corresponding shear capacities using the modified equations, Equations 5.8 to 5.19, are also shown in Figures 5.15 and 5.16. The equations modified by method 1, Equations 5.8 to 5.13, more accurately predicted the shear capacities of slabs I-150-C and I-200-C, and in most cases conservatively, than the unmodified equations, Equations 5.2 to 5.7. The equations modified by method 2, proposed by Machida (1996) , Equations 5.14 to 5.19, improved the estimated shear capacity of the original design code equations, but remained drastically overestimated.

5.3.2 CFRP and Steel Reinforced Slabs

The slab reinforced by Leadline, originally designed to fail by crushing of the concrete, failed due to slippage of the bars at one end of the slab at a load level of 259.1 kN. Crushing of the concrete was ultimately achieved upon reloading the slab to a load level of 190.6 kN.

Slabs reinforced with steel rebars behaved classically by yielding of the rebars followed by crushing of the concrete.

5.4 FLEXURAL ANALYSIS PROCEDURE

The tested slabs were analyzed by the strain compatibility approach to predict the flexural response up to failure. Following common procedure, as described in many text books (Collins and Mitchell 1991), the analysis is based on the following assumptions:

1.) The concrete is subjected to axial strains only.

2.) The strains are uniform over the width of the section.

3.) The strains are linear over the depth of the section (i.e. plane section remains plane).

4.) Tension stiffening is ignored, due to the large crack widths which develop in FRP reinforced concrete members.

Due to the significant amount of calculations necessary to predict the full flexural response, the analysis procedure was completed using a computer program, according to the following steps:

1.) A strain at the extreme compression fibre of the concrete is assumed.

2.) A neutral axis depth is assumed.

3.) The internal forces in the compression and the tension zones, based on the tensile strains at the level of reinforcements, are determined, as shown in Figure 5.18.

4.) The equilibrium of the section is checked according to Equation 5.20.

$$\int_{A_c} f_c dA_c + \int_{A_F} f_F dA_F = 0 \qquad \text{Eqn. 5.20}$$

where:

f_c = *concrete stress in compression.*
A_c = *area of concrete.*
f_F = *stress in FRP.*
A_F = *area of FRP reinforcements.*

5.) The assumption of the neutral axis depth is revised until equilibrium is satisfied.

6.) The internal moment of the section, based on Equation 5.21, is calculated.

$$\int_{A_c} f_c \, y \, dA_c + \int_{A_F} f_F \, y \, dA_F = M \qquad \text{Eqn. 5.21}$$

where:

y = *distance, measured from the neutral axis.*
M = *bending moment.*

7.) The concrete strain in the extreme compression fibres is increased, and steps 2 to 6 are repeated.

8.) The moment-curvature relationship is calculated, ignoring the tension stiffening at every strain increment, based on Equation 5.22.

$$\Phi = \frac{\varepsilon_c}{c} \qquad \text{Eqn. 5.22}$$

where:

Φ = *curvature at a given strain increment.*
ε_c = *concrete strain at the extreme compression fibres.*
c = *neutral axis depth from the extreme compression fibres.*

5.4.1 Cracking Moment Calculation

The cracking moment was calculated based on Equation 5.23.

$$M_{cr} = \frac{f_R I_g}{y_b} \qquad \text{Eqn. 5.23}$$

where:

M_{cr} = *cracking moment*
f_R = *rupture strength of concrete.*
I_g = *moment of inertia based on gross sec tional properties.*
y_b = *neutral axis depth from tension side.*

5.4.2 Failure Criteria

As with steel reinforced one-way concrete slabs, the three modes of failure of GFRP and CFRP reinforced concrete one-way slabs are: rupture of the reinforcements; crushing of the concrete and; simultaneous rupture of the reinforcements and crushing of the concrete. Therefore, the failure modes of the slabs are dependent on the strains in the extreme compression fibres and at the level of the reinforcements. Rupture of the FRP reinforcements occurs when the strains at the level of the reinforcements reach the ultimate tensile strains, as presented in Tables 3.2 and 3.3 for the ISOROD-GFRP and Leadline-CFRP reinforcements, while the strain in the extreme compression fibres remains below the ultimate compression strain value for concrete. Crushing of the concrete occurs when the extreme compression fibres in the slab reach the ultimate concrete compression strain value, while the strains in the FRP reinforcements remain in the elastic range. Simultaneous rupture of the FRP reinforcements and crushing of the concrete occurs when the strains at the level of reinforcements and the extreme

compression fibres reach the ultimate tensile and compression values, respectively, at the same time.

5.5 MATERIAL MODELING

The four materials used in the study were concrete, ISOROD-GFRP bars, Leadline-CFRP rods and steel rebars. Modeling of the materials was based on measured values from the control specimens and the analytical models based on the available literature.

5.5.1 Concrete

The stress-strain relationship of the concrete was modeled based on a parabolic relationship, as shown in Figure 5.19. Through the use of stress-block factors α_1 and β_1, introduced by Collins and Mitchell (1991), the actual non-linear stress distributions can be simplified to equivalent uniform stress distributions. The determination of the stress-block factors α_1 and β_1 are made so that the magnitude and location of the resultant forces, for a given compressive stress distribution, are the same in the equivalent uniform stress distribution as in the actual distribution, by using the integrals based on Equations 5.24 and 5.25.

$$\int_0^c f_c \, b \, dy = \alpha_1 \, f_c' \beta_1 \, c \, b \qquad \text{Eqn. 5.24}$$

$$\bar{y} = \frac{\int_0^c f_c\, b\, y\, dy}{\int_0^c f_c\, b\, dy} = c - 0.5\beta_1 c \qquad \text{Eqn. 5.25}$$

Further simplifications are made for these integrals for a parabolic stress-strain curve and a constant width, resulting in Equations 5.26 and 5.27.

$$\alpha_1\beta_1 = \frac{\varepsilon_c}{\varepsilon'_c} - \frac{1}{3}\left(\frac{\varepsilon_c}{\varepsilon'_c}\right)^2 \qquad \text{Eqn. 5.26}$$

$$\beta_1 = \frac{4 - \varepsilon_c/\varepsilon'_c}{6 - 2\varepsilon_c/\varepsilon'_c} \qquad \text{Eqn. 5.27}$$

where:

ε_c = *concrete strain for a given loading condition.*
ε'_c = *concrete strain corresponding to the max imum stress.*

The concrete strain corresponding to the maximum stress, ε'_c, obtained during concrete cylinder tests, as given in Table 3.1, can also be calculated using an equation introduced by Park and Paulay (1975), based on Equation 5.28.

$$\varepsilon'_c = \frac{2f'_c}{E_c} \qquad \text{Eqn. 5.28}$$

The rupture strength of concrete was assumed according to the Canadian Design Code (CSA 1994), based on Equation 5.29.

$$f_R = 0.6\sqrt{f_c'} \qquad \text{Eqn. 5.29}$$

The concrete strength in tension was neglected after the initiation of cracking.

5.5.2 ISOROD-GFRP Bars

The stress-strain behaviour of the ISOROD-GFRP bars is assumed to be elastically linear up to failure. Based on strengths reported by Chaallal and Benmokrane (1993), the ultimate tensile strength, strain and elastic modulus values of 690 MPa, 1.767% and 41.3 GPa were used. It should be noted that based on tests done at the University of Manitoba (Grieef 1996), the ultimate tensile strains and elastic modulus values were observed to be 1.414% and 45 GPa.

5.5.3 Leadline-CFRP Rods

The stress-strain behaviour of the Leadline-CFRP rods is assumed to be elastically linear up to failure. The manufacturing company reported guaranteed values of 1950 MPa, 1.3% and 147 GPa for the ultimate tensile strength, strain and elastic modulus respectively. These values were used for analysis purposes. However, tests done at the University of Manitoba (Abdelrahman 1995) have found that the ultimate

tensile strength could be as high as 2950 MPa and the ultimate tensile strain could reach as high as 2.0%. The values reported by the University of Manitoba (Abdelrahman 1995) produced more accurate results with respect to the observed flexural response of the tested slab reinforced by Leadline-CFRP rods.

5.5.4 Steel Rebars

The tensile properties of the 10M and 15M steel rebars were based on tension tests, as explained in Chapter 2, and are given in Chapter 4. The yield strength and strain used in analysis were 435 MPa and 0.25% respectively. An elastic modulus value of 177 GPa was also used based on these tension tests. A rupture strain of 8.0% at a strength of 700 MPa was used for the ultimate rupture strengths.

5.6 DEFLECTION PREDICTION

The deflection was calculated using integration of the curvature at many sections along the slab span, and without accounting for the tension stiffening. The curvature was calculated using the strain compatibility, as described in previous sections. The self-weight of the slabs was also accounted for in the final calculation of the midspan deflections.

The moment-curvature relationship is calculated for every slab without accounting for the tension stiffening. For each load increment, the curvature at different sections along the entire length of the slab is determined up to failure load using a

computer program. The deflection is determined by integration of the curvature from the support to the midspan section to obtain the maximum deflection due to the specified load. The curvature integration was performed numerically using Equation 5.30, as illustrated in Figure 5.20.

$$\Delta = \Sigma \frac{\Phi_i x_i + \Phi_{i+1} x_{i+1}}{2} \Delta x_i \qquad \text{Eqn. 5.30}$$

For this project, the integration was performed for 40 sections along half the slab span.

The curvature was calculated without accounting for tension stiffening, based on the slope of the strain diagram obtained at each load increment, as described in previous sections.

Table 5.1: Crack widths and spacing

Slab	ρ %	w_{1F} or w_{1s} mm	w_{1F}/w_{1s}	s_{cF} mm	s_{cF}/s_{cs}
S-150-T	0.962	0.063	1.0	97	1.0
I-150-A	0.487	1.185	18.8	231	2.4
I-150-B	0.764	1.180	18.7	273	2.8
I-150-C	0.955	1.190	18.9	223	2.3
S-200-T	0.390	0.090	1.0	119	1.0
I-200-A	0.230	1.310	14.6	283	2.4
I-200-C	0.774	0.562	6.2	236	2.0
LL-200-C	0.303	0.506	5.6	220	1.8

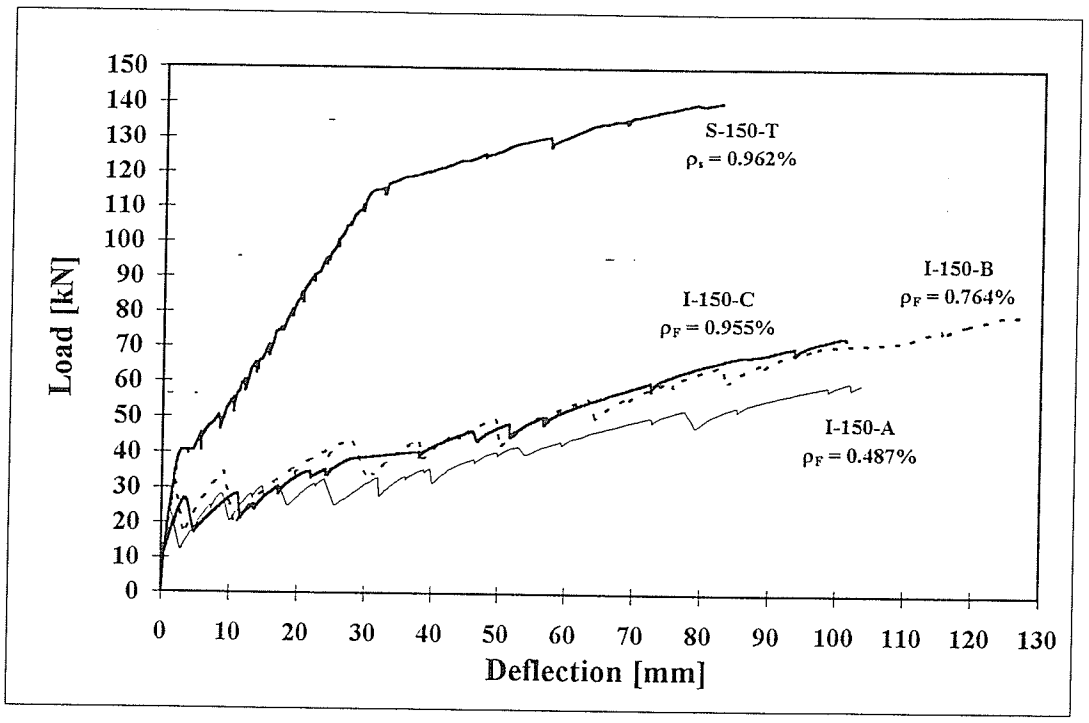

Figure 5.1: Midspan load-deflection diagram for the 150 mm thick slabs.

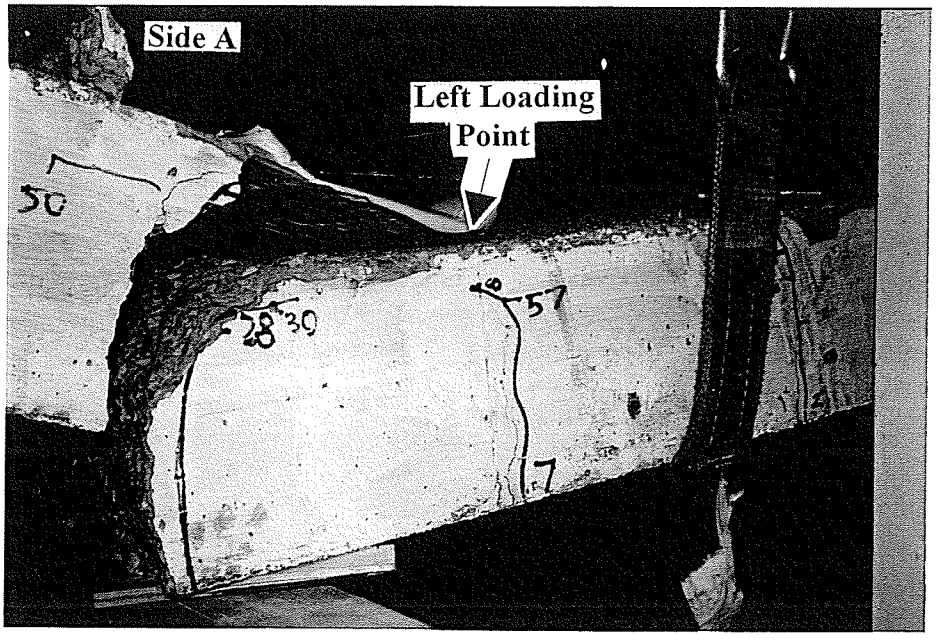

Figure 5.2: Failure crack at left end of slab I-150-C.

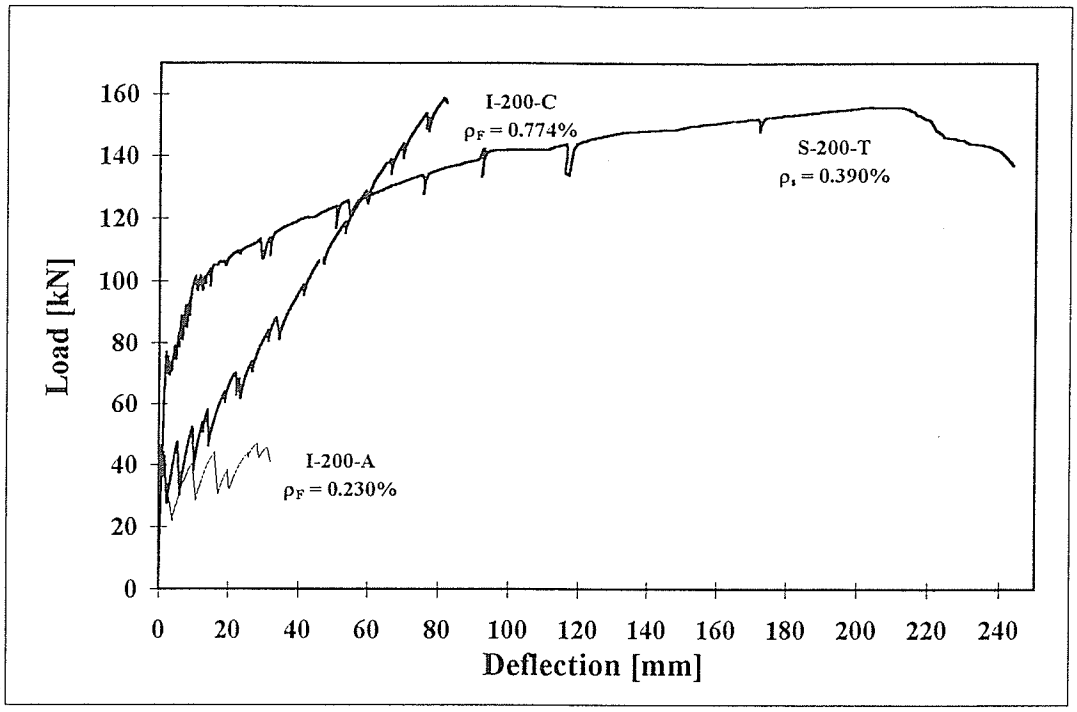

Figure 5.3: Midspan load-deflection diagram for 200 mm thick slabs reinforced by GFRP and steel reinforcements.

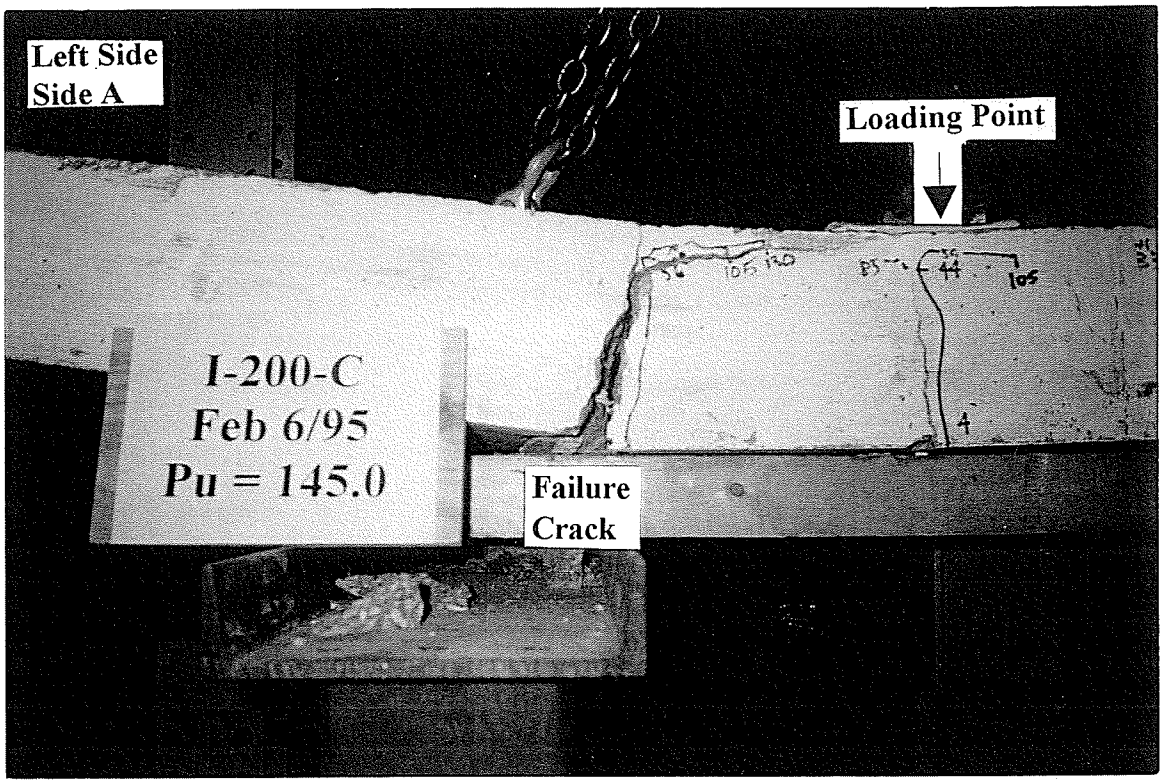

Figure 5.4: Failure crack at left end of slab I-200-C

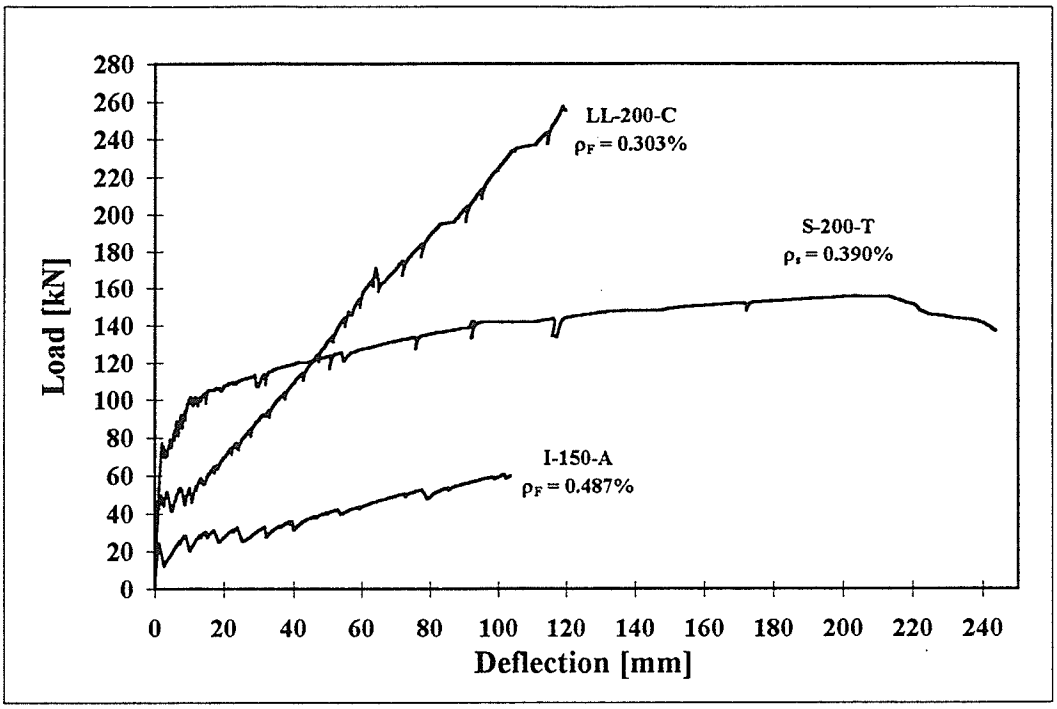

Figure 5.5: Midspan load-deflection diagram for slabs with similiar reinforcement ratios of GFRP,CFRP and steel reinforcements.

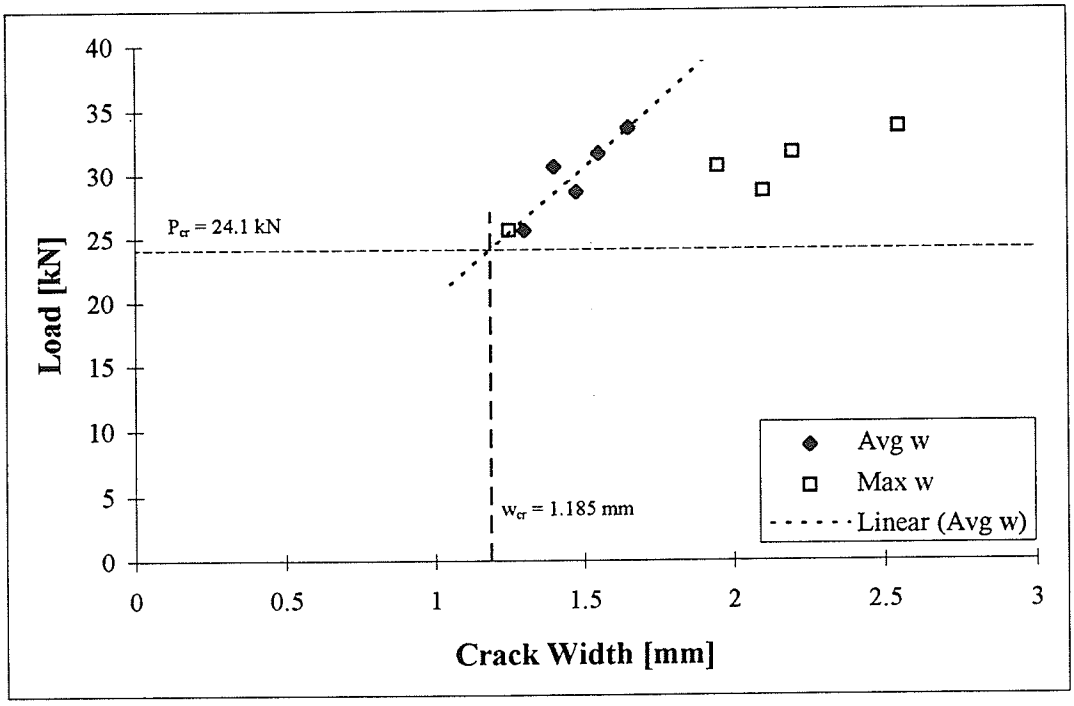

Figure 5.6: Average and maximum crack width measurements for slab I-150-A.

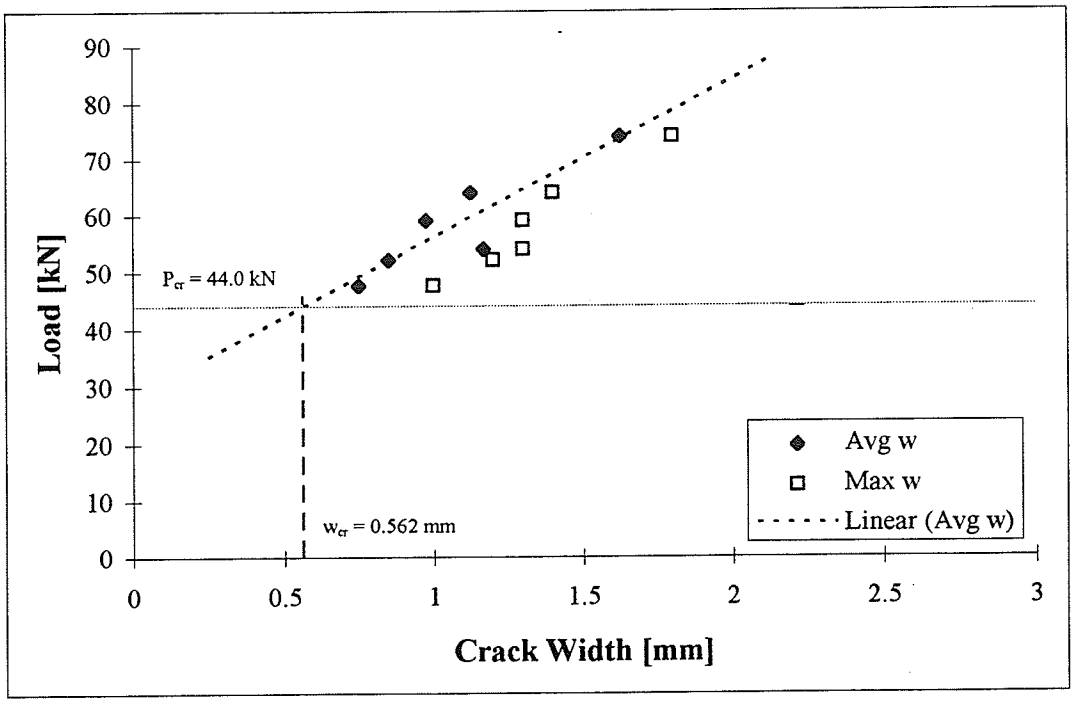

Figure 5.7: Average and maximum crack width measurements for slab I-200-C.

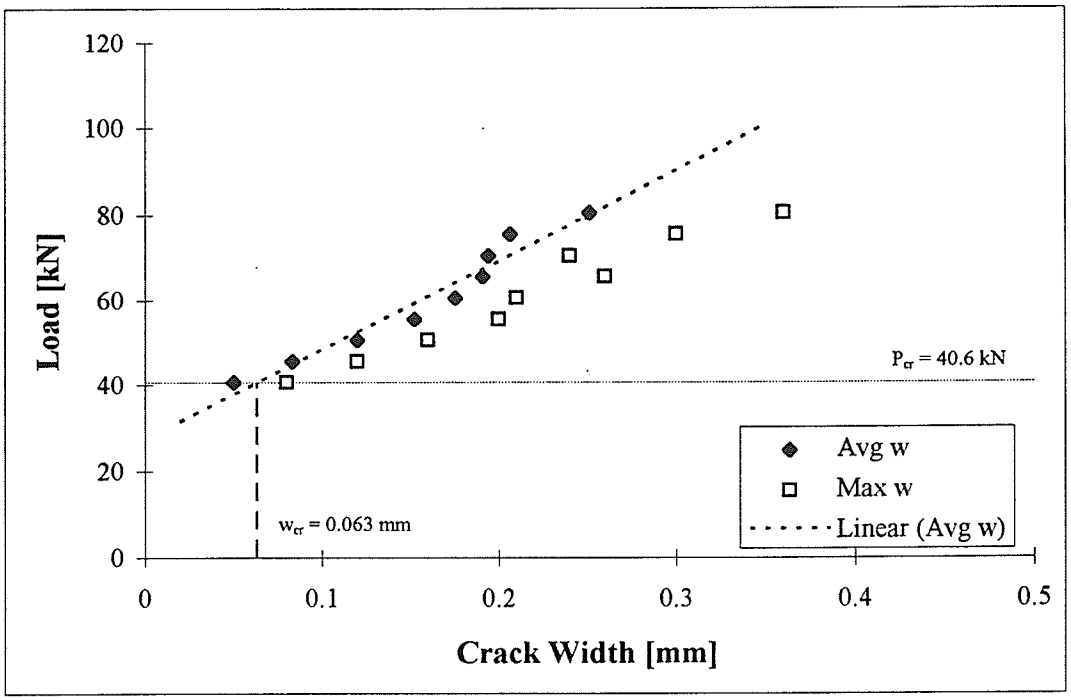

Figure 5.8: Average and maximum crack width measurements for slab S-150-T.

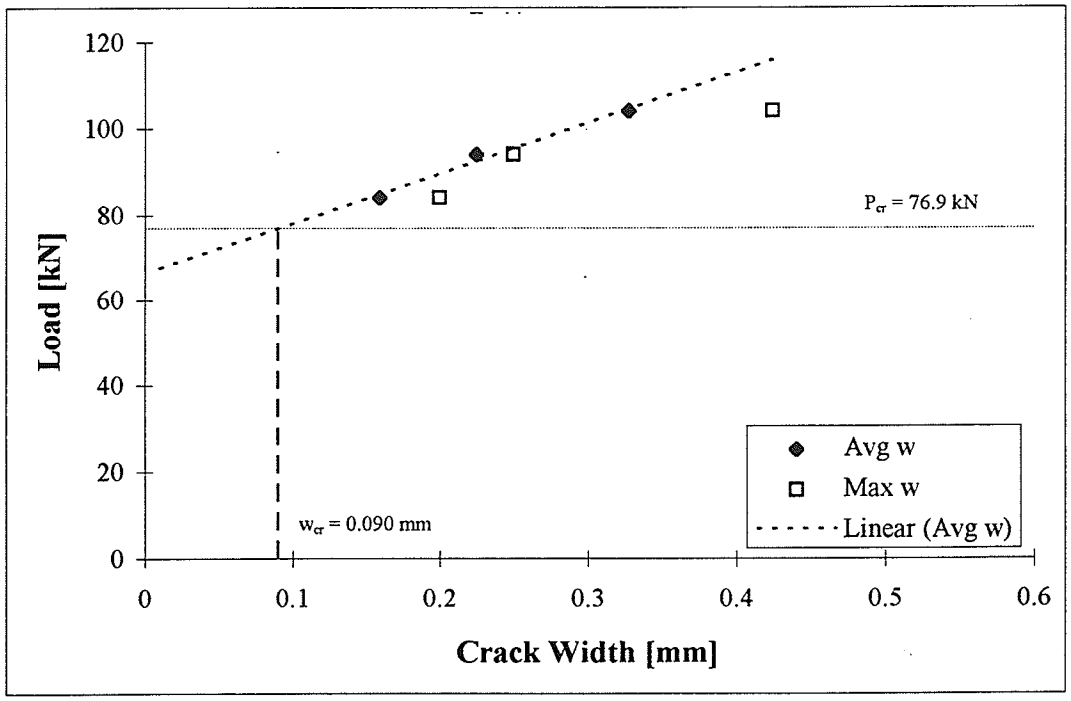

Figure 5.9: Average and maximum crack width measurements for slab S-200-T.

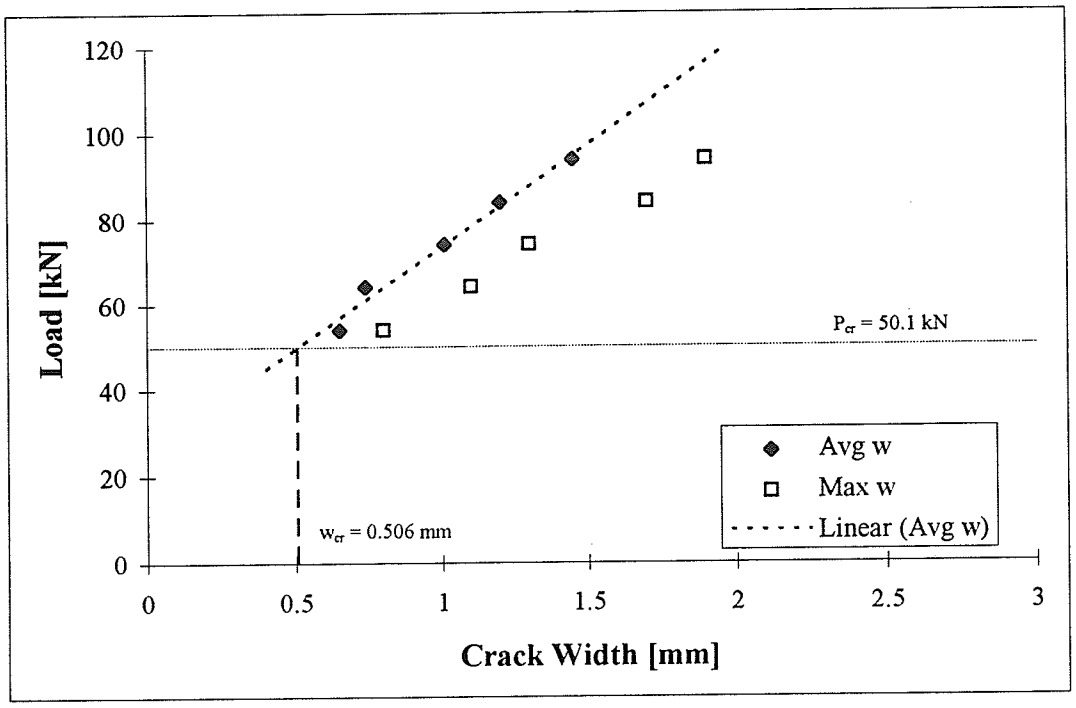

Figure 5.10: Average and maximum crack width measurements for slab LL-200-C.

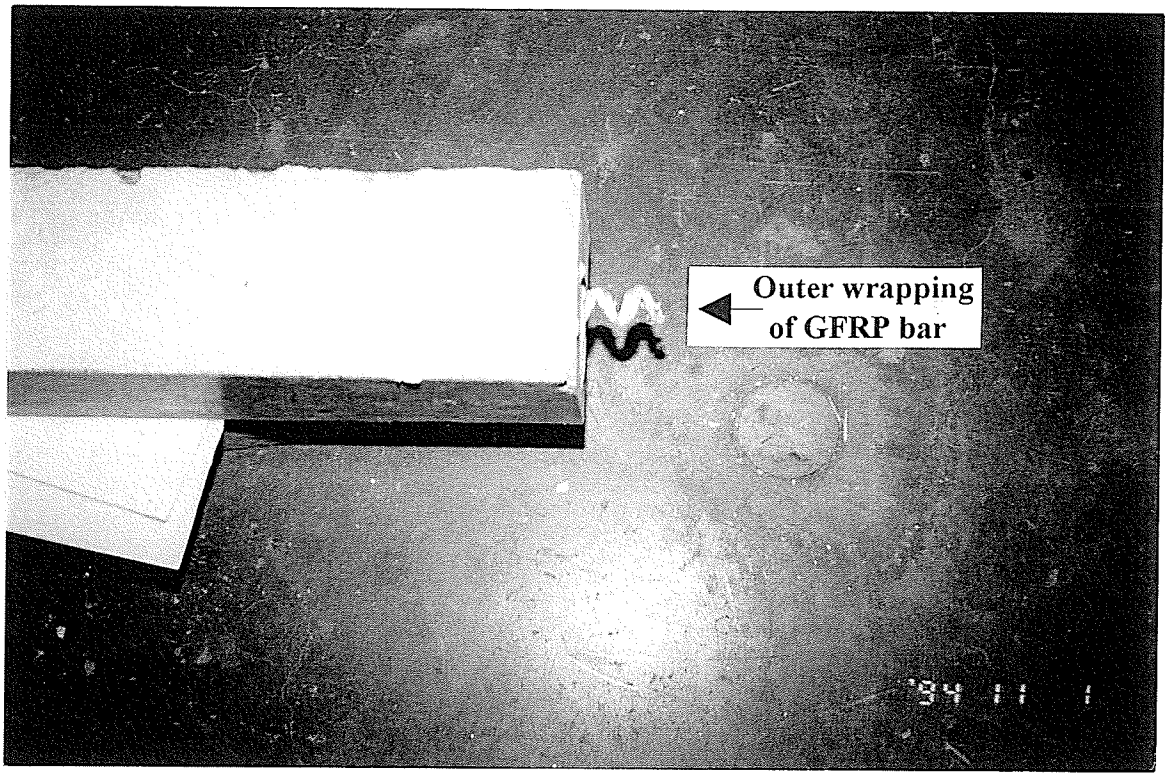

Figure 5.11(a): Debonding of the outer wrapping of the ISOROD bar.

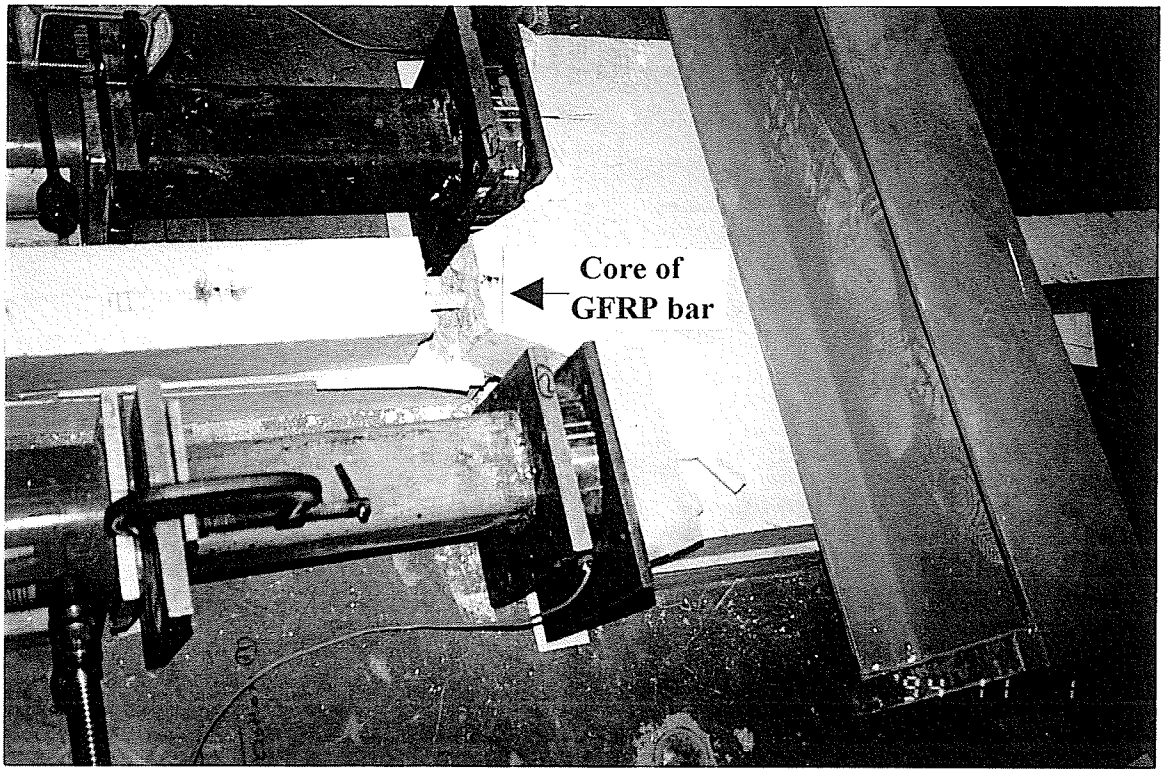

Figure 5.11(b): Concrete tension specimen.

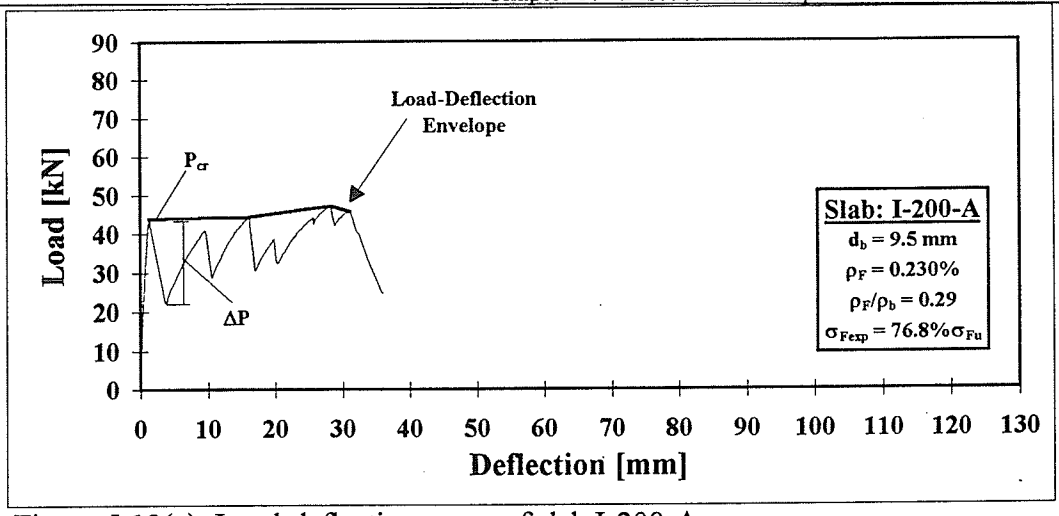

Figure 5.12(a): Load-deflection curve of slab I-200-A.

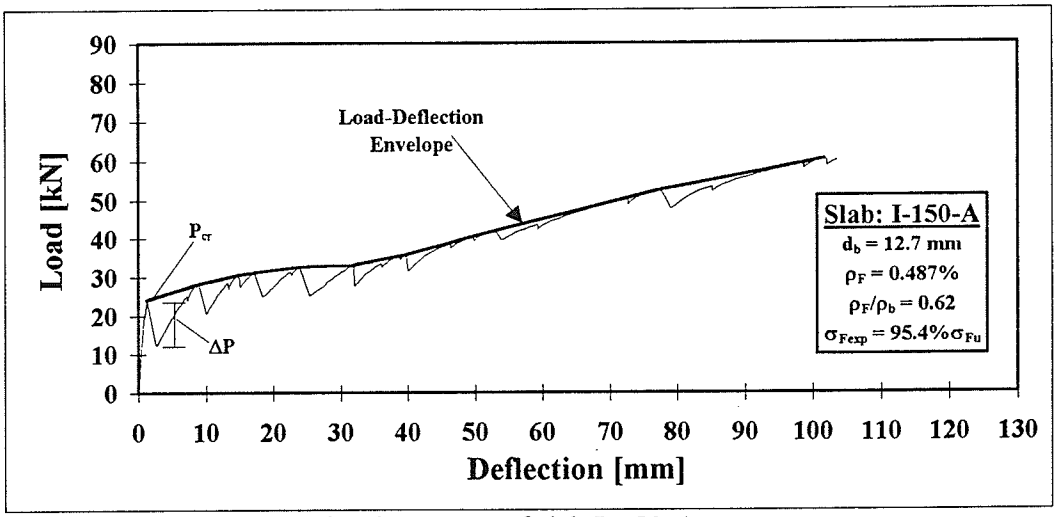

Figure 5.12(b): Load-deflection curve of slab I-150-A.

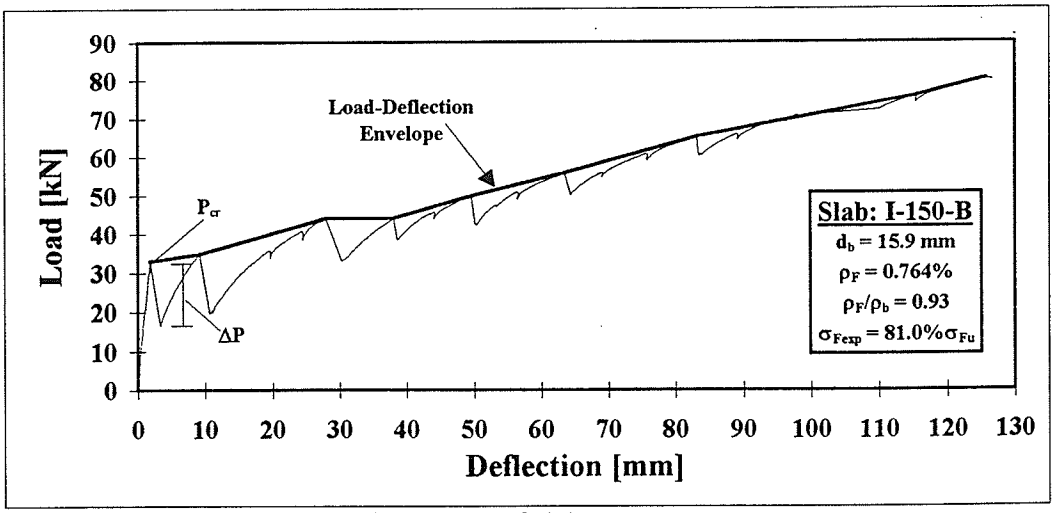

Figure 5.12(c): Load-deflection curve of slab I-150-B.

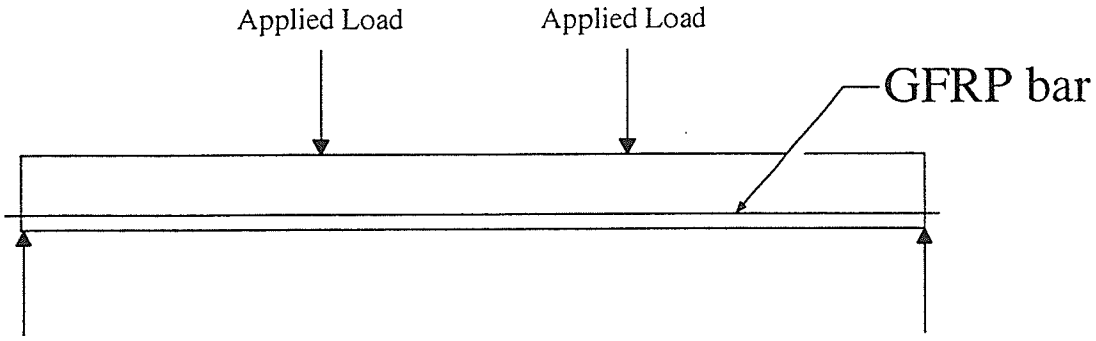

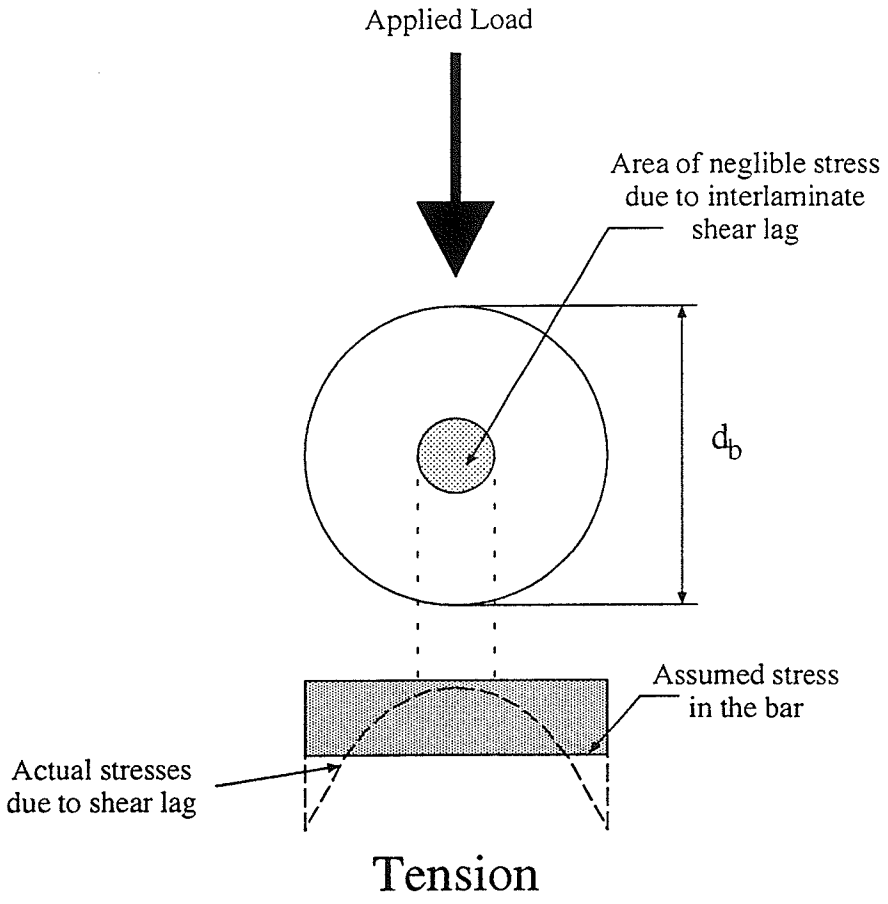

Figure 5.13: Stresses in GFRP bar induced by bending.

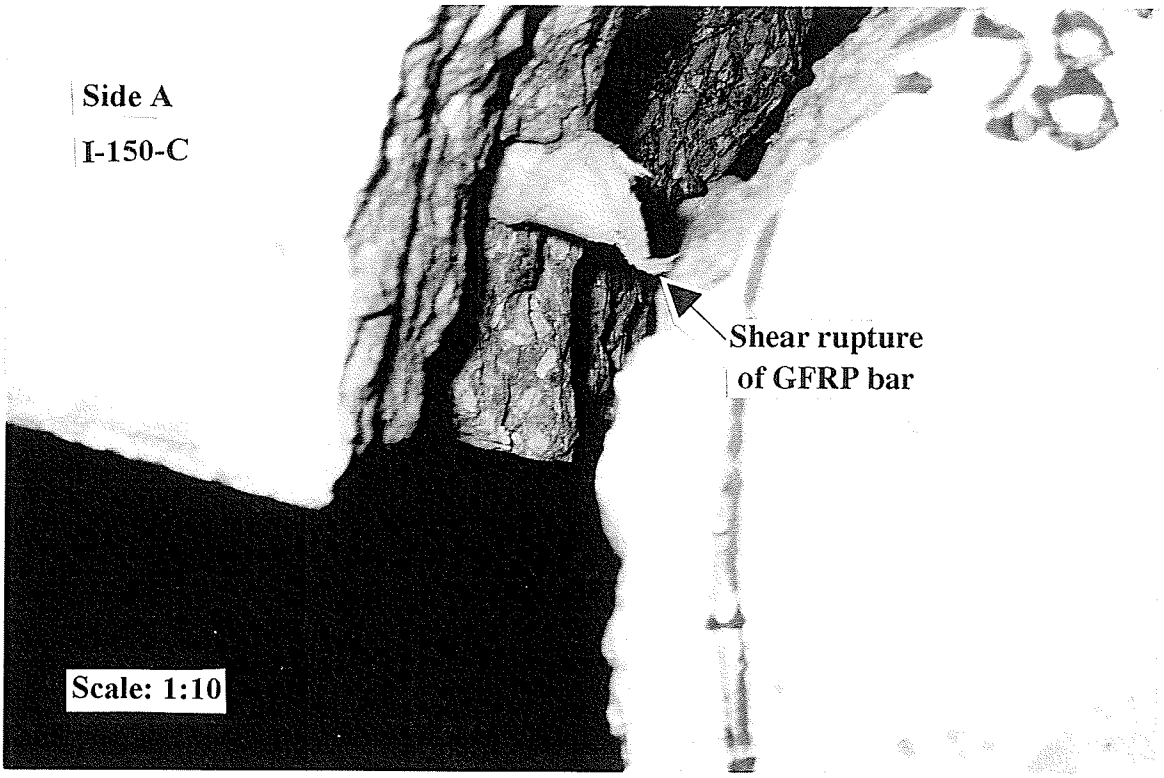

Figure 5.14: Shear rupture of ISOROD bar at the failure crack of slab I-200-C.

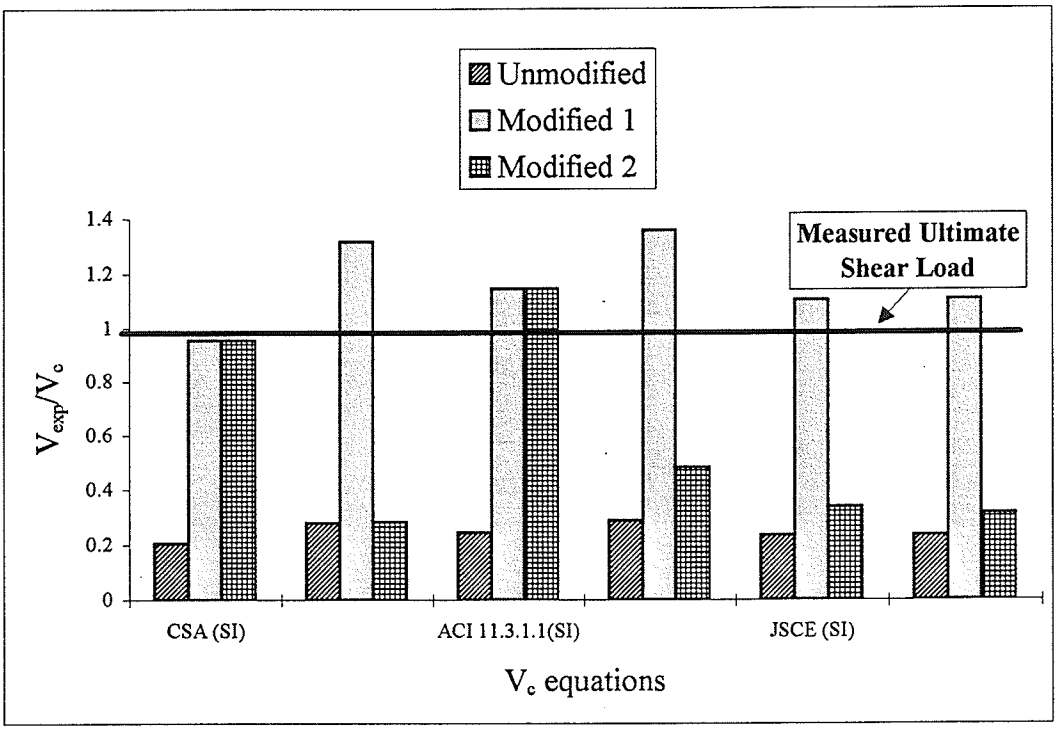

Figure 5.15: Comparison of modified and unmodified V_c equations for slab I-150-C.

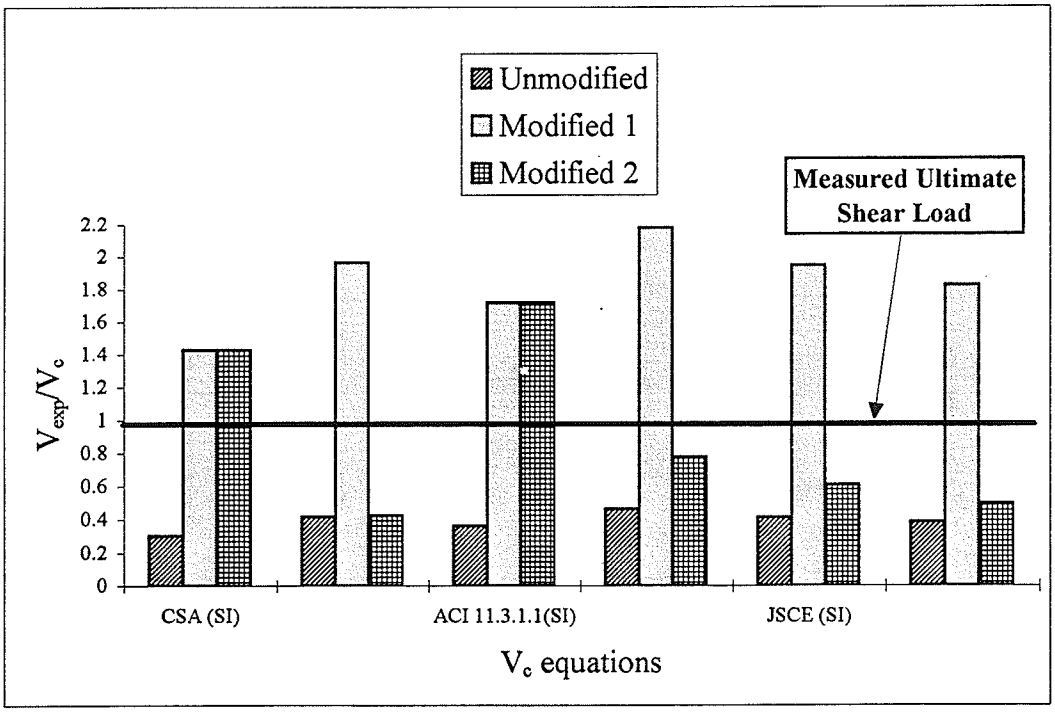

Figure 5.16: Comparison of modified and unmodified V_c equations for slab I-200-C.

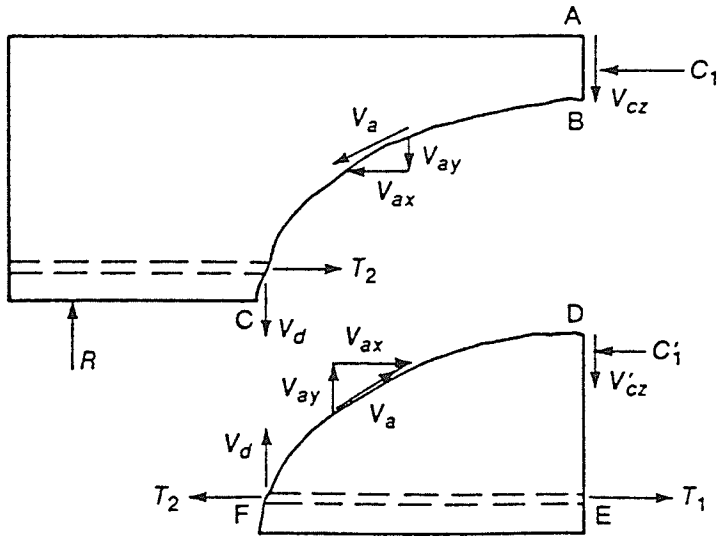

Figure 5.17: Shear strength components of V_c.

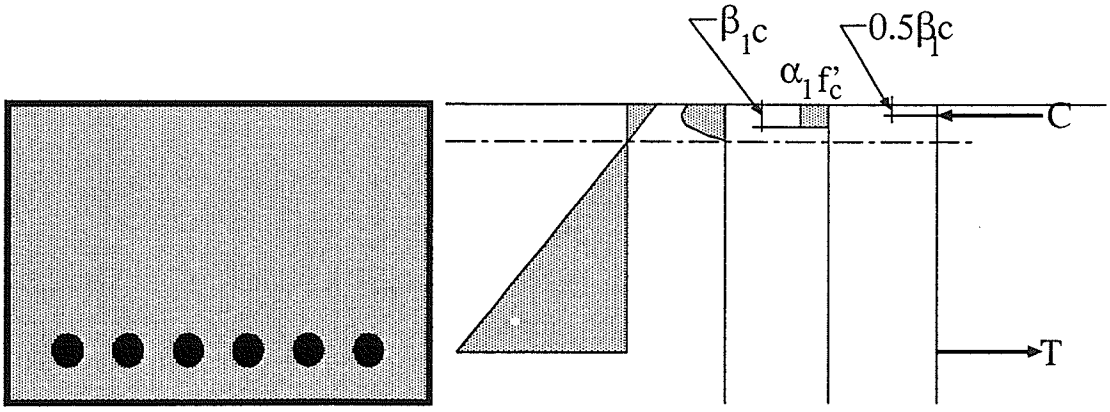

Figure 5.18: Strain compatibility of concrete members reinforced with GFRP bars.

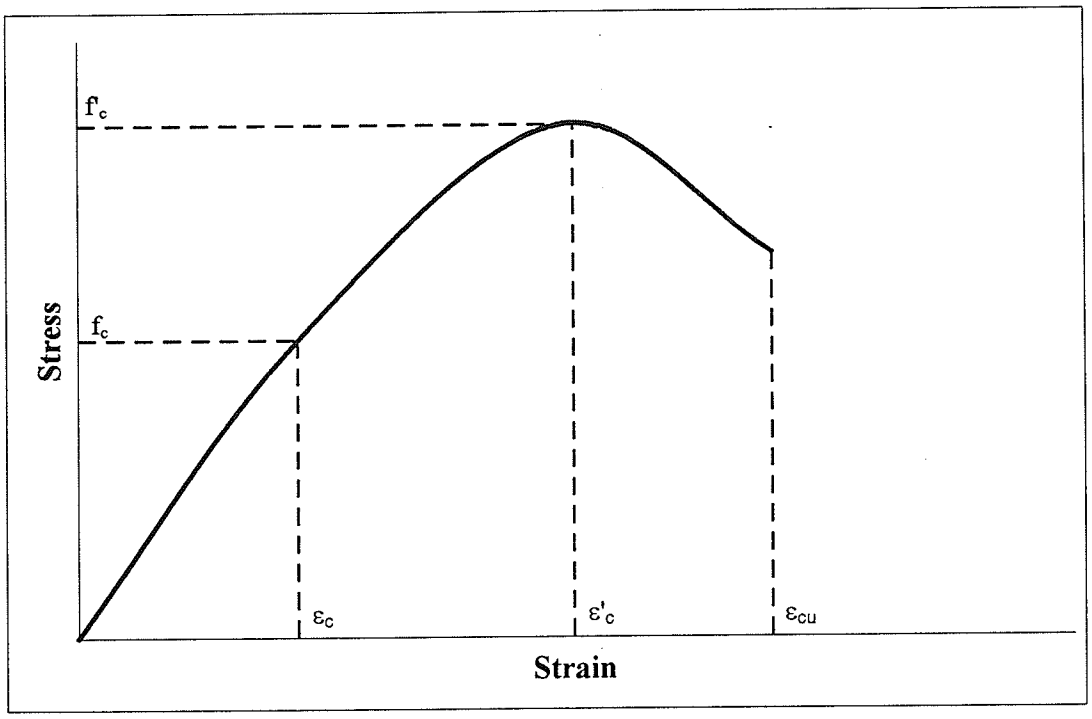

Figure 5.19: Stress-strain relationship of the concrete in compression.

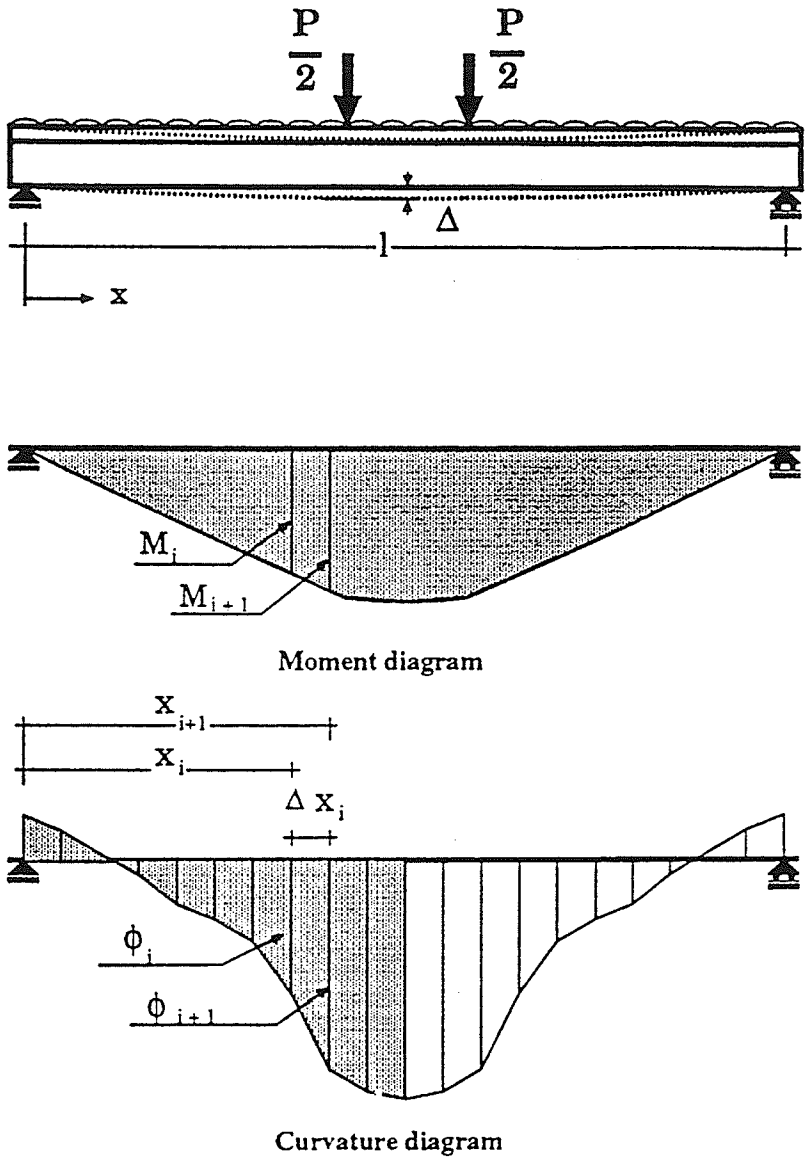

Figure 5.20: Numerical integration of the curvature for deflection calculation.

CHAPTER 6

SUMMARY AND CONCLUSIONS

6.0 SUMMARY

Eight one-way reinforced concrete slabs, with clear spans of 3000 mm, were tested under static loading conditions. Five slabs were reinforced by ISOROD-GFRP bars, two reinforced with conventional steel rebars and one slab reinforced with Leadline-CFRP rods. Behaviour of the specimens prior to and after cracking was monitored, including midspan deflections, crack widths and spacing. Test results provide a guide towards the development of design codes which will address the use of GFRP bars as reinforcement for structural concrete members.

6.1 CONCLUSIONS

Based on the experimental results and the observed behaviour, the following conclusions may be made:

1.) Behaviour of the FRP-reinforced specimens throughout the testing was bilinearly elastic until failure. Stiffness of the slabs reinforced by ISOROD-GFRP reinforcements is significantly reduced after initiation of cracks in comparison to the slabs reinforced by steel rebars.

2.) The slab behaviour exhibits adequate warning prior to failure through large and deep cracks, accompanied by large deformations for slabs reinforced by ISOROD-GFRP bars. Crack widths and deflections of slabs reinforced by ISOROD-GFRP reinforcements are significantly larger than comparable slabs with the same percentage of reinforcement using steel and Leadline-CFRP reinforcements. This is due to the low elastic modulus of GFRP bars in comparison to steel rebars, and the debonding of the outer deformation of this particular bar used in this study.

3.) For the under-reinforced slabs, designed to fail by rupture of the reinforcements, the GFRP bars did not reach the ultimate strain based on pure tension tests of the bars. This behaviour could be attributed to the localized failure of the fibres at the crack, due to the sudden transfer of tensile forces from the concrete to the GFRP bars at the crack. Increasing the diameter of the GFRP bars could also magnify the effect of the interlaminate shear lag phenomenon and consequently reduce the ultimate tensile stress of the GFRP bar. These two factors lead to the development of the general strength equation proposed to estimate the capacity of GFRP bars for flexural

behaviour. The behaviour suggests the use of a minimum reinforcement ratio for GFRP bars for concrete members subjected to flexural conditions.

4.) Heavily reinforced slabs with GFRP reinforcements could fail by shear of the GFRP reinforcements at a crack within the maximum shear-flexural zone. The measured dowel strengths of the GFRP bars is estimated to be 7.5% to 13.8% that of the ultimate tensile strength.

5.) The shear capacities provided by all of the current code equations significantly over-estimated the shear capacity of the slabs reinforced by GFRP bars. It is proposed to modify the current code equations for shear by the ratio of the elastic modulii of GFRP and steel, E_F/E_s.

6.2 RECOMMENDATIONS FOR FUTURE STUDY

In order to achieve a full understanding of the flexural behaviour of concrete slabs reinforced by GFRP bars, research should be continued in the future to include the following areas:

1.) Tensions tests on all the available diameters, as well as, small flexural tests should be completed in order to obtain the design factors needed in the proposed general strength equation.

2.) Further tests should be conducted which vary the percentage of reinforcement and result in an adequate amount of data to determine the minimum percentage of GFRP reinforcement.

3.) One-way concrete slabs reinforced by GFRP bars should be subjected to cyclic loading in order to obtain fatigue strength results.

4.) Due to the extensive use of one-way concrete slabs as bridge decks, punching shear testing should be pursued, in order to quantify the punching shear resistance of GFRP reinforced one-way concrete slabs.

5.) GFRP has a history of creeping, therefore, long term loading conditions of one-way concrete slabs reinforced by GFRP bars should be investigated. This should include tests on the effect of water intrusion and the alkali attack on the GFRP bars.

6.) Further testing on over-reinforced concrete slabs using GFRP reinforcements should be conducted, in order to modify further the current design codes for GFRP reinforced concrete members with respect to the concrete shear capacities.

7.) Since the dowel strengths of GFRP bars becomes the main component in resisting the shear loads, tests in concrete beams and slabs should be conducted.

REFERENCES

1. Abdelrahman, A., Tadros, G. and Rizkalla, S.H., "Test Model for the First Canadian Smart Highway Bridge," ACI Structural Journal, Vol. 92, No. 4, July-August, 1995.
2. Abdelrahman, A.A. and Rizkalla, S.H., "Serviceability of Concrete Beams Prestressed by CFRP Rods". *2nd Annual International Non-Metallic (FRP) Reinforcement for Concrete*, Ghent, Belgium: August 1995.
3. Abdelrahman, A.A., "Serviceability of Concrete Beams Prestressed by Fibre Reinforced Plastic Tendons," *Ph.D. Thesis*, Dept. of Civil and Geological Engineering, University of Manitoba, Winnipeg, Manitoba, Canada, Oct. 1995.
4. American Concrete Institute (ACI), "Building Code Requirements for Reinforced Concrete (ACI 318M-89) and Commentary-ACI 318RM-89," Detroit, Michigan, U.S.A., June 1990.

5. Bédard, C., "Composite Reinforcing Bars: Assessing Their Use in Construction," *Concrete International,* V. 14, No. 1, Jan. 1992, pp. 55-59.

6. Benmokrane, B., Masmoudi, R. and Chaallal, O., "Experimental and Analytical Study of the Flexural Behaviour of Concrete Beams Reinforced with GFRP Rebars," ACI Structural Journal, 28 pp. (under press).

7. Branson, D.E., "Deflections of Reinforced Concrete Flexural Members," Report by ACI Committee 415, Title 63-31, American Concrete Institute, Detroit, Mich., Dec., 1966.

8. Canadian Society for Civil Engineering, "Advanced Composite Materials with Applications to Bridges," *State of the Art Report*, May 1991.

9. Canadian Society for Civil Engineering, "Advanced Composite Materials in Bridges and Structures in Japan," *Technical Committee Mission to Japan*, August 1992, pp. 9-10.

10. Canadian Standards Association (CSA), "Design of Concrete Structures for Buildings (CAN3-A23.3-M94)," Rexdale, Ontario, Canada 1994.

11. Canadian Standards Association (CSA), "Design of Concrete Structures for Buildings (CAN3-A23.3-M84)," Rexdale, Ontario, Canada 1984.

12. Chaallal, O. and Benmokrane, B., "Physical and Mechanical Performance of an Innovative Glass-Fiber-Reinforced Plastic Rod for Concrete and Grouted Anchorages" *Canadian Journal of Civil Engineering*, Vol. 20, No. 2, 1993, pp. 254-268.

13. Clarke, J.L., "Alternative Materials for the Reinforcement and Prestressing of Concree," Blackie & Professional, an import of Chapman & Hall, 1993, pp. 204.

14. Clegg, A. and Markos, S., "Tension Stiffening of Concrete Reinforced by FRP," *Undergraduate Thesis*, Dept. of Civil and Geological Engineering, University of Manitoba, Winnipeg, Manitoba, Canada, April 1995.

15. Collins, M., and Mitchell, D., "Prestressed Concrete Structures", Prentice Hall, Englewood Cliffs, New Jersey, U.S.A., 766 pages.

16. Comité Euro-International du Béton and Fédération de la Précontrainte (CEB-FIP), "CEB-FIP Model Code for Concrete Structures," Third Edition, CEB, Paris, France, 1978, 348 pages.

17. Domenico, N., Mahmoud, Z. and Rizkalla, S.H., "Bond Properties of CFRP Prestressed Reinforcements," *Proceedings CSCE Annual Conference*, May 1996.

18. Faza, S.S. and GangaRao, H.V.S., "Pre- and Post-cracking Deflection Behaviour of Concrete Beams Reinforced with Fibre-Reinforced Plastic Rebars," Advanced Composite Materials in Bridges and Structures, CSCE, 1992, pp. 151-160.

19. Fickelhorn, M. , "Editorial," *Materials and Structures*, RILEM, V. 23, No. 137, Sept. 1990, pp. 317.

20. GangaRao, H.V.S. and Faza, S.S., "Bending and Bond Behaviour and Design of Concrete Beams Reinforced with FRP Rebars," FHWA-WV DOH Report'83, Dept. of Civil Engineering, University of West Virginia, Morgantown, W. Va., 1983.

21. Grieef, S., "ISOROD GFRP Dowel Bars in Concrete Pavements," *MS Thesis*, Dept. of Civil and Geological Engineering, University of Manitoba, Winnipeg, Manitoba, Canada, May 1996.

22. Head, P., "Use of Fibre Reinforced Plastics in Bridge Structures," *Congress Report*, 13th Congress of International Association for Bridge and Structural Engineering (IABSE), Helsinki, Finland, 1988, pp. 123-128.

23. Howell, Kerri M., "Corrosion of Reinforced Concrete Slab Foundations," *Materials Performance*, Dec. 1990, pp. 15-19.

24. Hull, Derek, "An Introduction to Composite Materials," *Cambridge Solid State Science Series*, Cambridge University Press 1981, pp. 1-57.

25. Jaeger, L.G., "Advanced Composite Materials in Bridges - Overview of Work to Date and Outline of Proposed Project," Vaughan Engineering Associates Ltd., Halifax, Nova Scotia, September 1989.

26. Japan Society of Civil Engineers (JSCE), "Concrete Library," International No. 4, Tokyo, Japan, December, 1984, 329 pages.

27. Johansen, E.J. and Roll, F., "A Prestressed Kevlar/FRP Structural System," ASCE 1st Materials Congress, Denver, Co., August, 1990.

28. MacGregor, J.G., "Reinforced Concrete: Mechanics and Design", Prentice Hall, New Jersey, U.S.A., pp. 180.

29. Machida, A., "Designing Concrete Structures With Continuous Fiber Reinforcing Materials," Dept. of Civil and Environmental Engineering, Saitama University, Urawa, Saitama 338, Japan, 1996, pp. 1-13.

30. Makhtouf, Hanna M., Ahmadi, Bijan H. and Al-Jabal, J., "Preventing Reinforced Concrete Deterioration in the Arabian Gulf," *Concrete International*, V. 13, No. 5, 1991, pp. 65-67.

31. Malvar, L.J., "Grip Effects in Tensile Testing of FRP Bars," Second FRP International Symposium, Non-Metallic (FRP) Reinforcements for Concrete Structures, Ghent, Belgium, August, 1995, pp. 108-115.

32. Malvar, L.J., "Tensile and Bond Properties of GFRP Reinforcement Bars," *ACI Materials Journal*, V. 92, No. 3, May-June, 1995.

33. Masmoudi, R., Benmokrane, B. and Chaallal, O., "Cracking Behaviour of Concree Beams Reinforced with FRP Rebars," Proceedings of the First International Conference on Composites in Infrastructure (ICCI '96), Tucson, Arizona, U.S.A., Jan. 15-17, 1996, pp. 374-388.

34. Meier, U. and Kaiser, H., "Strengthening of Structures with CFRP Laminates," *Advanced Composite Materials in Civil Engineering Structures*, Proceedings of the Specialty Conference, Las Vegas, Nevada, Jan. 31-Feb. 1, 1991, ASCE, pp. 288-301.

35. Meier, U., "Designing and Producing Materials by Combination," *Materials and Structures*, Vol. 21, 1988, pp. 85-89.

36. Meier, U., "Proposal for a Carbon Fibre Reinforced Composite Bridge Across the Strait of Gibraltar at its Narrowest Site," *Proceedings of International Mechanical Engineers*, Vol. 201, No. B2, 1987, pp. 73-78.

37. Michaluk, C.R., "Technical Report on Experimental Results: Behaviour of Concrete Slabs Reinforced by ISOROD Glass-Fibre Reinforcements," *Technical Report for M.Sc. Thesis*, Dept. of Civil and Geological Engineering, University of Manitoba, Winnipeg, Manitoba, Canada, August 1995.

38. Mitsubishi Kasei Corporation, "Leadline Carbon Fibre Tendons/Bars", *Product Manual*, December, 1992, 75 pages.

39. Murphy, J., "Reinforced Plastics Handbook," *Elsvier Advanced Technology*, Elsvier Science Publishers Ltd. 1994, pp. 56-72.

40. Mutsuyoshi, H., Uehara, K. and Machida, A., "Mechanical Properies and Design Method of Concrete Beams Reinforced with Carbon Fiber Reinforced Plastics," Transactions of the Japan Concrete Institute, Vol. 12, 1990, Tokyo, Japan, pp. 231-238.

41. Nanni, A., "Flexural Behaviour and Design of RC Members Using FRP Reinforcement," ASCE Journal of Structural Engineering, Vol. 119, No. 11, Nov., 1993, pp. 3344-3359.

42. Nawy, E.G. and Neuwerth, G.E., "Fiberglass Reinforced Concrete Slabs and Beams," ASCE Journal of the Structural Division, No. ST2, Vol. 103, Proc. Paper 12762, Feb. 1977, pp. 420-421.

43. Nawy, E.G., Neuwerth, G.E. and Phillips, C.J., "Behavior of Fiber Reinforced Concrete Beams," ASCE Journal of the Strucural Engineer, No. ST9, Vol. 97, Proc. Paper 8353, Sept. 1971, pp. 2203-2215.

44. Noritake, K., Kumagai, S.I. and Mizutani, J., "Practical Use of Aramid FRP Rods for PC Structures," The Third East Asia-Pacific Conference on Structural Engineering and Construction, Shanghai, China, April 23-26, 1991.

45. Park, R. and Paulay, T., "Reinforced Concrete Structures", John Wiley & Sons, 769 pages.

46. SPI Composites Institute, "FRP Composites in Construction Applications: A Profile in Progress," New York, New York, U.S.A., 1995, pp. 91.

47. Yeomans, S.R., "Performance of Black, Galvanized, and Epoxy-Coated Reinforcing Steels in Chloride-Contaminated Concrete," *Corrosion*, V. 50, No. 1, Jan. 1994, pp. 72-81.